Field relations, petrography and 40Ar/39Ar cooling ages of hornblende in a part of the eclogite-bearing domain, Sveconorwegian Orogen

Nasim Mozafari Amiri

**Dissertations in Geology at Lund University,
Master's thesis, no 329
(45 hp/ECTS credits)**

**Department of Geology
Lund University
2013**

Field relations, petrography and $^{40}Ar/^{39}Ar$ cooling ages of hornblende in a part of the eclogite-bearing domain, Sveconorwegian Orogen

Master's thesis
Nasim Mozafari Amiri

Faculty of Science
Department of Geology
Lund University
2013

Contents

Cover Picture: Chevron fold in the migmatitic grey orthogneiss

Field relations, petrography and ^{40}Ar/^{39}Ar cooling ages of hornblende in a part of the eclogite-bearing domain, Sveconorwegian Orogen

NASIM MOZAFARI AMIRI

Abstract: High-pressure metamorphism and deformation of the Ullared Deformation Zone (UDZ) in the Eastern segment of the Sveconorwegian Orogen, southwest Sweden is evidenced by ~ 970 Ma retro-eclogite found in association with upper amphibolite and high-pressure granulite facies rocks. Petrographic, structural and geochronological studies of the UDZ were carried out to better understand the regional metamorphism and deformation history with focus on a ~N-S trending part of the zone influenced by a late stage of deformation during Sveconorwegian orogeny, namely the Svarten Zone.

The deformational history of the investigated area can be discussed in two scenarios. In the first one, an E-W extension component synchronized with the onset of migmatization was responsible for the development of an old upright and symmetric ESE-WNW generation of folds. The folds were later influenced by an intense phase of shear, which formed the isoclinal folds and the parallel mineral stretching lineation. The old ESE-WNW foliation was deflected by a later phase of NNW-SSE shear, following the isoclinal folds development. The second possible scenario is that a NNW-SSE shear phase has taken place synchronized with E-W extension, following the regional migmatization, resulted in E-plunging mineral stretching lineation and isoclinal folds development, which consequently deflected ESE-WNW foliations. Regardless of which scenario is correct, the sheared limb of a young, open and upright generation of folds indicate that a late phase of shear has taken place in association with ~N-S structure of the Svarten Zone.

Mineral assemblages indicate the occurrence of retrograde metamorphism resulted from uplift of the Sveconorwegian Orogen, reflected in the amphibolite mineral assemblages overprinting of the eclogite and the granulite facies. ^{40}Ar/^{39}Ar dating of hornblende yielded cooling ages that range from 920 Ma to 927 Ma. The cooling rates of 5.5-6.4 °C/m.y. and 4.5-5.2 °C/m.y. were obtained from the onset of partial melting and migmatization down to the hornblende cooling age of 920 Ma to 927 Ma, respectively, upon the chosen closure temperatures of 500°C and 550°C. The cooling rates are associated with uplift of the Sveconorwegian Orogen and cooling after peak metamorphism.

Nasim Mozafari Amiri, Department of Geology, Lund University, Sölvegatan 12, SE-223 62 Lund, Sweden.
E-mail: nasim.mozaffari@gmail.com

1   Introduction

The Sveconorwegian Orogen in southwest Scandinavia (Fig. 1) formed during late Mesoproterozoic to early Neoproterozoic as a result of accretion ending with continent-continent collision (Bingen et al. 2008). The southern Eastern Segment (Fig. 1) is dominated by upper amphibolite and high-pressure granulite facies rocks, which hosts remnants of ~ 980 Ma eclogite, which are evidence of burial to depths in excess of 50 km (Möller 1998, 1999; Johansson et al. 2001; Möller et al. 2012). The Ullared Deformation Zone (UDZ, Möller et al. 1997) is a high-temperature deformation zone situated in the Eastern Segment of the Sveconorwegian Orogen, which formed during the late stage of the orogeny.

Knowledge on the processes in which eclogite-bearing crust was formed and exhumed is critical for tectonic interpretation. This study focuses on a part of the UDZ with the aims to characterize and interpret the late stage ductile deformation. The investigation area is located in the NE part of the UDZ, where the strike is predominantly NNW-SSE, informally termed the Svarten Zone (SZ, Fig. 2). Since two sets of planar gneissic fabrics were observed in the Svarten Zone, ~E-W trending and ~N-S trending respectively, there is a probability that two different deformation phases can be distinguished (Fig. 2).

The specific objectives of this study were:
- Bedrock mapping in the scale of 1:10000 between Lake Byasjön and Dughult (~ 7 × 2.5 km).
- Characterization and interpretation of deformation structures, including different planar and linear fabrics and small-scale structures.
- Characterization of mineral assemblages and metamorphic textures associated with different deformation structures in order to assess the metamorphic conditions during deformation.
- $^{40}Ar/^{39}Ar$ geochronology of hornblende, in order to date cooling through c. 500°C- 550°C.

2   Geological setting

2.1   The Sveconorwegian Orogen

The Sveconorwegian Orogen in southern Scandinavia is considered as the tectonic counterpart of the Grenville Orogen in the eastern Canada. The Orogen formed in the time period 1.14-0.90 Ga, as a consequence of continent collision between Fennoscandia and another continent (possibly Amazonia; Hoffman 1991). The Sveconorwegian Orogen comprises five different lithotectonic segments (Bingen et al. 2005), which are separated by approximately N-S trending deformational zones in crustal-scale (Park et al. 1991). These segments are, from east to west, the Eastern Segment, the Idefjorden Terrane, the Bamble Terrane, the Kongsberg Terrane and the Telemarkia Terrane (Fig. 1). Each of these has its own characteristics regarding crustal evolution, deformation and metamorphism. The easternmost boundary of the Sveconorwegian Orogen is a low grade east-vergent thrust zone, the Sveconorwegian Frontal Deformation Zone (SFDZ, Fig. 1; Wahlgren et al. 1994).
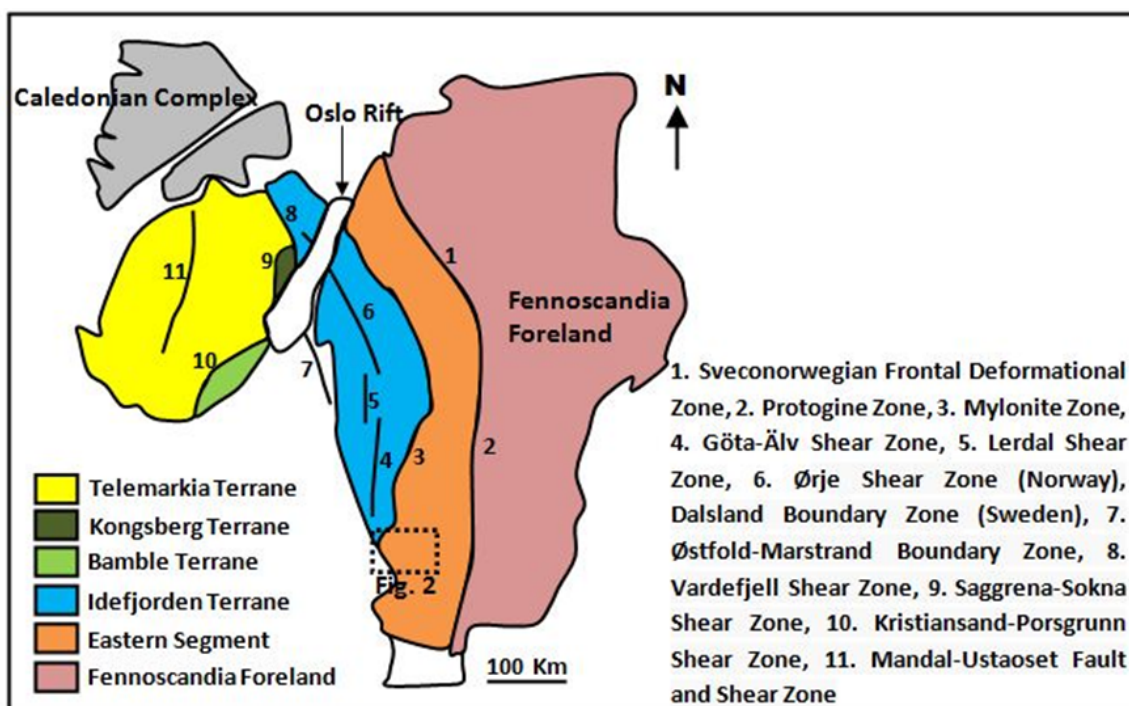

Fig. 1. Map of southwest Scandinavia showing lithological units of the Sveconorwegian Orogen and the associated shear zones (Modified after Bingen et al. 2008).
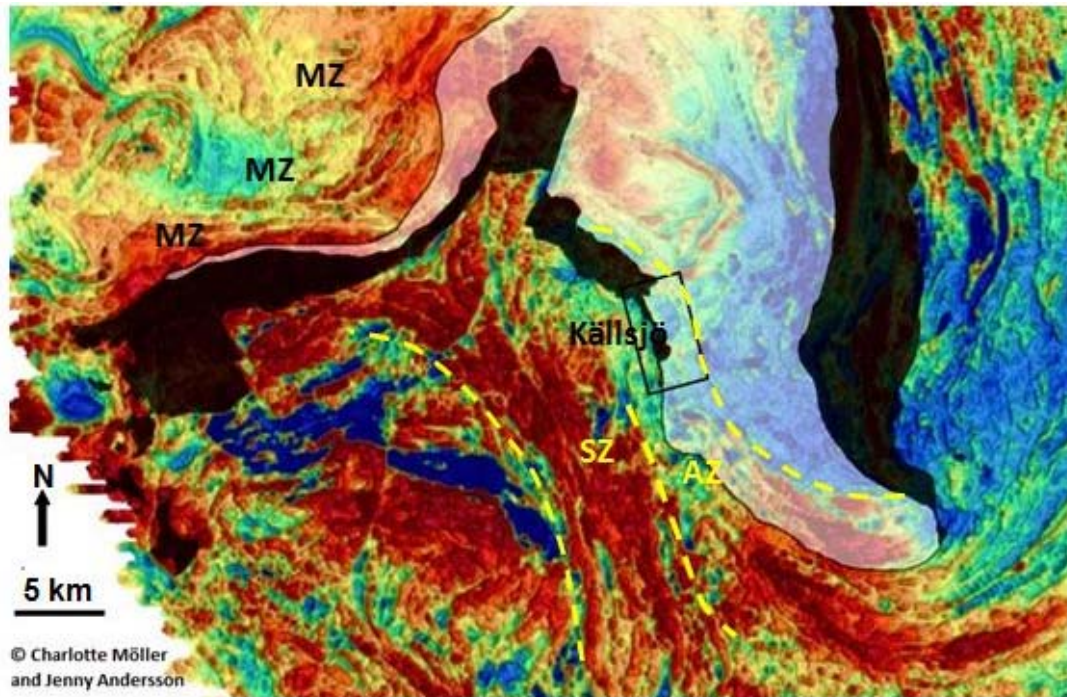
Fig. 2. Airborne magnetic map of the Varberg-Ullared area (source SGU), with occurrences of 1.4 Ga porphyritic granite and augenic gneiss outlined in black (source SGU and Möller et al. unpublished) and the eclogite-bearing gneiss domain shaded in white (Möller et al. 2011). Dashed lines show approximate shear zone boundaries of the Ammås Zone (AZ) and the Svarten Zone (SZ; Möller et al. 2011). These two zones were originally interpreted as one zone or system and coined the Ullared Deformation Zone (UDZ; Möller et al. 2007).

Metamorphism, partial melting and deformation of the Fennoscandian crust involving both compressional and extensional kinematics characterizes the Sveconorwegian rocks (Bingen et al. 2008). Prior to the onset of the Sveconorwegian orogeny, between 1.28 and 1.14 Ga, western Fennoscandia was affected by bimodal magmatism, mostly occurring in the Telemarkia terranes (Laajoki et al. 2002), but also traceable deep into the Fennoscandia Craton (Söderlund and Ask 2006). Early high-grade metamorphism took place at 1.14-1.13 Ga (Arendal phase) in the Bamble Terrane (Smalley et al. 1983, Bingen et al. 2012). Agder phase (1.05 - 0.98 Ga), the main phase of regional deformation, metamorphism and partial melting affected the western parts of the orogen and eastwards into the Idefjorden Terrane. It involved metamorphism with varying degrees in various regions of the orogen, from lower amphibolite to high-pressure granulite facies (e.g. Bingen et al. 2008, Söderlund et al. 2008). The Falkenberg phase (0.98-0.96) Ga reflects the final convergence associated with the continent-continent collision, and caused eclogite and high-pressure granulite metamorphism in the Eastern Segment (Möller 1998, 1999; Johansson et al. 2001). During the Dalane phase (0.97-0.90 Ga) the Orogen underwent gravitational collapse (Bingen et al. 2006) along with exhumation and uncovering of the buried rocks. Extensional reactivation of the major shear zones and, in the central parts of the orogen, granite magmatism have taken place. The last relative motion between the Sveconorwegian terranes took place around 0.92-0.91 Ga.

2.2 The southern Eastern Segment

The Eastern Segment is composed of 1.81-1.66 Ga old metagranitoids and orthogneisses (Connelly et al. 1996; Söderlund et al. 1999; Söderlund et al. 2002; Möller et al. 2007; Bingen et al. 2008). It is considered as parautochthonous and is bounded by major deformation zones both to the east and west (Bingen et al. 2005) (Fig. 1). The Mylonite Zone constitutes a west-dipping boundary to the overlying and allochthonous Idefjorden Terrane (Park et al. 1991; Stephens et al. 1996).

High-grade metamorphism in the southern Eastern Segment is commonly reflected in migmatitic orthogneisses, migmatitic garnet amphibolite and mafic high-pressure granulite lenses. P-T estimates for the Sveconorwegian metamorphism are 680-770 °C and 9-12 kbar (Johansson et al. 1991; Wang and Lindh 1996; Möller 1998, 1999). Pressures correspond to depths of c. 30-45 km: however, the occurrence of eclogite remnants in a part of the Eastern Segment (Möller 1998, 1999; Austin Hegardt et al. 2005) is evidence of greater than 50 km burial depths.

Pre-Sveconorwegian metamorphism (Halladian orogeny) involved regional scale migmatization at 1.46 -1.42 Ga (Christoffel et al. 1999; Söderlund et al. 2002; Möller et al. 2007). At 1.40-1.38 Ga, following

the Hallandian orogeny, charnockitic granite and syenitoids intruded in the Eastern Segment (Andersson et al. 1999 and references therein).

2.3 The Ullared Deformation Zone

The Ullared Deformation Zone is characterized by the occurrences of decompressed retroeclogite in the Eastern Segment. An age of 972 ± 14 Ma was obtained for prograde eclogite metamorphism on metamorphic zircon inclusions in garnets (Johansson et al. 2001). Möller et al. (2011, 2012) interpreted the eclogite-bearing unit as a recumbent isoclinal fold nappe, about 60 × 30 km, with high-strain mylonitic gneiss located along its southern margin. Based on the aeromagnetic data, UDZ was interpreted as a shear zone or probably a shear zone system (Möller et al. 1997) with variable strikes in different areas. Lundberg and Juhlin (2011) presented seismic data across the UDZ which reveals that structures dip shallowly to moderately towards the north. Their data are in concordance with the structural and metamorphic data (Möller et al. 2011, 2012) and the airborne magnetic pattern (SGU) which suggests that the bedrock across the UDZ is composed of distinct tectonometamorphic units.

3 Methods

3.1 Field work

Field work was performed during six weeks in August to October 2011 using magnetic anomaly maps in the scale of 1:50000 and topographic maps in the scale of 1:10000 as base maps. The investigated area cover 17.5 km^2 and include 255 outcrop observations. Map preparation was made using ArcGIS 9 (ArcMap 9.3.1) software. Measurements of foliations, stretching lineations and fold axes were plotted in Tectonic FP 1.75 software. Small-scale asymmetric structures were documented and used for shear sense interpretation.

3.2 Petrography

Thin sections of fifteen selected samples were investigated using a standard petrographic microscope to investigate the mineral assemblage, metamorphic texture and metamorphic facies.

3.3 Geochronology

Nine hornblende-bearing hand samples were crushed with a jaw-crusher. The crushed material was sifted, using plastic sieves, into two separate grain size fractions, 0.25-0.5 mm and 0.5-1 mm. Hornblende grains were hand-picked under optical microscope.

$^{40}Ar/^{39}Ar$ geochronology was carried out at the geochronology laboratory of Lund University, Sweden. The samples selected for geochronology study were irradiated together with the TCR sanidine standard (28.34 Ma following Renne et al. 1998), for 14 hours at the Oregon State research reactor. J-Values were calculated with a precision of <0.25% and reported for each sample in the data tables. Decay constants utilized were those given in Steiger and Jäger (1977).

The $^{40}Ar/^{39}Ar$ geochronology laboratory at Lund University contains a Micromass 5400 mass spectrometer with a Faraday and an electron multiplier. A metal extraction line, which contains two SAES C50-ST101 Zr-Al getters and a cold finger cooled to ca. 155°C by a Polycold P100 cryogenic refrigeration unit, is also present. Hornblende fractions were loaded into a copper planchette that consists of several 3 mm holes. Samples were step-heated using a defocused 50W CO_2 laser. Sample clean-up time was five minutes that made use of the two hot Zr-Al SAES getters and a cold finger with a Polycold refrigeration unit. The laser was rastered over the samples to provide even-heating of all grains. The entire analytical process is automated and runs on a Macintosh-steered OS 10.7 with software modified specifically for the laboratory at Lund University and developed originally at the Berkeley Geochronology Center by Al Deino.

Time zero regressions were fitted to data collected from 10 scans over the mass range of 40 to 36. Peak heights and backgrounds were corrected for mass discrimination, isotopic decay and interfering nucleogenic Ca-, K-, and Cl-derived isotopes. Isotopic production values for the cadmium lined position in the OSU reactor are $^{36}Ar/^{37}Ar$ (Ca) = 0.000264, $^{39}Ar/^{37}Ar$ (Ca) = 0.000695, and $^{40}Ar/^{39}Ar$ (K) = 0.00073. ^{40}Ar blanks were calculated before every new sample and after every three sample steps. Blank values were subtracted for all incremental steps from the sample signal. The laboratory was able to produce very good incremental gas splits, using a combination of increasing time at the same laser output, followed by increasing laser output. Age plateaus were determined using the criteria of Dalrymple and Lamphere (1971), which specify the presence of at least three continuous incremental heating steps with statistically indistinguishable ages and constituting greater than 40% of the total ^{39}Ar released during the experiment. In some places, where a statistical overlap of steps is not obtained, a forced-fit age is given over a pre-determined percentage of gas.

$^{40}Ar/^{39}Ar$ geochronology data were produced, plotted and fitted using the argon programme provided by Al Deino from the Berkeley Geochronology Centre, USA. Data was subsequently exported to MS Excel tables.
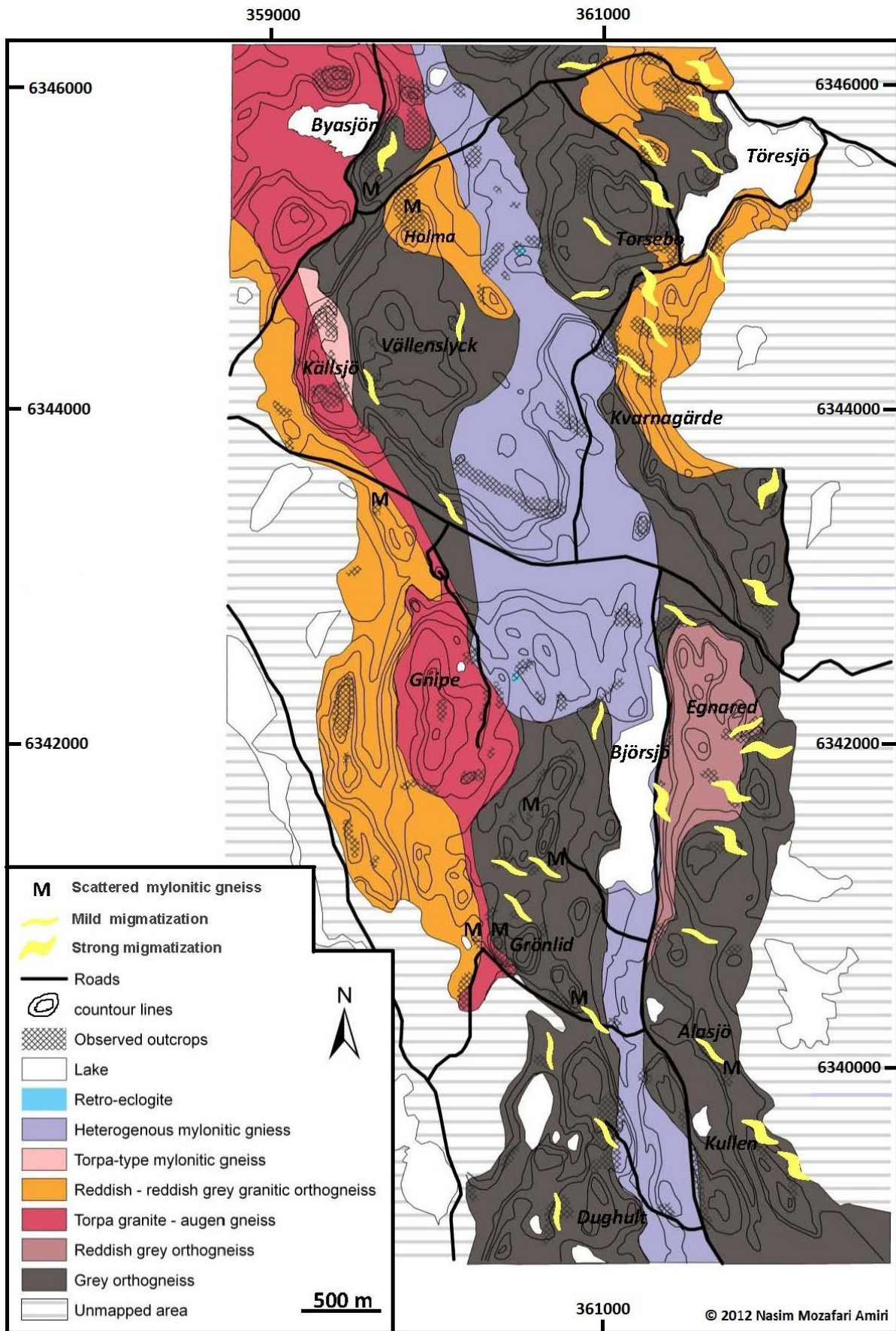
Fig. 3. Lithological map of the study area.

4   Lithology and petrography

The mapped area consists of heterogeneous and layered gneissic rocks with variable amounts of strain and migmatization. Eight different rock units were distinguished (Fig. 3):
- Grey orthogneiss
- Reddish grey orthogneiss
- Torpa-type granite-augen gneiss
- Granitic orthogneiss
- Retro-eclogite
- Heterogenous mylonitic gneiss
- Torpa-type mylonitic gneiss
- Garnet-rich amphibolite

The locations of observation points discussed in the text are marked on the map in Fig. 24 (chapter 5) and coordinates are listed in Table 1. Contacts between the rock units were determined with fairly high accuracy, since the observed localities were so close to each other. There are minor occurrences, which due to their small size, were ignored when drawing the map. For instance locality 68, which exposes c. 10 × 10 m grey orthogneiss, occurs within an area dominated by granitic gneiss.

4.1   Grey orthogneiss

The grey orthogneiss (similar rocks dated at c. 1.7 Ga, SGU database) is widespread in the investigated area (Fig. 3). It is characterized by strong migmatization (4a & b), which regarding to domination of the felsic and mafic minerals, can be classified into intermediate and dark varieties, respectively. Due to the close spatial associations between these two types in the field, and difficulties to determine actual contacts, they are shown as the same rock type on the map. In general, quartz, plagioclase and some K-feldspar constitute the leucosome while the mesosome is made

Table.1. Key locality coordinates in SWEREF 99. The blue rows mark coordinates lower precision due to a GPS problem.

Locality No.	N	E	Rock type	Locality No.	N	E	Rock type
NMA11001	6346061	359313	Augen gneiss	NMA11049b	6342440	360450	Mylonitic gneiss and retroeclogite
NMA11002	6345988	359796	Granitic gneiss	NMA11049c	6342400	360350	Mylonitic gneiss
NMA11004	6346123	360762	Migmatitic grey gneiss	NMA11052a	6345290	362090	Mylonitic gneiss
NMA11010	6345392	361325	Migmatitic grey gneiss	NMA11054c	6344577	359267	Torpa-type mylonitic gneiss
NMA11016a	6345714	361603	Migmatitic reddish grey gneiss	NMA11055	6344542	359339	Garnet-rich amphibolite
NMA11016b	6345755	361698	Migmatitic reddish grey gneiss	NMA11065d	6344180	359570	Migmatitic grey gneiss
NMA11018	6344847	360307	Mylonitic gneiss	NMA11068a	6341775	359848	Migmatitic grey gneiss
NMA11019	6344907	360261	Mylonitic gneiss	NMA11068b	6341793	359865	Migmatitic grey gneiss
NMA11021b	6345144	361333	Migmatitic grey gneiss	NMA11074	6341839	360242	Torpa granite
NMA11024	6344875	361197	Reddish grey gneiss	NMA11083	6340851	360265	Mylonitic gneiss
NMA11029	6345056	360472	Retroeclogite	NMA11087	6340812	360357	Mylonitic gneiss
NMA11030	6345052	360625	Granitic gneiss	NMA11090	6340533	360700	Migmatitic grey gneiss
NMA11031c	6344078	360737	Mylonitic gneiss	NMA11091	6340435	360806	Migmatitic grey gneiss
NMA11034	6344507	361036	Migmatitic grey gneiss	NMA11092	6340348	361058	Mylonitic gneiss
NMA11035	6345052	360625	Migmatitic grey gneiss	NMA11095	6341267	360613	Reddish grey gneiss
NMA11039	6343374	360820	Mylonitic gneiss	NMA11100	6340013	361270	Mylonitic gneiss
NMA11040b	6343337	361168	Mylonitic gneiss	NMA11105	6342043	361972	Migmatitic grey gneiss
NMA11041a	6342870	361910	Migmatitic grey gneiss	NMA11110	6341378	361857	Migmatitic grey gneiss
NMA11041b	6342810	361980	Migmatitic grey gneiss	NMA11125	6341571	361349	Reddish grey gneiss
NMA11044b	6344100	359310	Augen gneiss	NMA11137	6344751	360861	Reddish grey gneiss
NMA11045b	6344140	359280	Torpa-type granitic gneiss	NMA11150	6339112	361643	Mylonitic gneiss
NMA11049a	6342460	360560	Mylonitic gneiss				
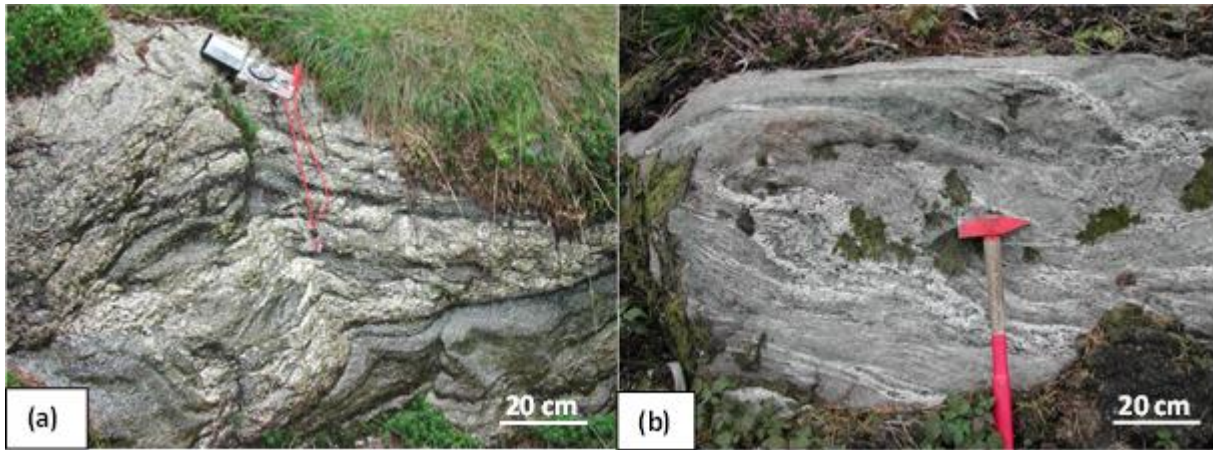
Fig. 4. (a) Migmatitic grey orthogneiss with white leucosome, locality 105. (b) Migmatitic grey orthogneiss with white leucosome, locality 65d. Location numbers for these and following illustrations are marked on the map in Fig. 24.

up of hornblende, biotite with lesser amounts of plagioclase, quartz and occasionally opaque minerals (e.g. Pyrite, localities 4 and 21b). Leucosome is commonly medium or coarse grained whereas mesosome is fine grained or relict medium grained. Amphibolite lenses of different size from centimeters to meters is another common characteristic of the migmatitic orthogneiss (Fig. 31b). In some localities, grey orthogneiss has sugary texture (Locality 68b, below).

4.1.1 Sample NMA11021b Migmatitic grey orthogneiss

This sample represents a weakly foliated medium to fine-grained migmatitic intermediate grey orthogneiss (tonalitic composition) made up of plagioclase, hornblende, quartz and biotite, with accessory allanite, epidote, opaques and zircon (Fig. 5a & b). The rock is characterized by inequigranular texture with subhedral
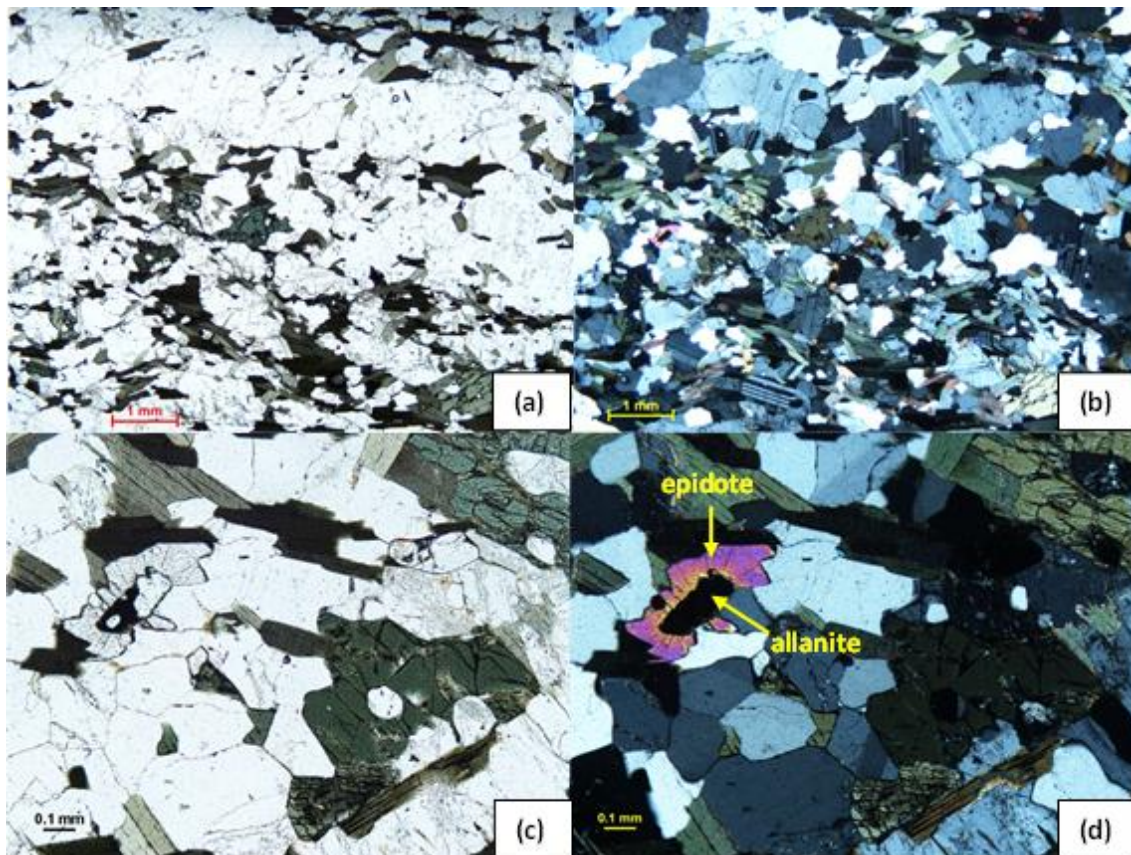
Fig. 5. (a)-(d) Photomicrographs of tonalitic gneiss, sample NMA11021b. (a) PPL, Plagioclase, quartz, biotite and hornblende with accessory allanite, epidote, opaques and zircon. (b) CPL, same view as in a. (c) PPL, Allanite crystal and radial fractures in surrounding epidote grain. (d) CPL, same view as in c.

10

grain boundaries. Hornblende and biotite are more strained than the other minerals. Saussurite occurs locally in plagioclase (Fig. 5a-d).

4.2 Reddish grey orthogneiss (Grey orthogneiss with reddish leucosome)

The grey orthogneiss with reddish leucosome (Fig. 3) is located on the right side of lake Björsjö, in association with the grey orthogneiss, but can be occasionally found in the other localities. Reddish leucosome oc-

curs parallel to the gneissic foliation (Fig. 6a & b). The leucosomes are generally made up of medium- to coarse-grained K-feldspar and elongated quartz occasionally with plagioclase.

4.2.1 Sample NMA11016a Reddish grey orthogneiss

This sample is a weakly strained, fine- to coarse-grained migmatitic reddish grey orthogneiss composed of plagioclase (locally antiperthite), quartz, K-feldspar,
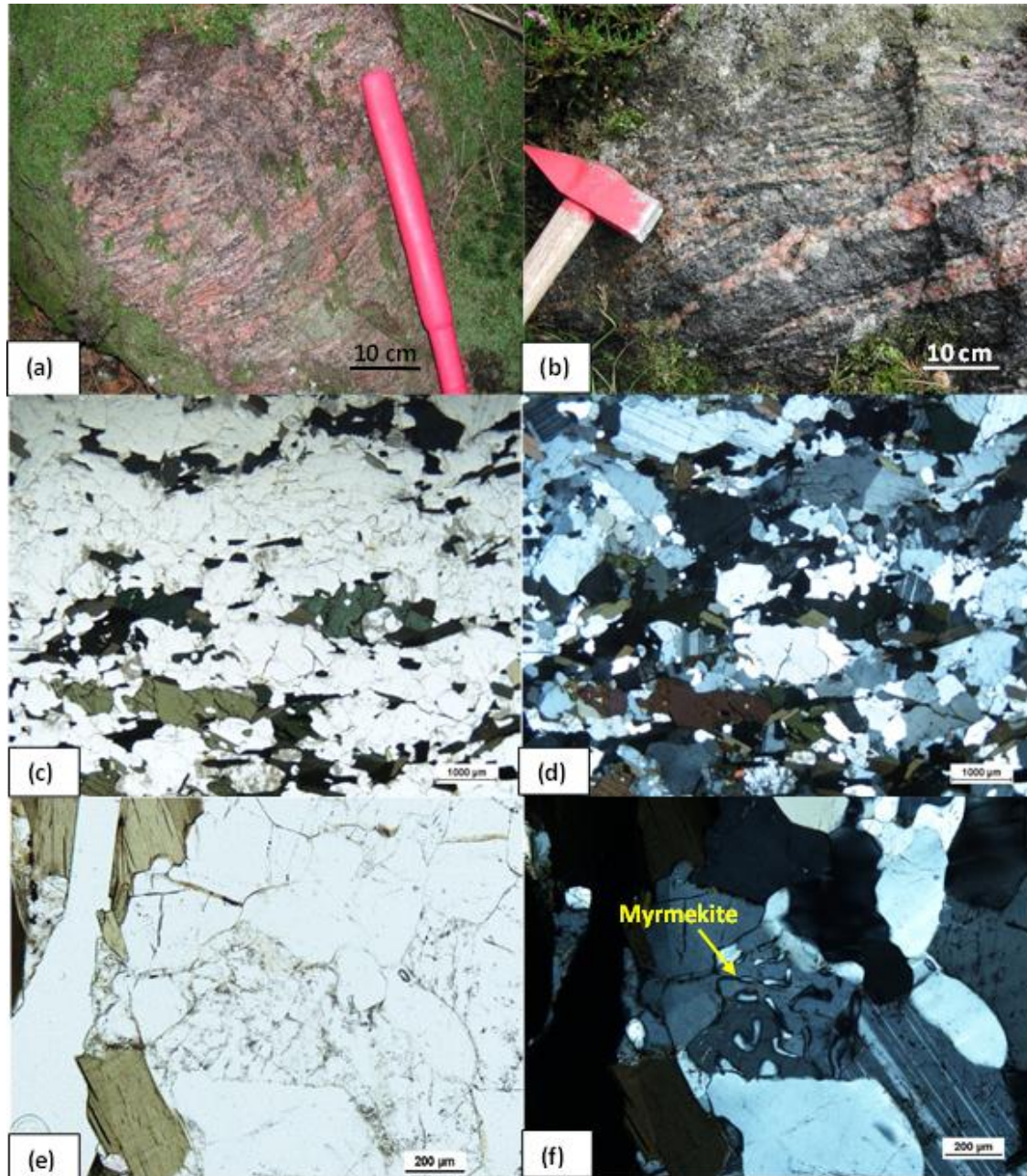
Fig. 6. (a) Reddish grey orthogneiss with reddish leucosome parallel to the gneissic foliation, locality 95. (b) Reddish grey orthogneiss with leucosome of red feldspar and quartz, locality 24. (c)-(f) Photomicrographs of grey orthogneiss, sample NMA11016a. (c) PPL, Plagioclase, quartz, antiperthite, biotite and hornblende with accessory zircon and opaques. (d) CPL, same view as in c. (e) PPL, Fine-grained myrmekite in the matrix in contact with plagioclase and quartz. (f) CPL, same view as in e.

11

hornblende, biotite and myrmekite in places along with accessory zircon and opaques. The rock has an inequigranular texture with subhedral grain boundaries (Fig. 6c-f). Hornblende and biotite grains are strained while the other minerals show little internal strain. Plagioclase and quartz are inequigranular and up to 10 mm large. Hornblende is pleochroic green- brown colors. Saussuritization occurs locally in plagioclase.

4.2.2   Sample NMA11125 Reddish grey orthogneiss

This sample was collected from the mesosome of the reddish grey orthogneiss characterized by a granoblastic texture composed of plagioclase, hornblende, quartz, biotite and accessory opaques. Biotite and hornblende grains define weak foliation of the rock (Fig. 7a & b). Restricted saussuritization within plagioclase is also visible. Chlorite has formed locally as alteration of biotite (Fig. 7c & d).

4.3   Porphyritic Torpa-type granite-augen gneiss

K-feldspar porphyritic granite in various states of deformation forms two lens-shaped bodies situated in the northernmost and central parts of the mapped area (Fig. 3). It is composed of K-feldspar, quartz and plagioclase, with a lesser amounts of biotite, hornblende and opaque minerals. The granite is well-preserved in the center of the lens, but foliated towards the margins (Fig. 8a & b). Large orthoclase crystals form an interlocking texture, which makes the rock competent to deformation. These characteristics along with the reddish hue of the rock are the most outstanding properties of the Torpa-type granite. Recrystallization of orthoclase to microcline is prevalent. Migmatization can be seen in places but it is not abundant. Augen gneiss is the most common deformed variety of the porphyritic Torpa granite (Fig. 8b); locally it has been sheared (Fig. 30).

4.3.1   Sample NMA11001 Augen gneiss

This sample represents a strongly deformed augen gneiss made up of K-feldspar, plagioclase and quartz with lesser amounts of hornblende-biotite aggregate. Plagioclase is fine-grained, granoblastic and intergrown with matrix microcline. Partial recrystallization of the rock can be inferred from augen composed of perthitic K-feldspar surrounded by recrystallized subgranoblastic microcline (Fig. 8c & d). Carlsbad twinning of orthoclase, tartan twinning of microcline and wave-like perthite lamellae are visible in the thin sec-
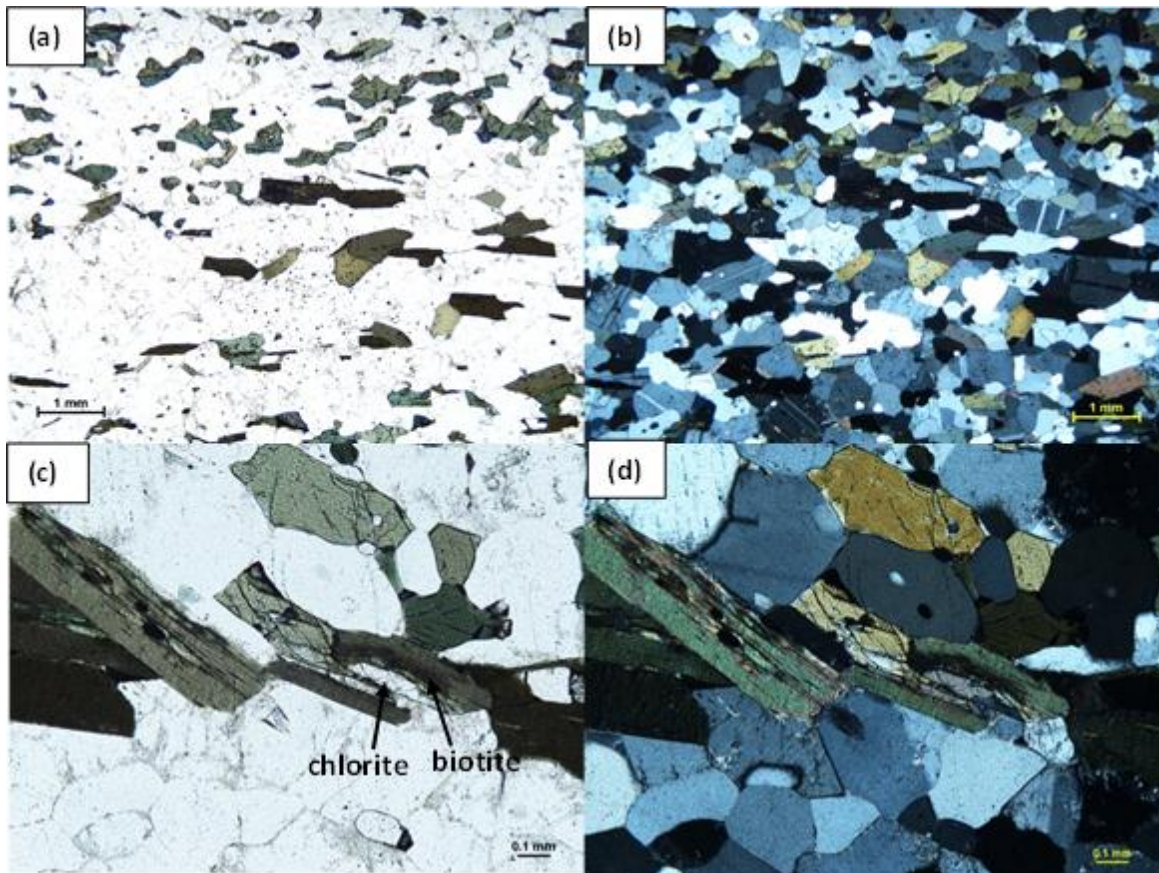
Fig. 7. (a)-(d) Photomicrographs of sample NMA11125, intermediate grey mesosome of reddish grey orthogneiss. (a) PPL, Granoblastic texture with plagioclase, hornblende, quartz, biotite and chlorite. (b) CPL, same view as in a (c) PPL, Biotite alteration to chlorite (d) CPL, same view as in c.
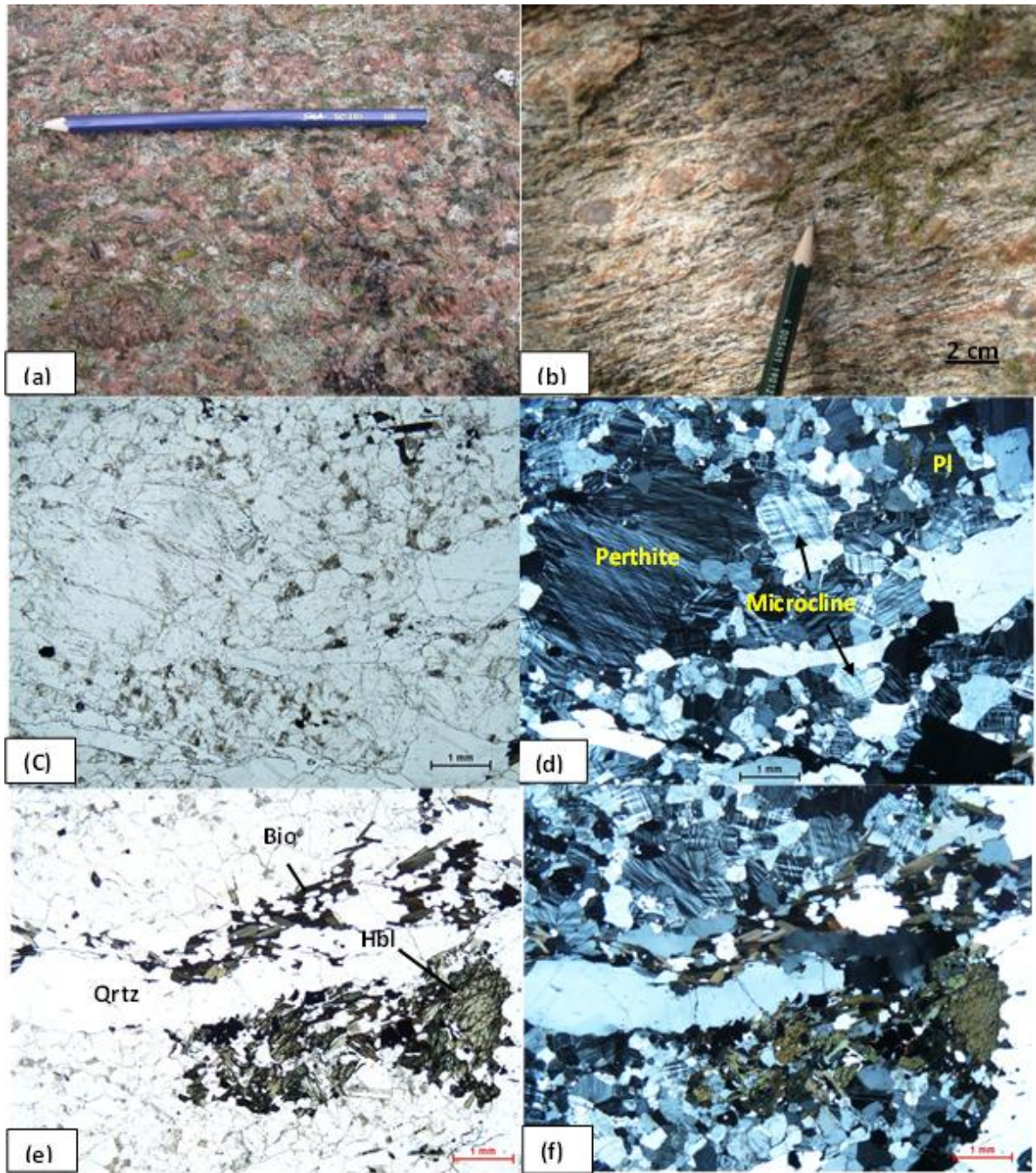
Fig. 8. Torpa-type granite. (a) Well-preserved K-feldspar porphyritic granite in the centre of a lens-shaped body, locality 1. The pencil length is 18 cm. (b) Augen gneiss in the margin of the Torpa granitic body, locality 1. (c)-(f) Photomicrographs of sample NMA11001, Well-preserved K-feldspar porphyritic granite. (c) PPL, Perthite megacryst enclosed within subgranoblastic microcline, plagioclase and quartz. (d) CPL, same view as in c. (e) PPL, Elongated quartz aggregate in the middle of the photo surrounded by hornblende, K-feldspar, plagioclase, biotite and quartz. (f) CPL, same view as in e.

tion (Fig. 8d). There is strongly elongated quartz with length to width ratios > 10 (Fig. 8e & f). Fine-grained saussurite occurs in plagioclase.

4.4 Retro-eclogite

4.4.1 Sample NMA11029 Retro-eclogite

The retro-eclogite body is shown in the map (Fig. 3) with some exaggeration since the outcrop was only about 30 m^2. The retroeclogite is situated within the mylonitic gneiss (Fig. 9a) and composed of garnet, clinopyroxene, kyanite, sapphirine, hornblende and plagioclase (Fig. 9b & c). Greenish grey clinopyroxene is dominant in the matrix. Small grains of plagioclase are hosted by clinopyroxene (Fig. 9d & e). Kyanite is absent in the thin section but visible in the field (Fig. 8a). Indicators of the former presence of kyanite are symplectites of sapphirine + plagioclase (Fig. 9f & g; cp. Möller 1999). Garnets have partially developed

13
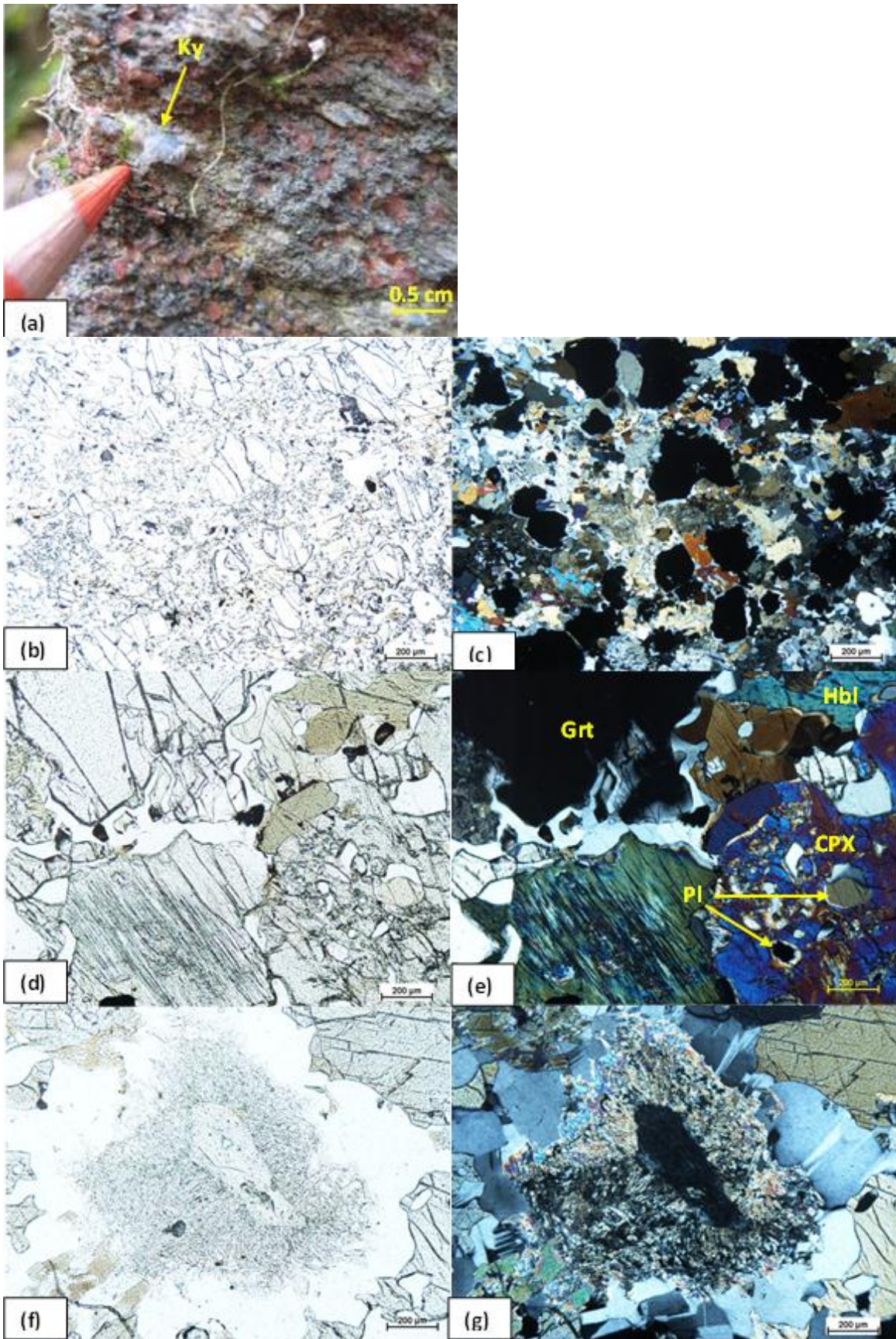
Fig. 9. (a) Kyanite-bearing retroeclogite, locality 29. (b)-(g) Photomicrographs of sample NMA11029. (b) PPL, Garnet, pyroxene, plagioclase, hornblende and quartz. (c) CPL, same view as in b. (d) PPL, Plagioclase occurs intergrown with pyroxene and as garnet corona. (e) CPL, same view as in d. (f) PPL, Symplectite of sapphirine (pseudomorph after kyanite). (g) CPL, same view as in f.

14

rims of plagioclase in contact with hornblende and clinopyroxene. Sussuritization of plagioclase is visible in places. Plagioclase was interpreted as secondary in relation to the eclogite facies assemblage and formed during decompression at high-pressure granulite and upper amphibolites facies conditions. Hornblende is also formed during post-eclogite conditions and has grown at the expense of clinopyroxene.

4.4.2 Sample NMA11049b Retro-eclogite

The sample was taken from a small retroeclogite occurrence within the mylonitic gneiss layers (exaggerated on the map; Fig. 3). The mineral assemblage is made up of garnet, clinopyroxene, hornblende, biotite, quartz and sussuritized plagioclase (Fig. 10a & b). Clinopyroxene occurs as remnants and has been partiallly replaced by fine-grained hornblende and plagioclase and intergrown with plagioclase (Fig. 10c & d). Garnet is strongly resorbed and replaced by fine-grained plagioclase, chlorite and opaques (Fig. 10e & f).
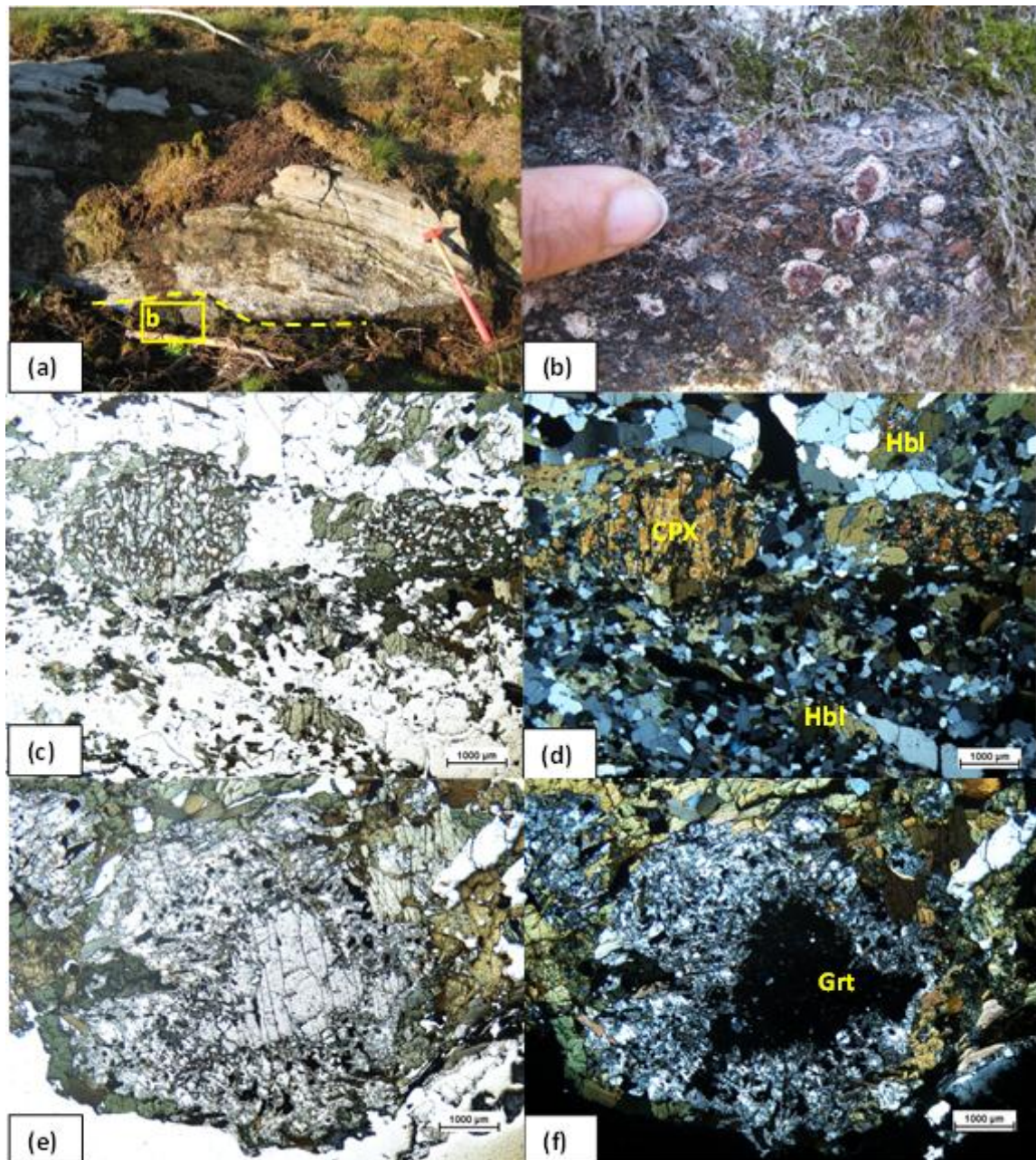
Fig. 10. (a) Outcrop of retroeclogite (below the dashed line) overlainby mylonitic gneiss, locality 49b. Hammer, 64 cm, for scale. (b) Closer view of retroeclogite showing garnet crystals with plagioclase rims (c)-(f) Photomicrographs of sample NMA11049b (c) PPL, Clinopyroxene enclosing plagioclase grains and surrounded by secondary hornblende in a matrix of fine-grained plagioclase and quartz. (d) CPL, same view as in c. (e) PPL, Remnant of garnet replaced by plagioclase, chlorite and opaques. (f) CPL, same view as in e.

15

4.5 Granitic orthogneiss

The granitic orthogneiss is reddish and a moderate to strongly deformed rock with granitic composition, devoid of K-feldspar augen or megacrysts.

4.5.1 Sample NMA11002 Recrystallized granitic gneiss

Collected from the margin of the Torpa granite body, this sample is made up of plagioclase, K-feldspar, quartz and biotite along with scattered accessory grains of garnet, zircon, allanite and opaques (Fig. 11a-d). Microcline is more abundant than in the augen gneiss. Quartz and feldspars are strain-free, forming a granoblastic texture, however with a slight preferred orientation; biotite defines foliation (Fig. 11a & b).   Late local alteration includes chlorite replacement of biotite, and growth of muscovite and saussurite in plagioclase.

4.6 Heterogenous mylonitic gneiss

Intensively layered and very fine-grained mylonitic gneiss with a thickness of 200 to 1200 meters is located in the middle of the study area, trending NNW-SSE and forming a low-elevated farm land area (Fig. 3). Mylonitic gneiss was also observed locally in association with grey orthogneiss and granitic gneiss (mapped as scattered mylonitic gneiss). The laminated rocks are made up of alternating felsic and mafic domains (Fig. 12a), based on field and thin section observation. Amphibolite layers parallel to the mylonitic gneiss foliation is common. The most common porphyroclasts are plagioclase, garnet and hornblende of variable size up to 20 cm (Fig. 12b).

4.6.1 Sample NMA11018 Mylonitic gneiss

A very fine- to medium-grained mafic mylonitic gneiss containing plagioclase, hornblende, quartz and some biotite along with accessory zircon and opaques (Fig. 13). Plagioclase grains are locally saussuritized. Hornblende (Fig. 13a & b) and a few grains of perthite (Fig. 13c & d) constitute porphyroclasts. Due to the abundance of mafic minerals, felsic banding is not apparent in the hand specimen, but in the thin section felsic domains of plagioclase and quartz are distinguishable. Dark minerals are oriented and form a foliation, whereas plagioclase and quartz are subgranoblastic. Hornblende is pleochroic green and brown, in places patchy in appearance (Fig. 13a-b).
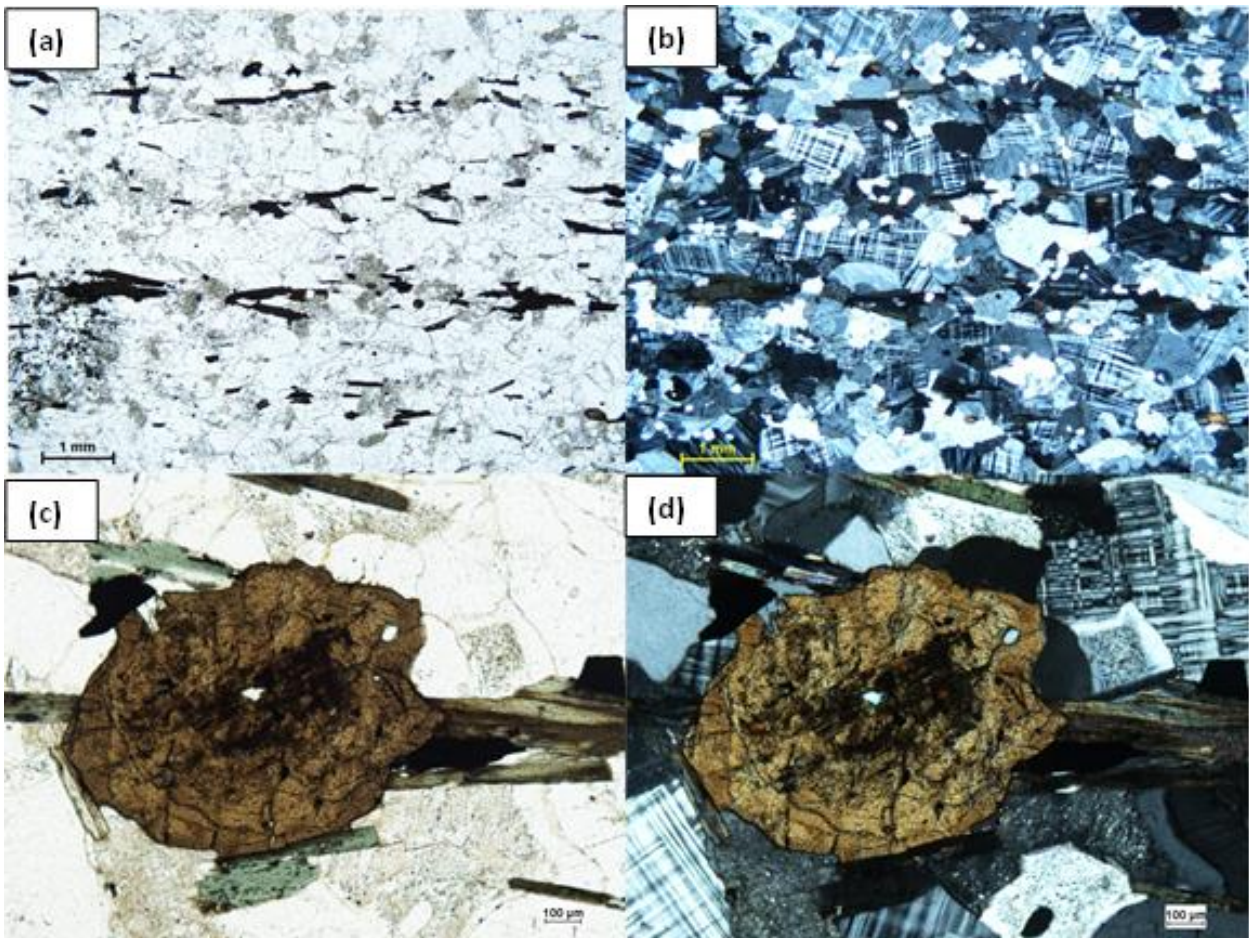
Fig. 11. (a)-(d) Photomicrograph of sample NMA11002, Granitic gneiss. (a) PPL, Plagioclase, orthoclase, microcline, perthite, biotite. (b) CPL, same view as in a. (c) PPL, The brown mineral is allanite. (d) CPL, same view as in c.
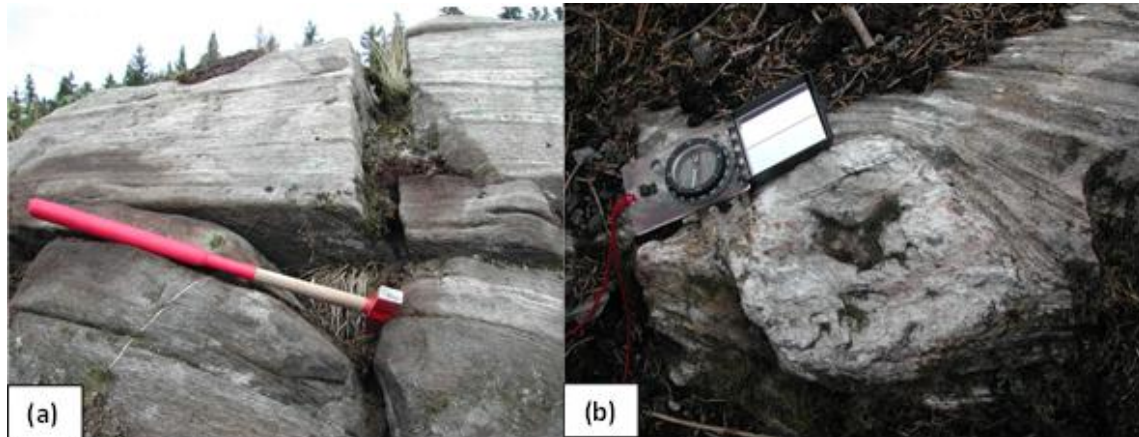
Fig. 12. (a) Fine-grained and intensely layered mylonitic gneiss, locality 19. The hammer (64 cm) marks the boundary between a mafic rock (below) and a felsic rock (above). (b) A large size porphyroclast of plagioclase in the mylonitic gneiss. Locality 49a. The compass length is 17 cm.

4.6.2 Sample NMA11019 Mylonitic gneiss

The mylonitic gneiss consists of recrystallized ribbon quartz in a granoblastic matrix of equigranular fine-grained plagioclase, subhedral hornblende and biotite. Hornblende with some scattered and resorbed garnet remnants form lens-shaped, slightly larger grains (Fig. 14 a-b). The foliation is defined by preferentially oriented mineral aggregates such as ribbon quartz, biotite and hornblende (14c & d).

4.6.3 Sample NMA11052a Mylonitic gneiss

The sample is a finely layered mylonitic gneiss composed of ribbon quartz in a matrix of granoblastic plagioclase, hornblende and small biotite (Fig. 15 a-f). Hornblende and biotite grains which in places occur as aggregates define the foliation along with quartz ribbons. Hornblende is pleochric in brown and green colors (Fig. 15c & d). Accessory minerals include zircon (Fig. 15e & f) and opaques. Saussuritization
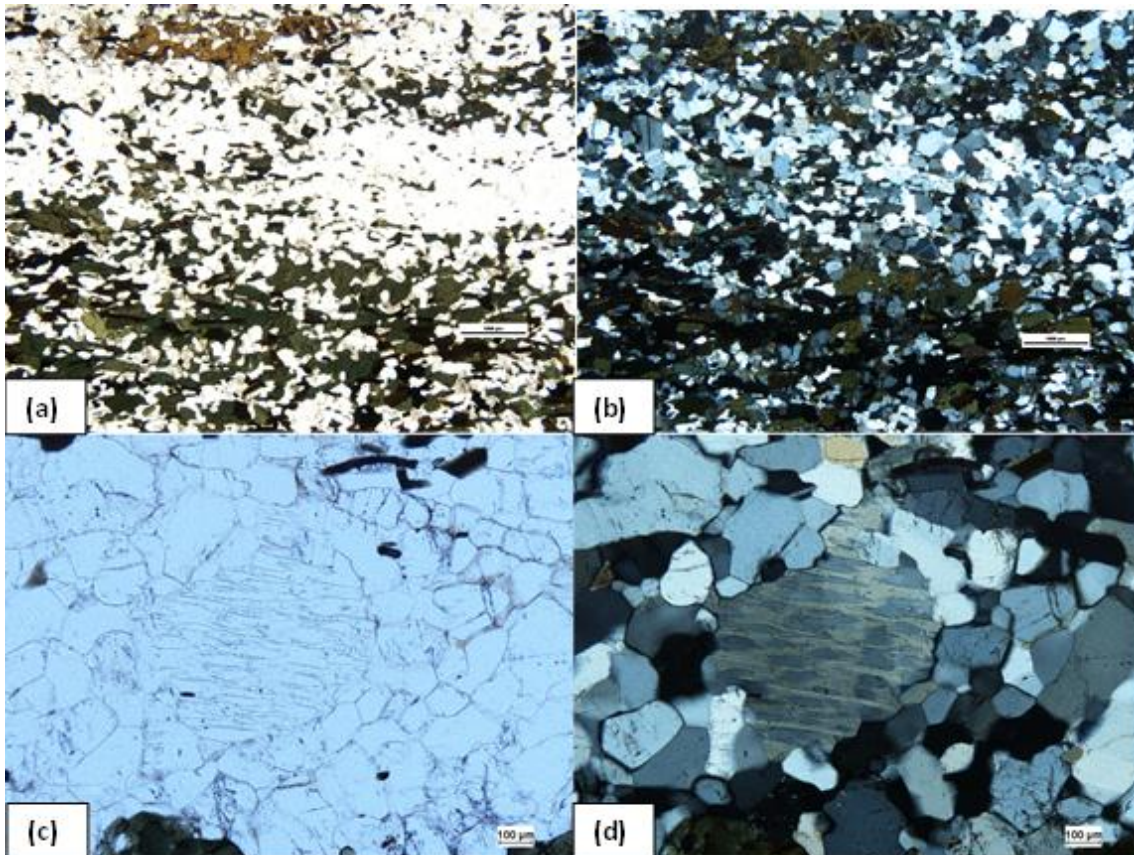
Fig. 13. (a)-(d) Photomicrographs of mylonitic gneiss, sample NMA11018. (a) PPL, Dark and mesocratic bands composed of plagioclase, quartz, hornblende, biotite. (b) CPL, same view as in a. (c) PPL, Perthitic feldspar as porphyroclast surrounded by finer grained plagioclase and quartz. (d) CPL, same view as in c.

occurs locally in plagioclase. Biotite is altered to chlorite in places.

4.6.4   Sample NMA11087 Mylonitic gneiss

This sample is a mylonitic gneiss with up to 5 mm sized porphyroclasts of perthitic feldspar, garnet and hornblende in a fine-grained matrix of equigranular plagioclase, biotite, quartz and hornblende with granoblastic texture (Fig. 16a & b). The rock has a strongly laminated structure of alternating felsic and mafic mineral aggregates.

4.6.5   Sample NMA11150 Mylonitic gneiss

The rock is a fine-grained mylonitic gneiss with an intensely developed foliation defined by alternating felsic and mafic mineral aggregates and recrystallized quartz ribbons (Fig. 17a-e). The foliation wraps around strongly resorbed porphyroclasts of garnet up to 5 mm in size, and around one allanite porphyroclast c. 2 mm long. The foliation bands are made up of fine-grained biotite, plagioclase, quartz, hornblende. Sparse remnants of larger sized grains clinopyroxene and scapolite occur in the foliation bands (Fig. 17d & e).

4.6.6   Sample NMA11155 Mylonitic gneiss

This rock is a mylonitic gneiss of mafic to intermediate composition, which were collected within the migmatitic grey gneiss unit. It is composed of abundant garnet, clinopyroxene, antiperthitic plagioclase, hornblende and biotite (Fig. 18a-d). The dark minerals occur in thin elongated aggregates alternating with plagioclase aggregates and quartz ribbons. The minerals show no or very little internal strain but form subgranoblastic or irregular grain shapes. There are fine greenish minerals in the thin section possibly formed after scapolite alteration (Fig. 18d & e). Elongated quartz show width: length ratio of c. 1:15 (Fig. 18b & c). Biotite occurs in elongated aggregates.

4.7   Torpa-type mylonitic gneiss

4.7.1   Sample NMA11054c Torpa-type mylonitic gneiss

Taken from the marginal part of the Torpa granite-augen gneiss, the sample is made up of very fine grained quartz, plagioclase, K-feldspar (granoblastic crypto-perthite) and accessory grains of opaques,
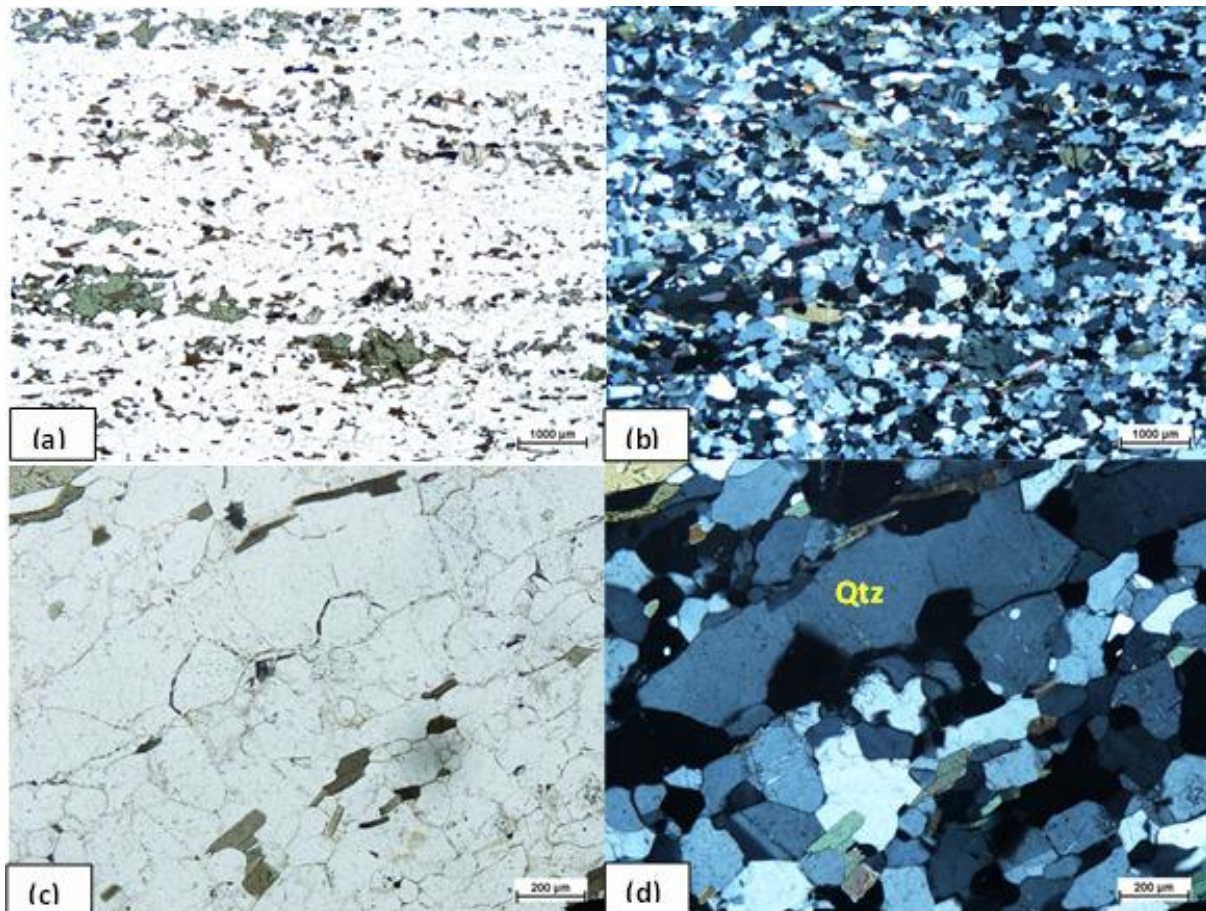
Fig. 14. (a)-(d) Photomicrographs of sample NMA11019. (a) PPL, Fine-grained quartz, plagioclase, biotite and hornblende, with some larger grains of hornblende. (b) CPL, same view as in a. (c) PPL, Elongated quartz ribbon surrounded by granoblastic plagioclase and biotite. (d) CPL, same view as in c.

Fig. 15. (a)-(f) Photomicrographs of mylonitic gneiss, sample NMA11052a. (a) PPL, Dark and light bands composed of different proportions of plagioclase, hornblende and biotite and conspicuous quartz ribbons. (b) CPL, same view as in a. (c) PPL, Plagioclase, quartz, hornblende and biotite. Hornblende is brown-green pleochroic. (d) CPL, same view as in c. (e) PPL, Granoblastic plagioclase with local saussuritization. Small zircon grain in the center of the photo. (f) CPL, same view as in e.

garnet, zircon along with rare occurrences of hornblende and biotite. In the field, the rock is similar to the granitic gneiss due to its reddish color and intense foliation. Considering the presence of igneous perthitic orthoclase, which is typical for the Torpa granite, the rock, however, was interpreted as a mylonitic gneiss variety of the Torpa-type granite. The elongation of mineral aggregates suggests high strain: some quartz ribbons are elongated with width: length ratios of at least 1:20 (Fig. 19a & b). Plagioclase shows local saussuritization. Grain size reduction is

notable where remnants of coarser perthite are surrounded by recrystallized plagioclase and quartz (Fig. 19c & d).

4.8 Garnet-rich amphibolite

Garnet-rich amphibolite is not shown as an individual unit on the map, since it occurs as small lenses within the other rocks (Torpa granite and migmatitic grey orthogneiss). Garnet is commonly surrounded by a fine-grained corona of plagioclase (Fig. 20a).

4.8.1 Sample NMA11055 Garnet-rich amphibolite

This sample represents garnet-rich and migmatized amphibolite within the Torpa granite-augen gneiss. The rock is taken from a 15 × 20 m body and contains garnet, hornblende and plagioclase, with small amounts of clinopyroxene, quartz and titanite (Fig. 20b & c). Plagioclase occurs intergrown with garnet and hornblende in the matrix but also as fine-grained intergrowths with opaques along the resorbed rims of garnet. Clinopyroxene is commonly anhedral, locally intergrown with plagioclase and partly replaced by hornblende. Weak saussuritization can be seen in plagioclase.

Fig. 16. (a) Scanned thin section of sample NMA11087, Mylonitic gneiss showing strongly elongated and alternating felsic and mafic domains with resorbed porphyroclasts of garnet and hornblende. (b) Photomicrograph of the same sample, CPL, Hornblende and garnet megacrysts in a fine-grained matrix of plagioclase, biotite, quartz and hornblende.
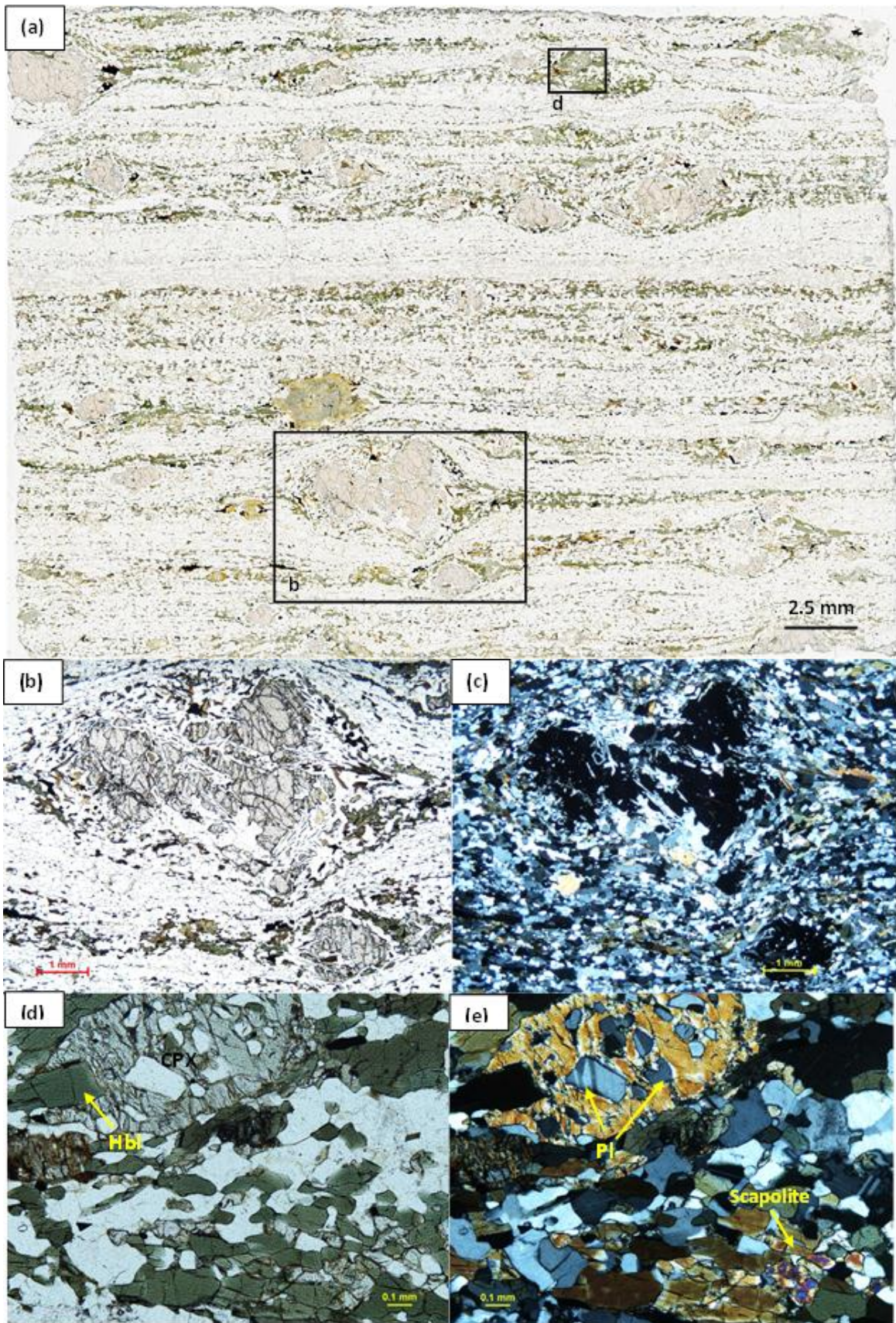
Fig. 17. (a) Scanned thin section of sample NMA11150, garnet rich mylonitic gneiss. (b)-(e) Photomicrographs of sample NMA11150, mylonitic gneiss (b) PPL, Two resorbed garnet megacrysts in a matrix of fine-grained plagioclase, biotite, hornblende and quartz. (c) CPL, same view as in b. (d) PPL, Clinopyroxene megacryst with plagioclase blebs surrounded by hornblende, plagioclase and scapolite. (e) CPL, same view as in d.

21
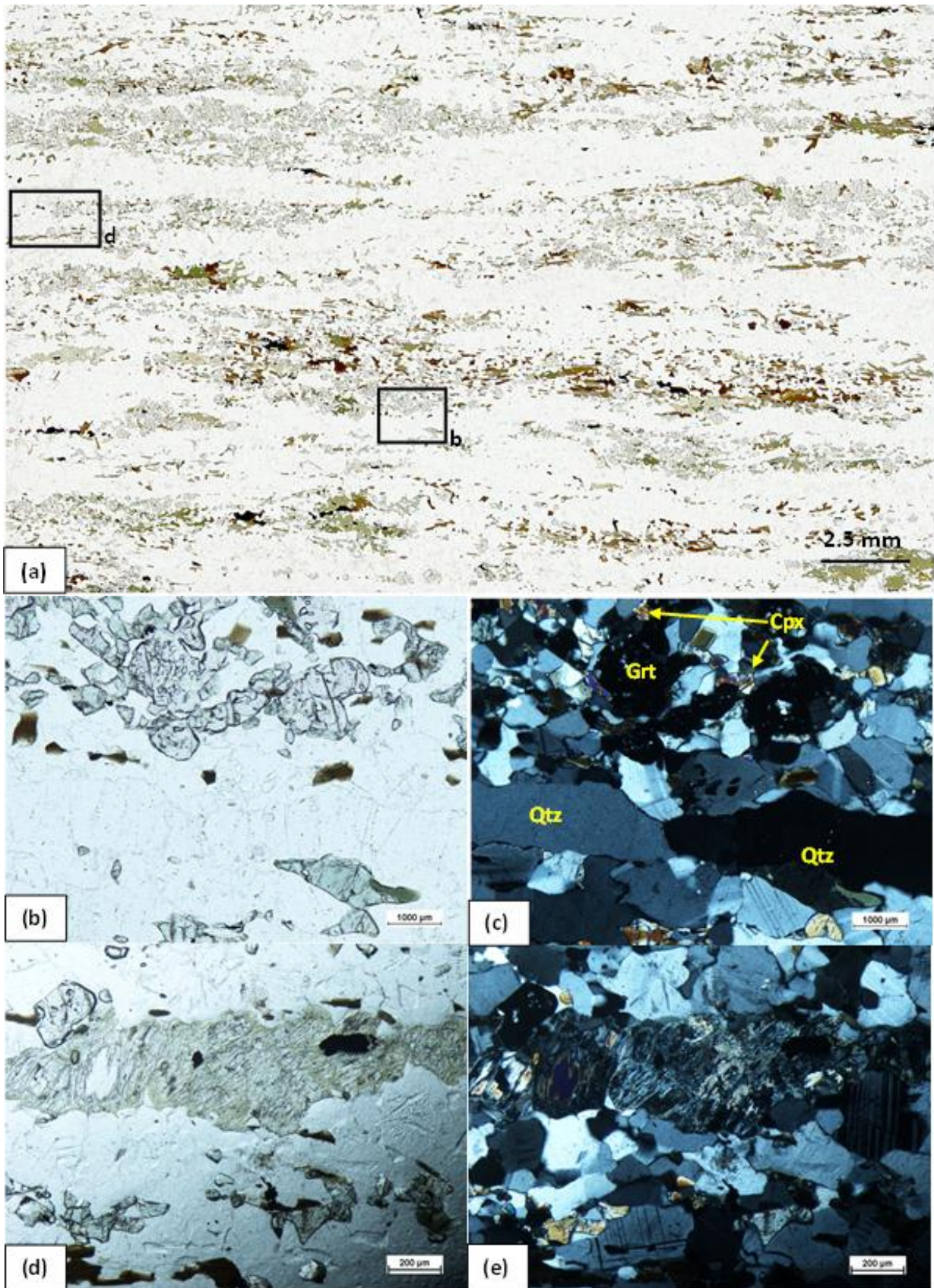
Fig. 18. (a) Scanned thin section of sample NMA11155. Mylonitic gneiss with a strong deformation fabric. (b)-(e) Photo-micrographs of the same sample (b) PPL, Plagioclase, garnet, clinopyroxene, quartz, biotite and hornblende. (c) CPL, same view as in b. (d) PPL, Scapolite aggregate with fine-grained alteration by chlorite. (d) CPL, same view as in d.
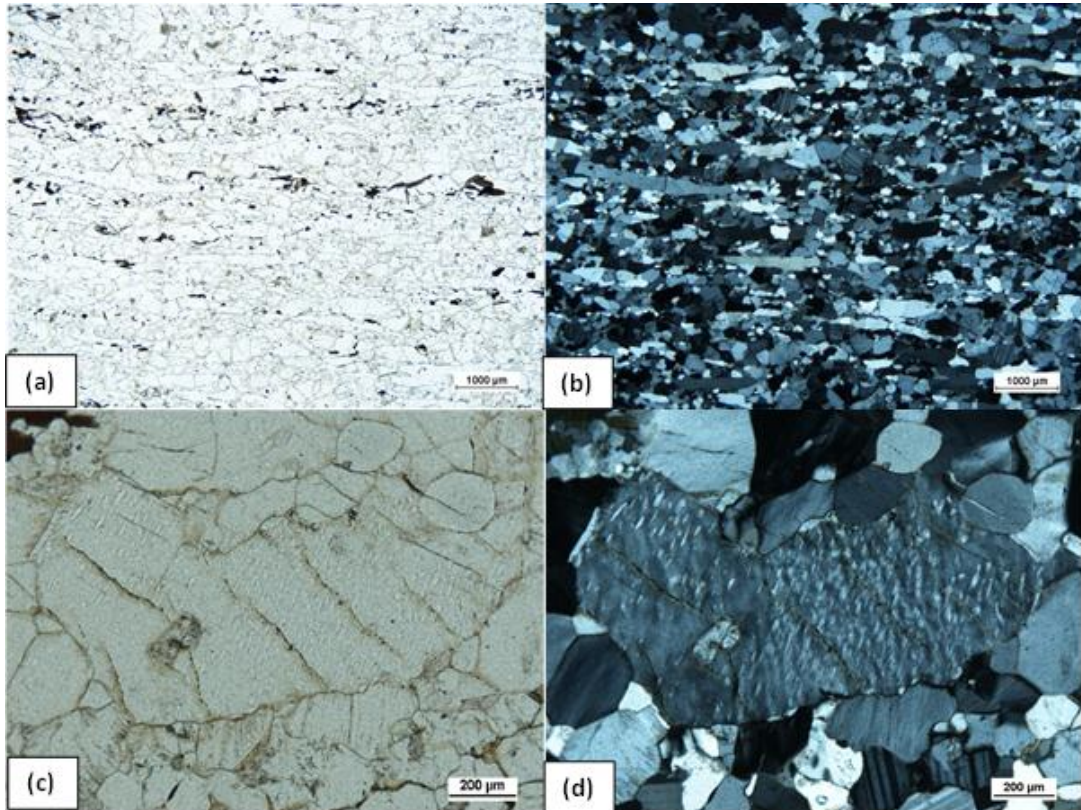
Fig. 19. (a)-(d) Photomicrograph of sample NMA11054c, Torpa-type mylonitic gneiss. (a) PPL, Quartz, plagioclase, K-feldspar with accessory grains of opaques, garnet, zircon and rare hornblende and biotite. (b) CPL, same view as in a. (c) PPL, Perthite megacryst surrounded by recrystallized plagioclase and quartz. (d) CPL, same view as in c.
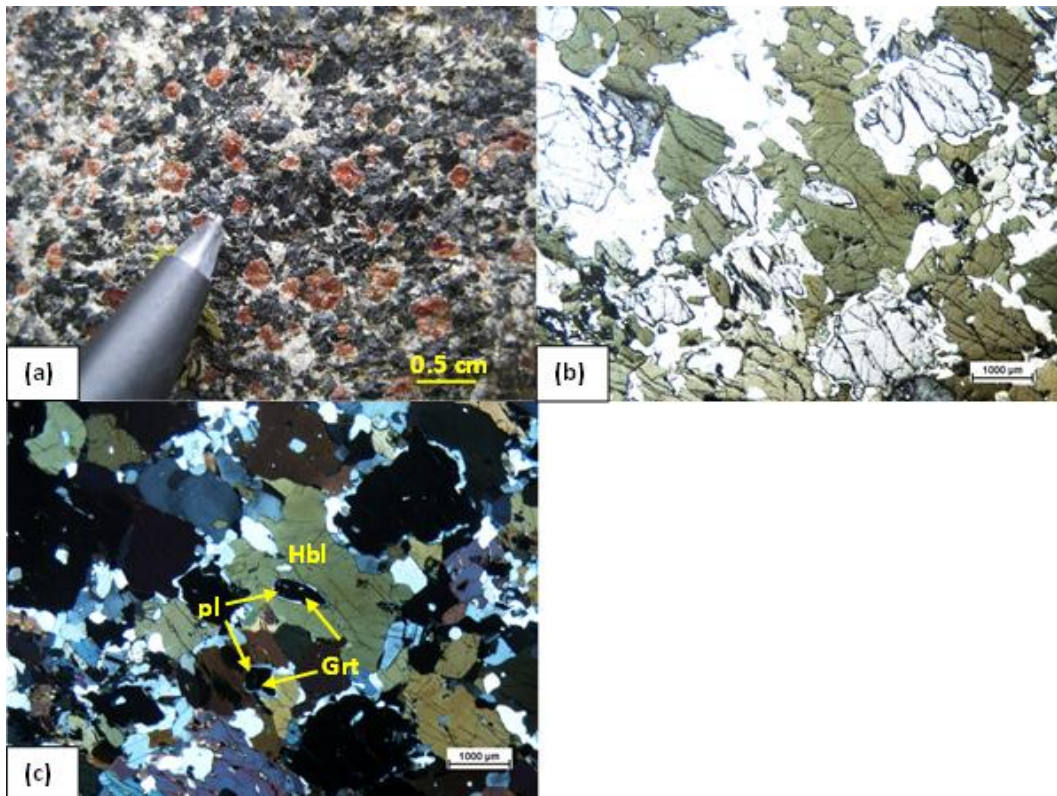
Fig. 20. (a) Garnet-rich amphibolite lens in Torpe granite-augen gneiss, locality 55. Note plagioclase coronas around garnet. (b)-(c) Photomicrographs of the same sample (b) PPL, Garnet, clinopyroxene, hornblende and plagioclase. (c) CPL, same view as in b.

5 Structure

5.1 Structural map

As described in chapter 3, the study area is characterized by strong deformation (Fig. 22). Competency contrasts of the different rocks have resulted in a variety of strain state and a heterogenous structural pattern.

The most competent rock is the porphyritic Torpa granite, which forms two lens-shaped NNW-SSE-striking bodies in the northernmost and central parts of the mapped area. As previously described by Ekdahl (2001), the granite is better preserved in the central parts of the lenses but increasingly foliated towards the margins. The lenses of Torpa granite-augen gneiss are wrapped by grey orthogneiss and granitic gneiss. Migmatitic grey orthogneiss demonstrates high-grade metamorphism and strong deformation, resulting in extensive migmatization and tight to isoclinal folding. The granitic gneiss has been less competent than the Torpa granite. Accordingly, the shape of the Torpa bodies has locally controlled the orientation of the surrounding granitic gneiss foliation particularly in the western contact between Torpa and granitic gneiss (Fig. 22).
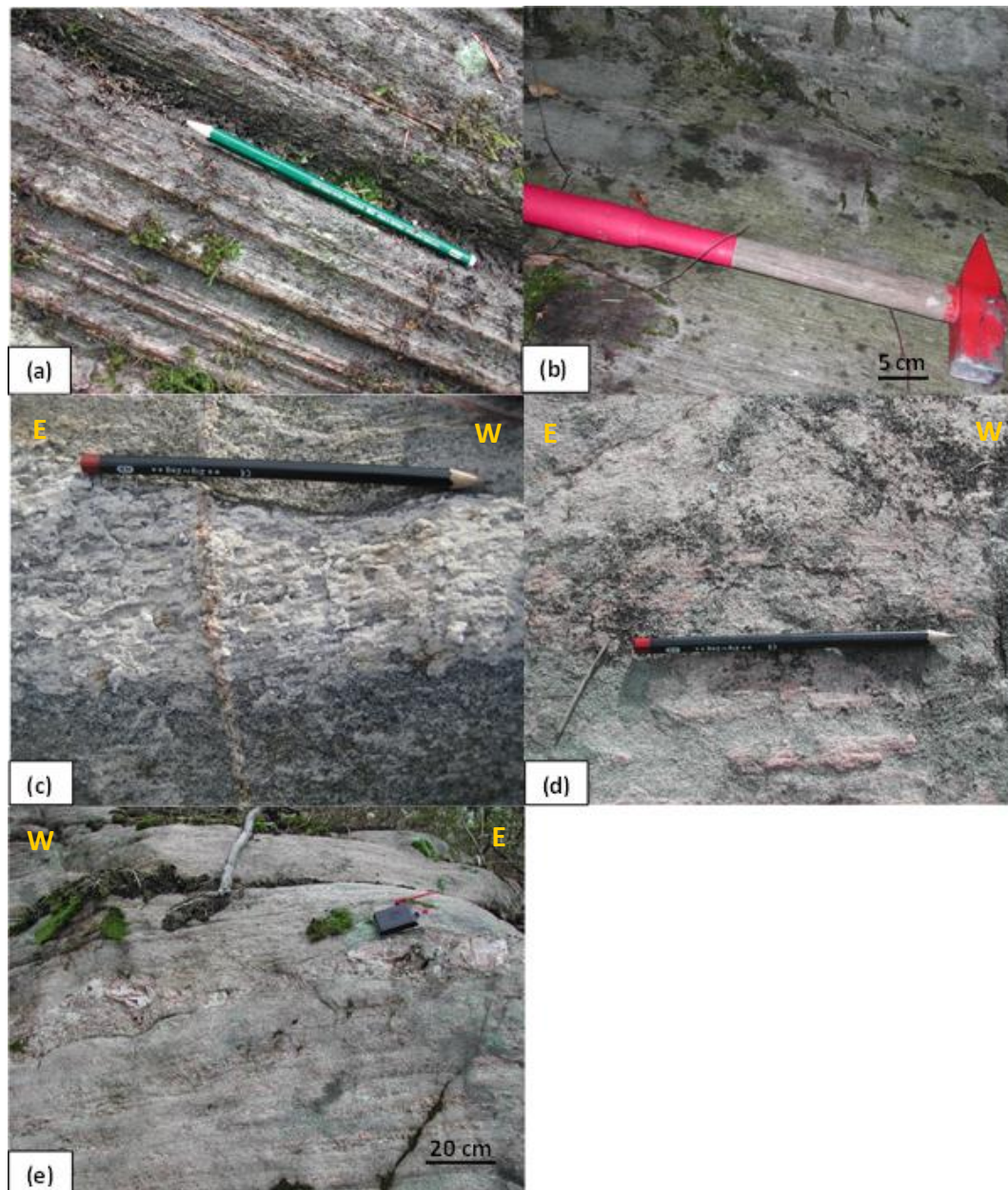
Fig. 21. (a) Foliation in the mylonitic gneiss, locality 92. (b) Foliation in mylonitic gneiss, locality 83. (c) Stretching lineation defined by quartz and feldspar ribbons, locality 19. (d) Stretching lineation defined by aggregates of recrystallised K-feldspar, locality 39. (e) Boudinaged leucosome of quartz, k-feldspar and plagioclase aggregates in a vertical S-facing outcrop in reddish grey gneiss, locality 137. Pencil length is 16 cm.
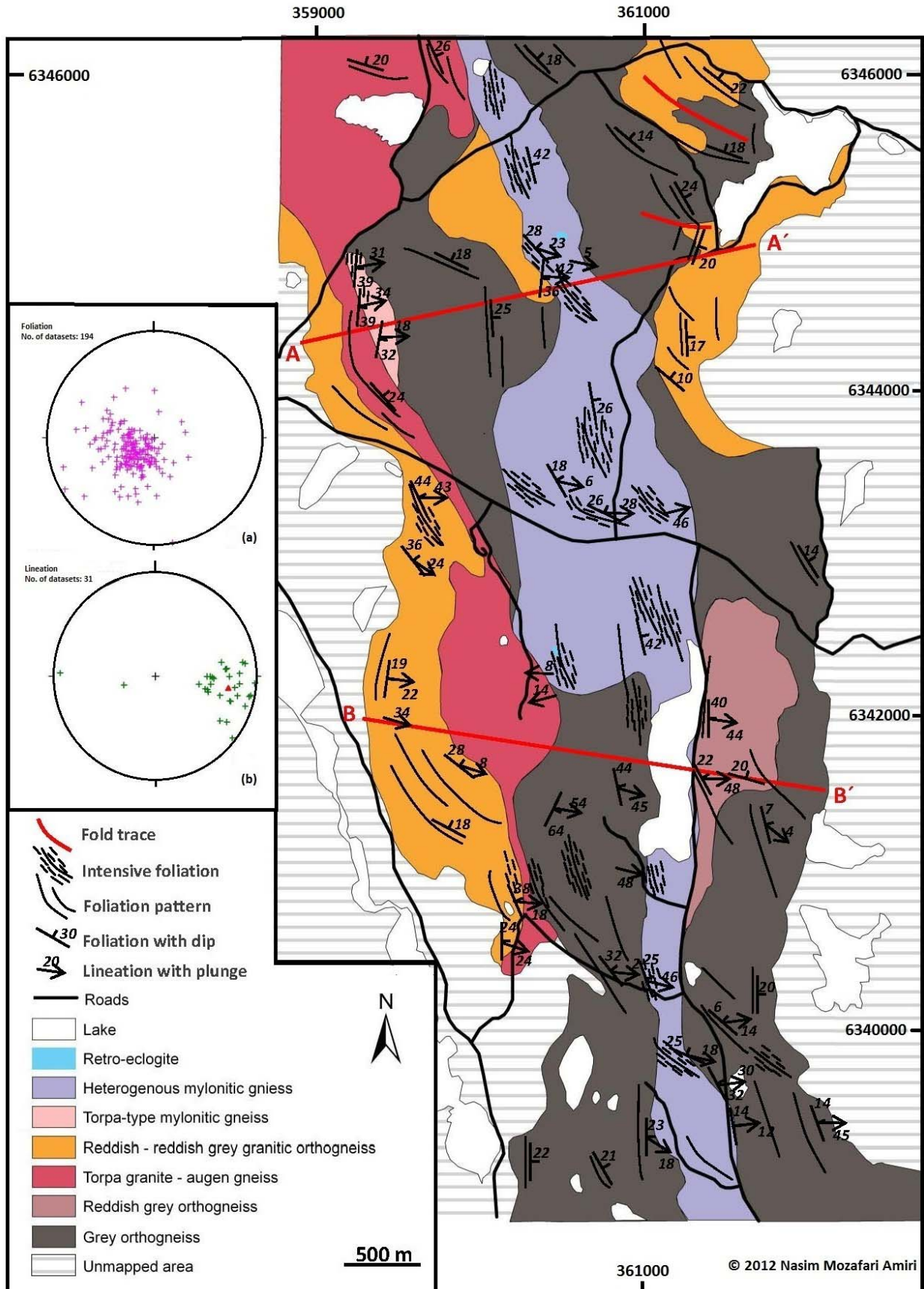
Fig. 22. Structural map showing strike lines and representative orientations of the foliation and lineation along with Lambert equal area stereonet plots of (a) foliations (poles to planes) and (b) stretching lineations. The red triangle represents the mean of measured lineations (099/28).

25

North transect

SW 255°

A 10 36   11 24 19   20   44   23   26   A'

South transect

NW 280°   SE 100°

B 19   11   40   16   11   11   20   B'

Lake

Torpa granite - augen gneiss	Heterogenous mylonitic gneiss
Reddish grey orthogneiss	Torpa-type mylonitic gneiss
Grey orthogneiss	Reddish - reddish grey granitic orthogneiss
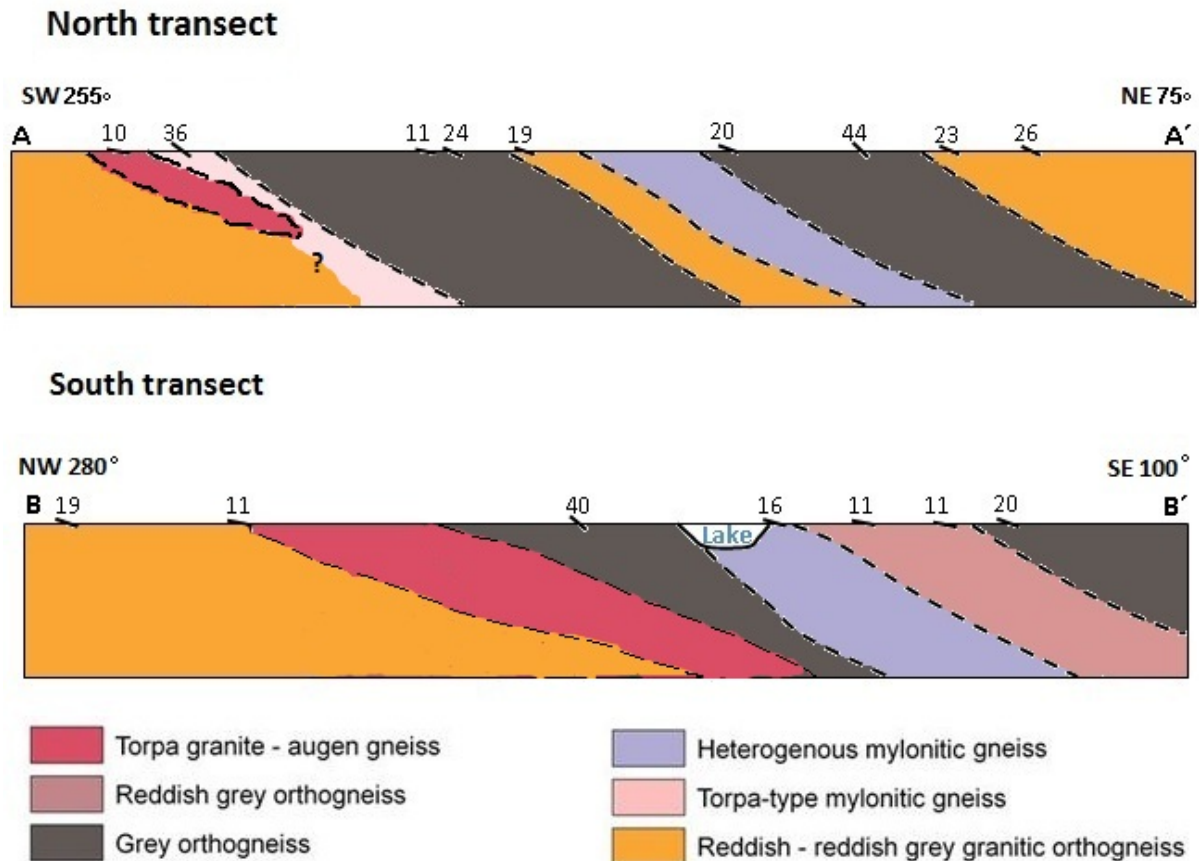
Fig. 23. Cross-sections (locations in Fig. 22). The numbers represent apparent dips of the foliations. Scale 1:20000. Vertical scale was exagerrated to better identify the structural features.

Amongst all rock types, both varieties of mylonitic gneiss (chapter 3) show the most intensive foliation. The heterogeneous mylonitic gneiss extends throughout the map area (7 km) with a thickness of 200 to 1200 meters. The strain is reflected in recrystallization of all previous minerals, except single porphyroclasts. In a narrow domain in the eastern part, where two lens-shaped bodies of the Torpa granite connect, Torpa-type mylonitic gneiss is situated. It differs from the heterogenous mylonitic gneiss in terms of its granitic composition and the presence of porphyroclasts of perthitic orthoclase, which is common in the Torpa granite (Fig. 22).

5.2 Foliations

Gneissic foliation and parallel gneissic layering make a penetrative planar fabric. Compositional banding of dark mafic (locally amphibolite bands) and light felsic phases is common (Figs. 4a, 21a & b, 27c, e, f). Foliations generally strike N-S to NNW-SSE (cp. also the airborne magnetic map, Fig. 2), and dip moderately towards the east or northeast. There are also minor ESE-WNW striking foliation dipping towards north or northeast (Figs. 22 & 23). In the cross-sections (Fig. 23), apparent dip is shown where the strike of the foliation is not perpendicular to the section. In some localities, the foliation was folded into isoclinal folds (Fig. 28b-c, 29a-c).

5.3 Lineations

Stretching lineations are commonly polycrystalline aggregates of quartz or K-feldspar (Fig. 21c & d). They generally trend E-W (in the range between 78° to 128°) and with the exception of two west plunging measurements in the Torpa granite (location 49c & 74), all lineations are east-plunging (Fig. 22). In the reddish grey orthogneiss, a E-W trending leucosome composed of quartz, K-feldspar and plagioclase aggregates is boudinaged, coincident with the trend of lineations (Fig. 21e).

5.4 Shear sense indicators

Indications of shear was observed in both map and outcrop scales. In the map scale, the pinched out Torpa granite body extends from NNW to SSE parallel to the Svarten zone. In outcrop scale, shear structures include displaced foliations, sheared and dissected folds, sigma and delta clasts and asymmetric amphibolite lenses (Figs. 24, 25, 26 & 27). Shear sense indicators were

26
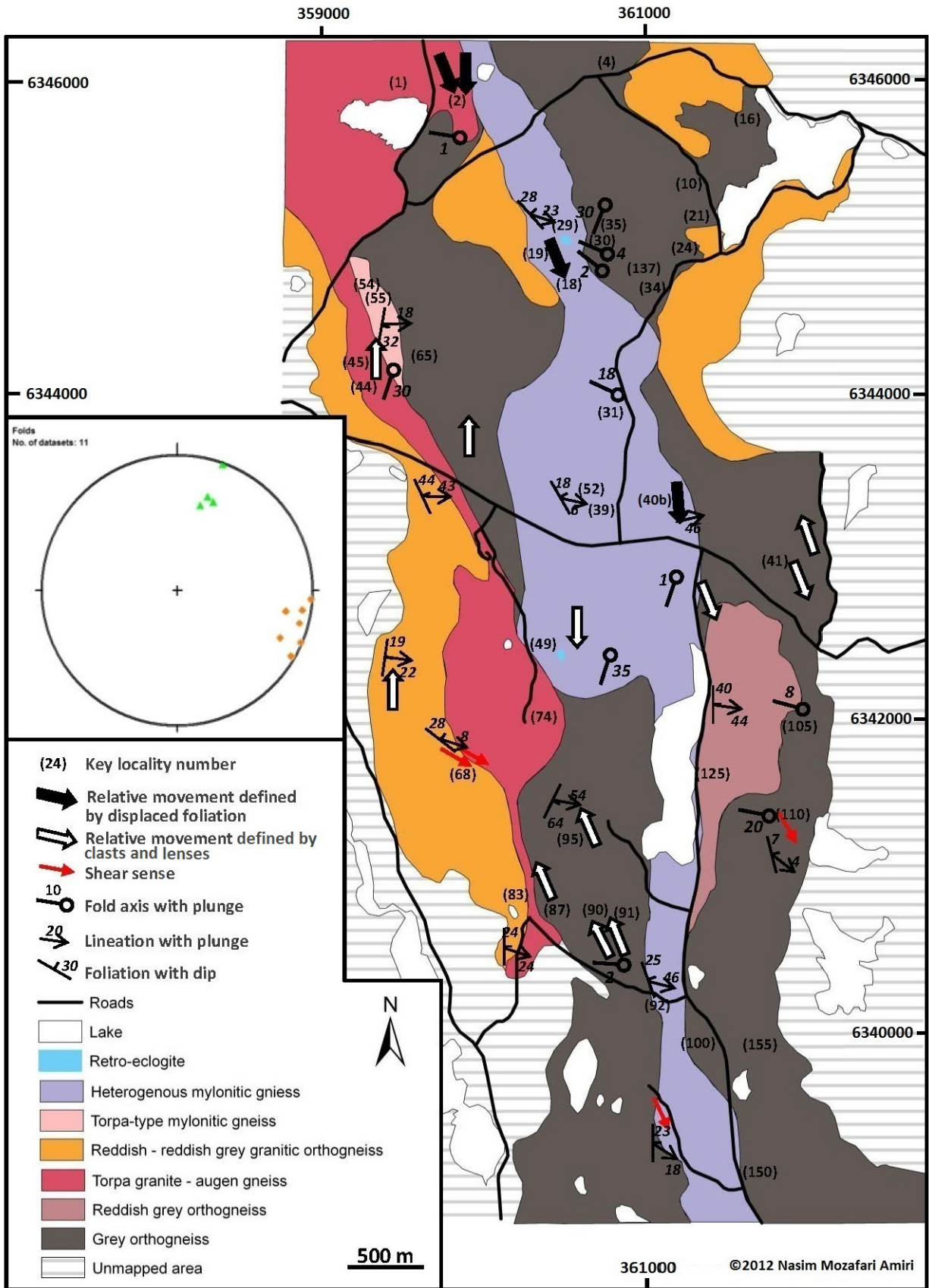
Fig. 24. Structural map showing fold axes, shear sense and apparent relative movement along N-S vertical sections along with plot of fold axes: orange = intrafolial isoclinal folds, green = upright gentle-open folds. Marked are also dips of foliations and plunge of lineations.

27
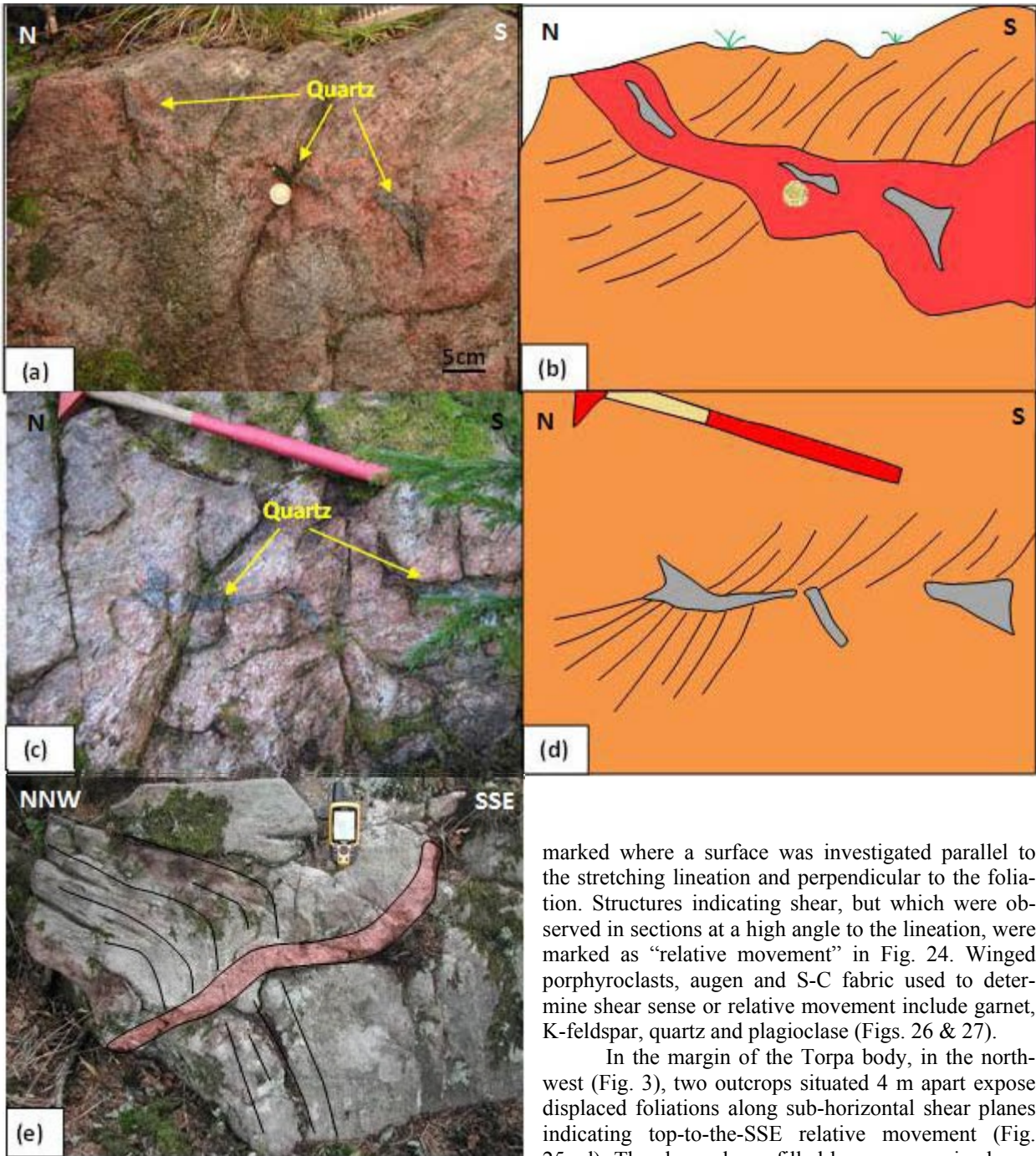
Fig. 25. (a) and (c) Shear planes in the Torpa granite showing top-to-the-SSE relative movement in west-facing outcrops involving dilated quartz minerals, locality 2. (b) and (d) Schematic drawing of photos a and c. Orange = Torpa granite, red = red stained Torpa granite, grey = quartz. The hammer length is 64 cm. (e) Shear plane in the grey orthogneiss filled by coarse-grained granitic minerals which displaced WNW-ESE trending foliations showing top-to-the-SE relative movement, locality 40b.

marked where a surface was investigated parallel to the stretching lineation and perpendicular to the foliation. Structures indicating shear, but which were observed in sections at a high angle to the lineation, were marked as "relative movement" in Fig. 24. Winged porphyroclasts, augen and S-C fabric used to determine shear sense or relative movement include garnet, K-feldspar, quartz and plagioclase (Figs. 26 & 27).

In the margin of the Torpa body, in the northwest (Fig. 3), two outcrops situated 4 m apart expose displaced foliations along sub-horizontal shear planes indicating top-to-the-SSE relative movement (Fig. 25a-d). The shear planes filled by coarse-grained granitic minerals, one is strongly reddish stained, and both localities hosts coarse grained quartz. The shear planes are probably late, syn- or post-kinematic structures (Fig. 25a & b).

A moderately north dipping shear plane, which caused deflection of WNW-ESE foliations in the mylonitic gneiss, with top-to-the-SSE sense of shear was also found. The shear plane was filled by coarse-grained granitic material and interpreted as a late, syn- or post-kinematic feature (Fig. 25e).

28
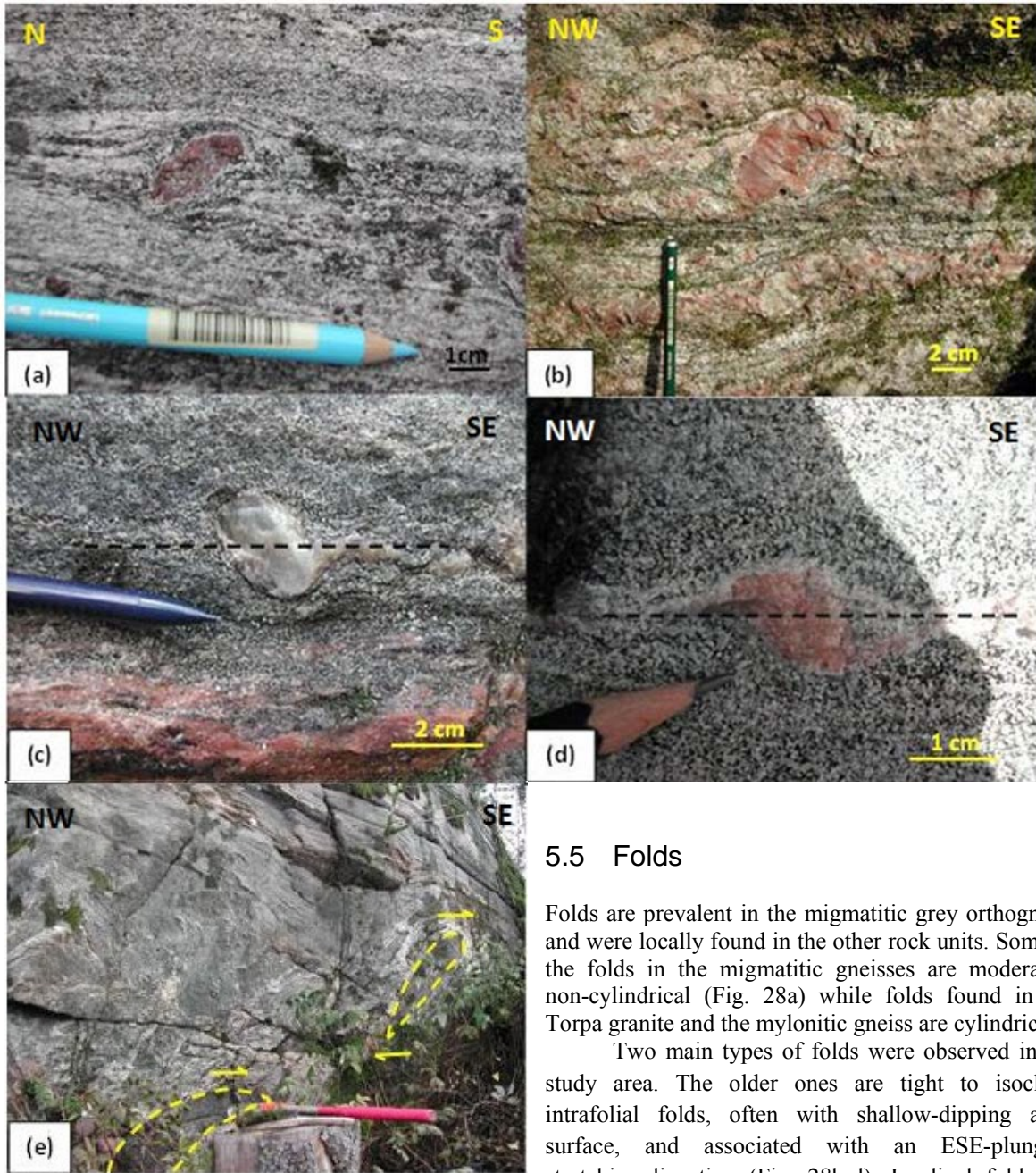
Fig. 26. (a) Garnet porphyroclast in the mylonitic gneiss showing top-to-the-S relative movement in a vertical W-facing outcrop, locality 49b (b) Sigma structure developed on K-feldspar (above) and plagioclase (below) augens with tails of recrystallized material showing top-to-the-SE sense of shear in a SW-facing outcrop in reddish grey gneiss, locality 110. (c) Delta structure of plagioclase porphyroclast in a vertical SW-facing outcrop in the grey orthogneiss showing top-to-the-SE sense of shear, locality 68a (d) Delta structure of K-feldspar porphyroclast in a vertical SW-facing outcrop in the grey orthogneiss showing top-to-the-SE sense of shear, locality 68b. (e) Amphibolite lenses in the grey orthogneiss showing top-to-the-SE. sense of shear in a vertical WNW-facing outcrop, locality 68a. Hammer length is 64 cm.

5.5   Folds

Folds are prevalent in the migmatitic grey orthogneiss and were locally found in the other rock units. Some of the folds in the migmatitic gneisses are moderately non-cylindrical (Fig. 28a) while folds found in the Torpa granite and the mylonitic gneiss are cylindrical.

Two main types of folds were observed in the study area. The older ones are tight to isoclinal intrafolial folds, often with shallow-dipping axial surface, and associated with an ESE-plunging stretching lineation (Fig. 28b-d). Isoclinal folds are found with maximum length of 20 meters in the field. Recumbent chevron-type folds were observed in the mylonitic gneiss and, commonly, in the migmatitic gneiss (Fig. 29). Parasitic folds are very common in association with the isoclinal and chevron folds (Fig. 29a & b). In places, elongated mineral aggregates can be seen in isoclinal fold hinges (Fig. 28e). The younger folds are open to gentle and upright with sub-vertical axial planes and generally sub-horizontal NNE-SSW trending fold axes in scales from 1 to 20 m (Figs. 24 & 28g); minor gentle folds occur with ESE-plunging axes (Fig. 28f).
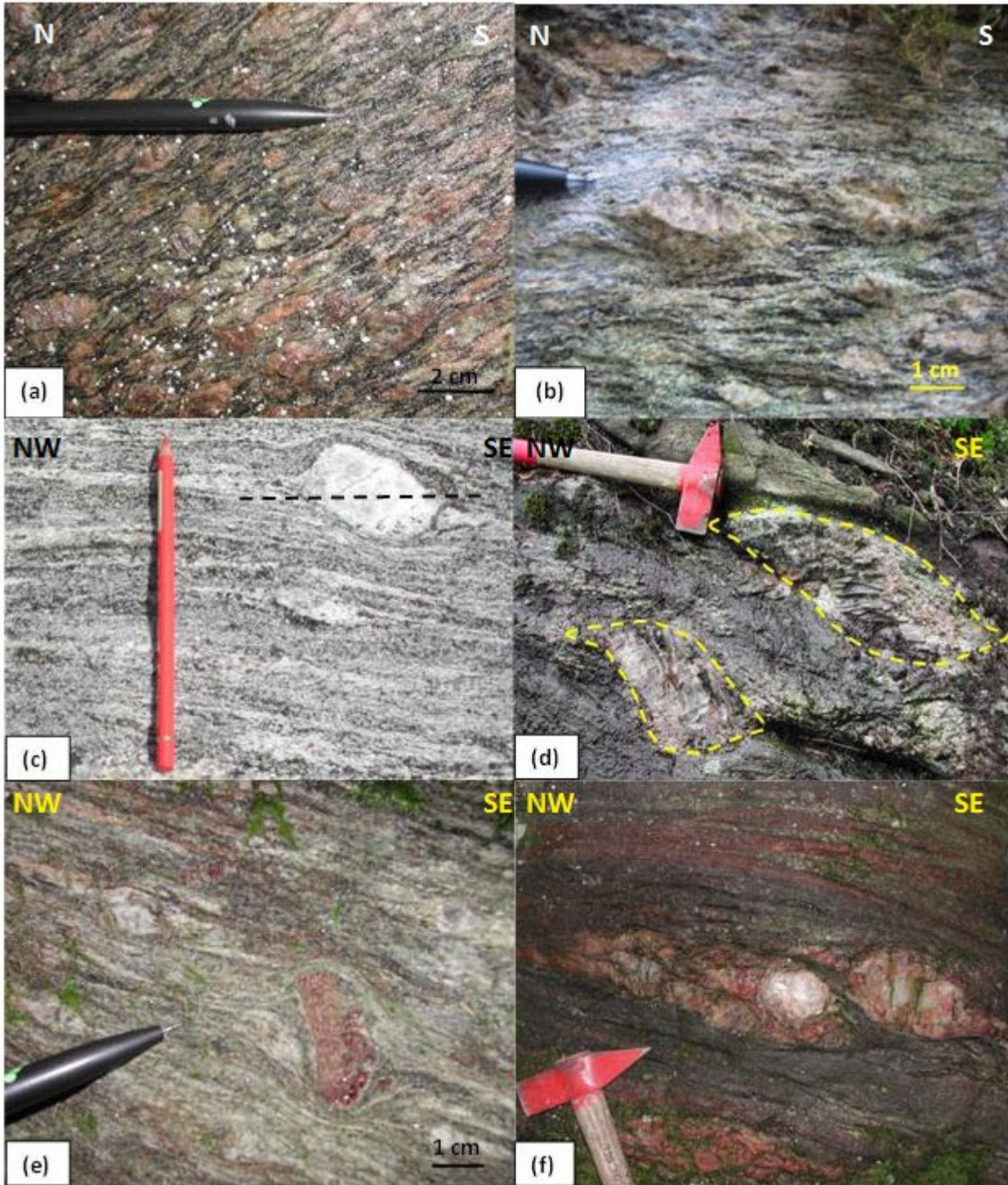
Fig. 27. (a) & (b) S-C-type fabric in a vertical NW-facing outcrop in the augen gneiss showing top-to-the-north relative movement, locality 44b (c) Sigma structure of plagioclase porphyroclast in a vertical SW-facing outcrop in the migmatitic grey gneiss showing top-to-the-NW relative movement, locality 41b. Pencil length is 17cm. (d) Sigma structure of quartz, K-feldspar and plagioclase aggregates in a vertical SW-facing outcrop in the grey orthogneiss showing top-to-the-NW relative movement, locality 91. The head of hammer length is 15 cm. (e) Tilted and rotated porphyroclast of garnet in a vertical SW-facing outcrop in the grey orthogneiss showing top-to-the-NW relative movement, locality 87. (f) Porphyroclasts of plagioclase and K-feldspar wrapped by the garnet-rich grey orthogneiss in a vertical SW-facing outcrop showing top-to-the-NW relative movement, locality 95. The head of hammer length is 15 cm.
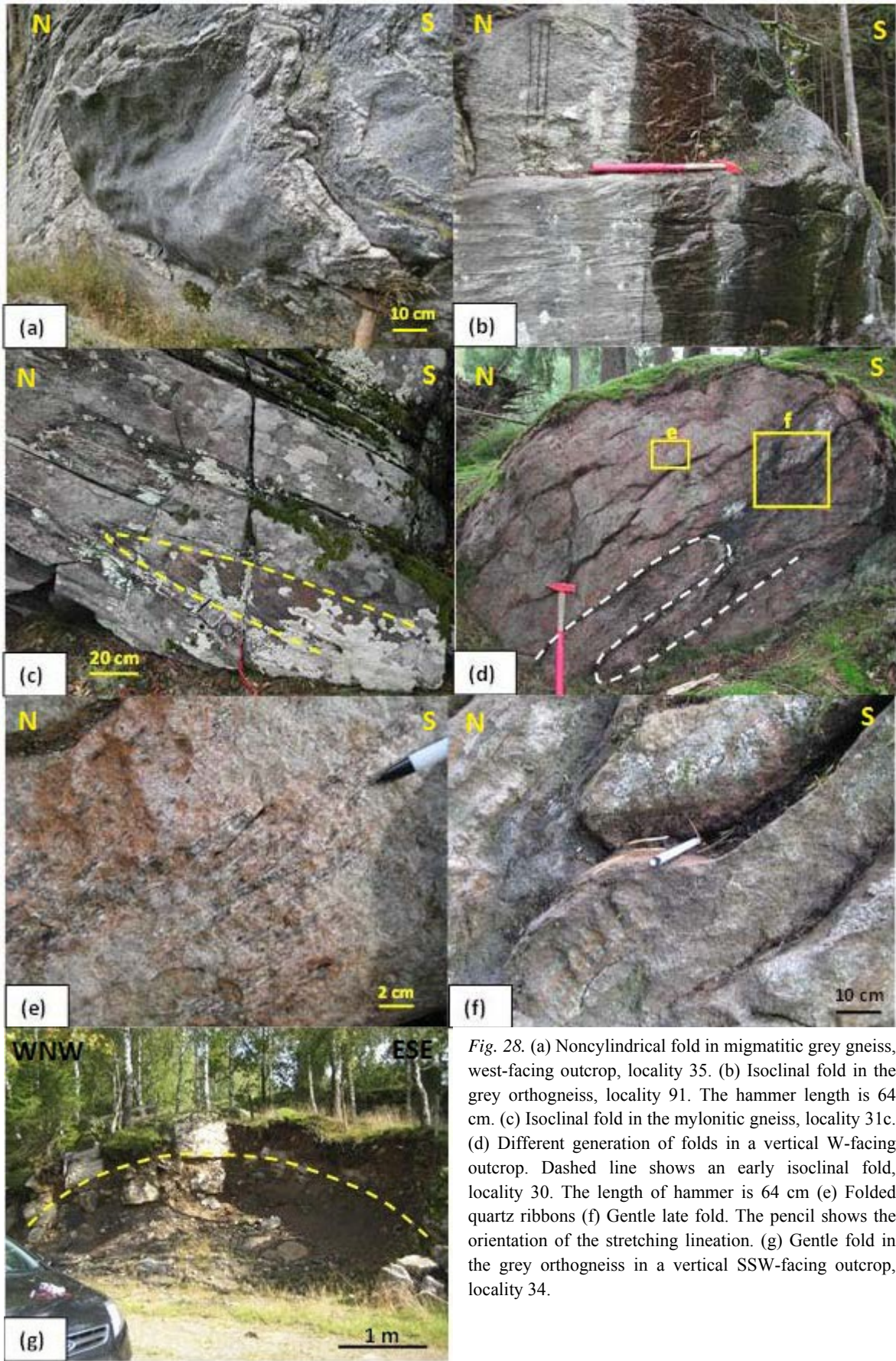
Fig. 28. (a) Noncylindrical fold in migmatitic grey gneiss, west-facing outcrop, locality 35. (b) Isoclinal fold in the grey orthogneiss, locality 91. The hammer length is 64 cm. (c) Isoclinal fold in the mylonitic gneiss, locality 31c. (d) Different generation of folds in a vertical W-facing outcrop. Dashed line shows an early isoclinal fold, locality 30. The length of hammer is 64 cm (e) Folded quartz ribbons (f) Gentle late fold. The pencil shows the orientation of the stretching lineation. (g) Gentle fold in the grey orthogneiss in a vertical SSW-facing outcrop, locality 34.

31
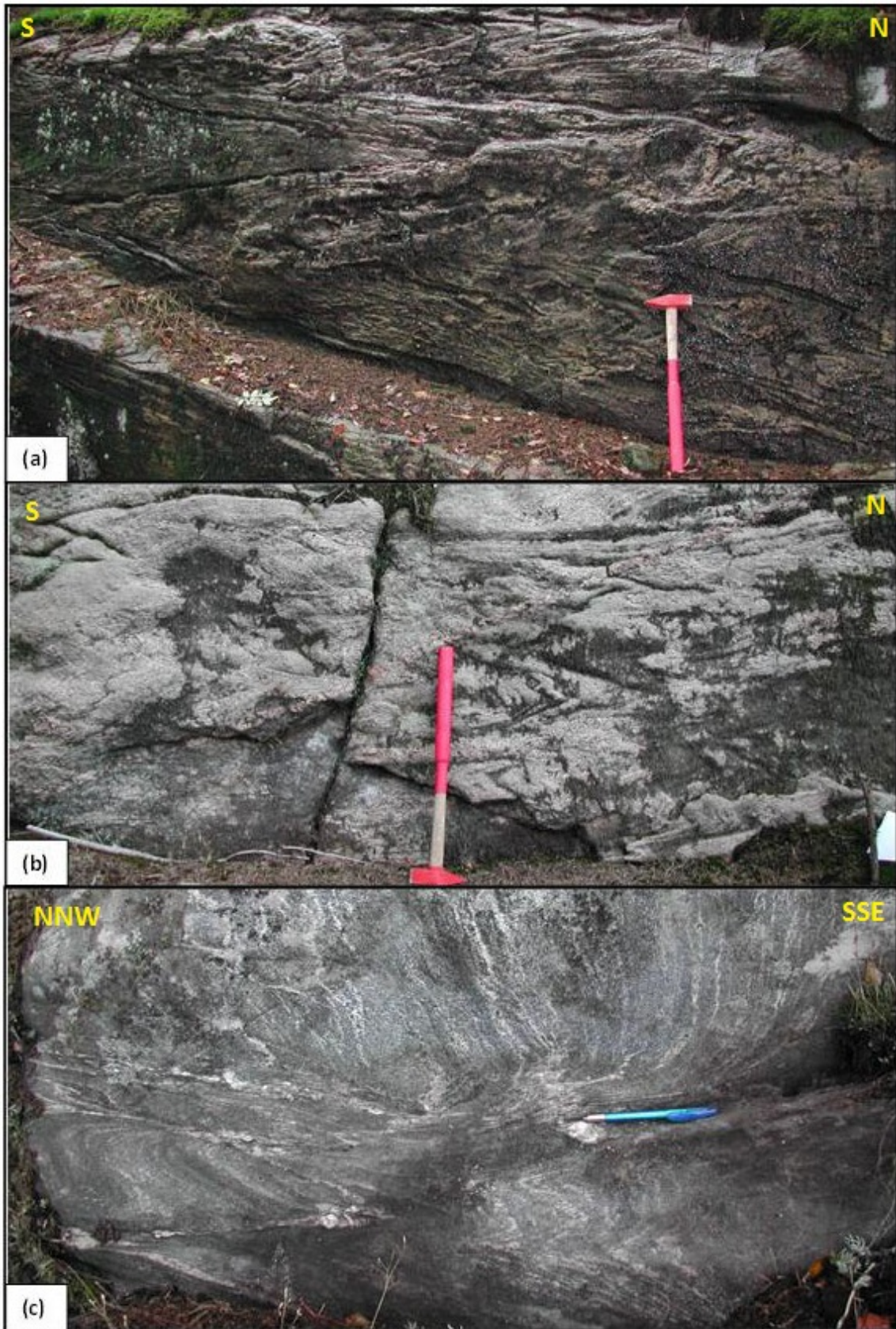
Fig. 29. Chevron folds developed in migmatite (a) A vertical E-facing outcrop in migmatitic grey gneiss with amphibolites lenses, locality 10. (b) A vertical E-facing outcrop in migmatitic grey gneiss, locality 16b. (c) A vertical WSW-facing outcrop in mylonitic gneiss showing shear plane associated with the development of a chevron fold, locality 18. The hammer and pen lengths are 64 cm and 16 cm, respectively.
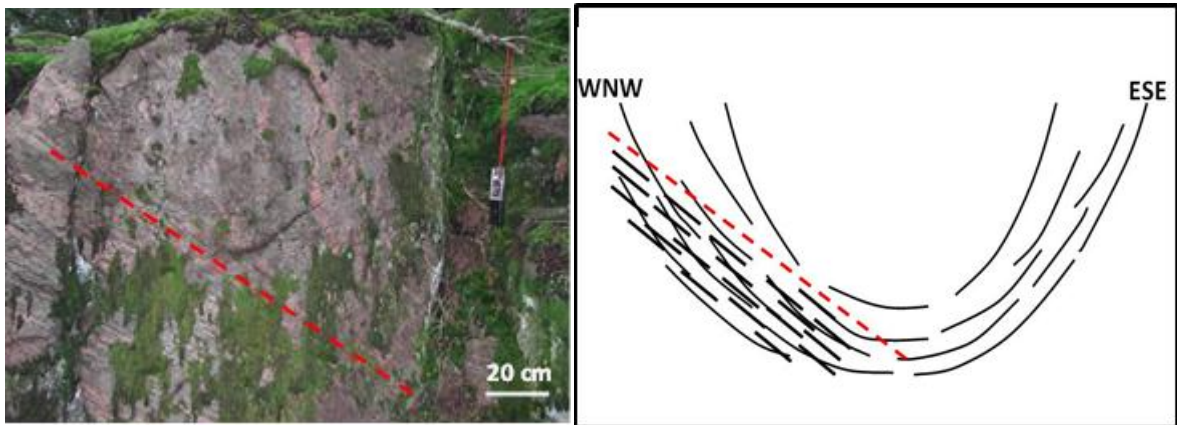
Fig. 30. The western limb of a gentle upright synform in a WNW-facing outcrop of Torpa type gneiss showing shearing in the lower part of the limb. The red dashed line represents the upper limit of the shear plane, locality 45b.
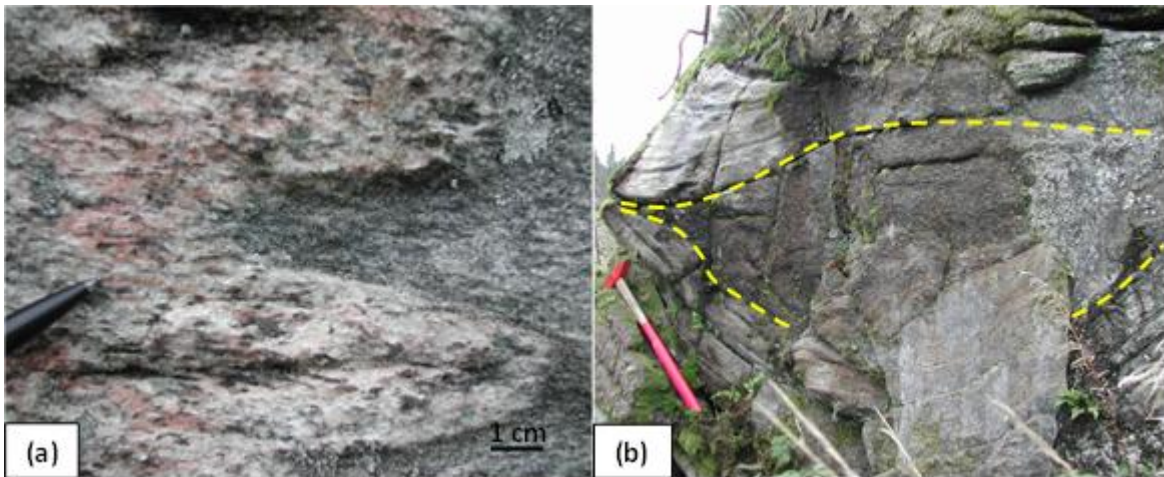
Fig. 31. (a) Elongated mineral aggregates (axial plane foliation) in a fold hinge in intermediate grey gneiss. The aggregates are composed of plagioclase, K-feldspar and quartz, locality 91. (b) Amphibolite lens in migmatitic body wrapped by grey gneiss, locality 90. Length of the hammer is 64 cm.
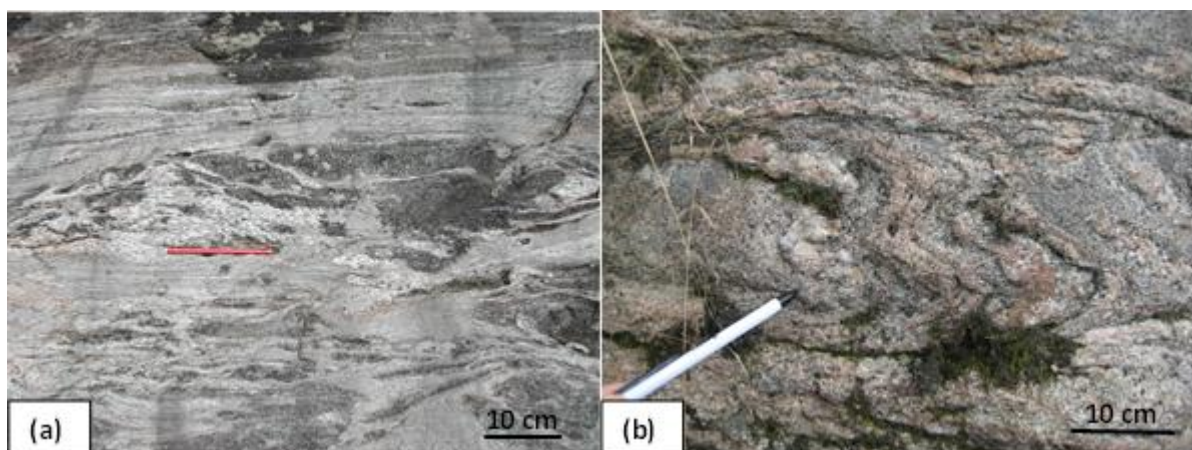
Fig. 32. (a) Stromatic migmatie with amphibolite lens in the grey orthogneiss, locality 41. (b) Folded migmatitic reddish grey orthogneiss, locality 16a.

A NNE-SSW trending upright synform (wave-length ca. 6 m) is defined by gneissic and migmatitic layering in Torpa gneiss (Fig. 30). A braided and heterogeneous gneissic foliation has developed in the lower part of the left limb in response to late stage shear.

In a WSW-facing sub-vertical outcrop in the mylonitic gneiss body, a shear plane was found with local top-to-the-SSE relative movement (Fig. 29c). The mesosome is dominated by amphibole while thin and white wavy-form folded ribbons of quartz and plagioclase constitute the leucosome. It appears that the chevron fold were formed in association with the shear plane development. But there is also a probability that the chevron fold was transected by a late phase of shear which displaced the foliations across the sub-horizontal plane.

5.6 Evidence of high strain

Field observation and thin sections demonstrate that the rocks were strongly strained under high-temperature conditions, corresponding to amphibolite, upper amphibolite and, locally, granulite facies. The Torpa type granite-gneiss, the migmatitic or-thogneisses and the mylonitic gneisses are strained with varying degrees. High strain is also evidenced by the presence of isoclinal and locally chevron folds especially in migmatitic gneiss and mylonitic gneiss. Furthermore, the occurrence of aggregate stretching lineations, particularly in the fold hinges (Figs. 28e & 31a), and tilted and rotated porphyroclasts (Fig. 27e) are small scale indicators of high strain.

5.7 Migmatization

Migmatization is common in the area, especially east of the heterogeneous mylonitic gneiss unit (Fig. 3). There the gneisses are stromatic migmatite with ca. 30-40% leucosome (Fig. 32a). Folded migmatitic structures are common particularly in the grey orthogneiss east of the heterogeneous mylonitic gneiss unit (Fig. 32b).

5.8 Grain size reduction

Grain size reduction occurred by recrystallization during high temperature. The effect of grain size reduction is shown by rigid porphyroclasts surrounded by a very fine recrystallized matrix (e.g. Figs. 19c-d & 26d).

6 Geochronology

6.1 Sample descriptions and results

Hornblende grains separated from nine hand specimens (localities are shown in Figure 24) were analyzed. The main purpose of Geochronology study was to date cooling time of hornblende through 500°C-550°C. Sample descriptions were given in more detail in chapter 4 where thin sections are explained. Most of the extracted hornblende minerals were fine-grained, 0.25 to 0.5 mm in size, but 0.5-1.0 mm fractions were also dated for a couple of the samples. Where the size of the fragments is not mentioned, the smaller size was considered. The isotopic results were presented in the appendix I and a series of spectrum graphs (Figs. 33-36) which represent step ages versus the cumulative % ^{39}Ar released. Rock sample descriptions and the results were also summarized in Table 2.

6.1.1 Reddish grey orthogneiss
6.1.1.1 Sample NMA11016a

The rock is sampled from a migmatitic reddish grey orthogneiss in the northeast of the area. The flat spectrum diagrams of over 80% of ^{39}Ar released, gave plateau ages of 919.9 ± 1.4 Ma and 923.2 ± 1 Ma obtained from 0.25-0.5 mm fractions and 926.7 ± 1.7 Ma and 925 ± 1.7 Ma obtained from 0.5-1.0 mm fragments (Fig. 33a-d).

6.1.1.2 Sample NMA11125

This sample is a grey orthogneiss characterized by intermediate composition which constitutes mesosome of the reddish grey orthogneiss. It is collected within a lithologic contact of the mylonitic gneiss. The spectra diagrams yielded ages of 927.6 ± 1.6 Ma and 928.4 ± 1.9 Ma, corresponding to about 50% of ^{39}Ar released (Fig. 33e-f).

6.1.2 Mylonitic gneiss
6.1.2.1 Sample NMA11018

The hand specimen was sampled within the mylonitic gneiss body about 5 m apart of a ~N-S shear plane in association with a chevron fold (Fig. 29c). The ^{40}Ar/^{39}Ar step-heating spectrum diagrams, corrosponding to 70-80% of the total ^{39}Ar released, yielded plateaus ages of 932.2 ± 1.6 Ma and 930.3 ± 1.4 Ma (Fig. 34a-b).

6.1.2.2 Sample NMA11019

The hornblende-bearing sample was taken from the mylonitic gneiss c. 100 m northeast of the sample NMA11018. The flat spectra diagrams manifesting around 80% of ^{39}Ar released, gave ages of 917.5 ± 1.7 Ma and 919 ± 2 Ma for the rock (Fig. 34c-d).
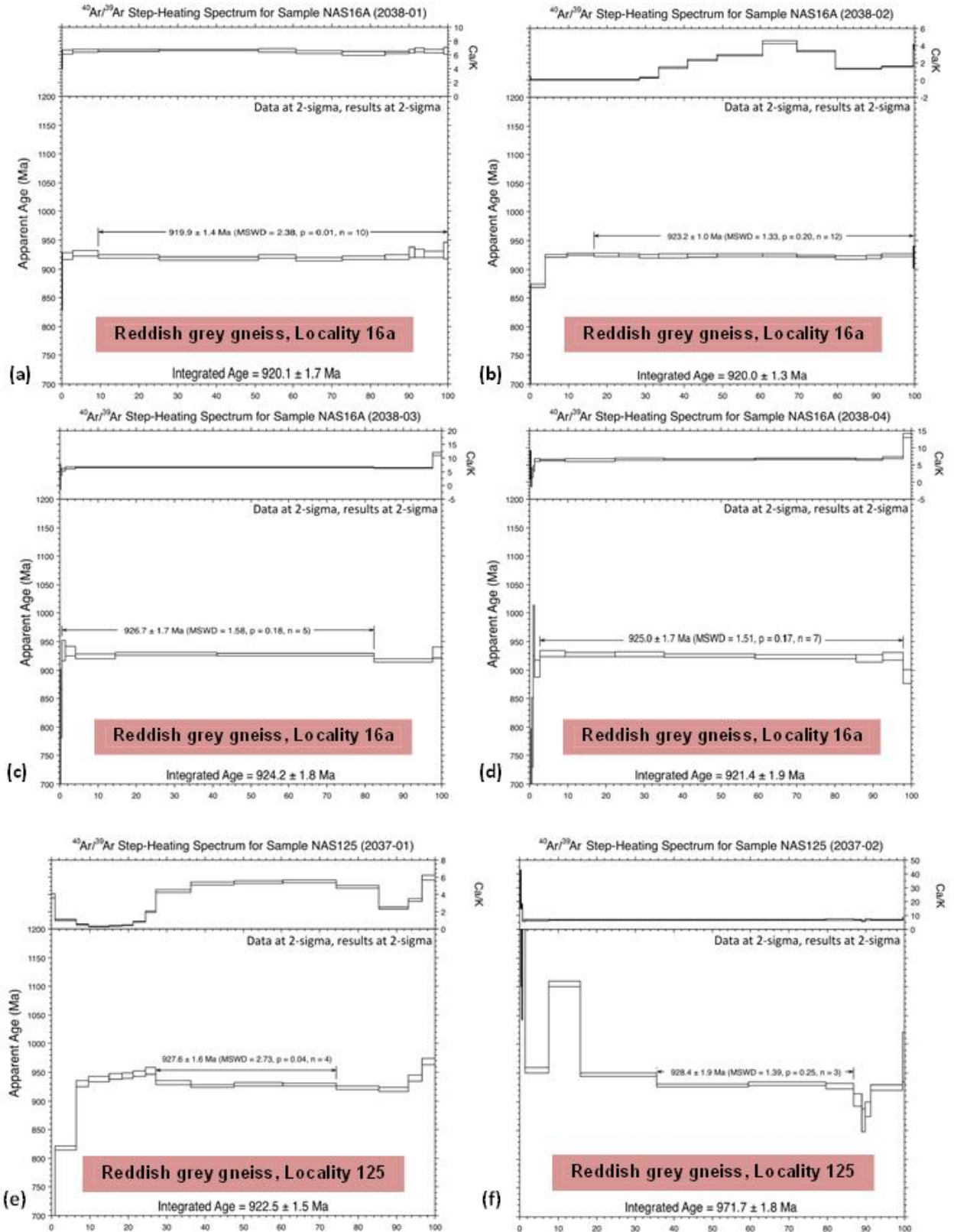
Fig. 33. $^{40}Ar/^{39}Ar$ release spectra of reddish grey orthogneiss. The color background in Fig. 33-36 corresponds to that of the rock units in the Geological map (Fig. 3).
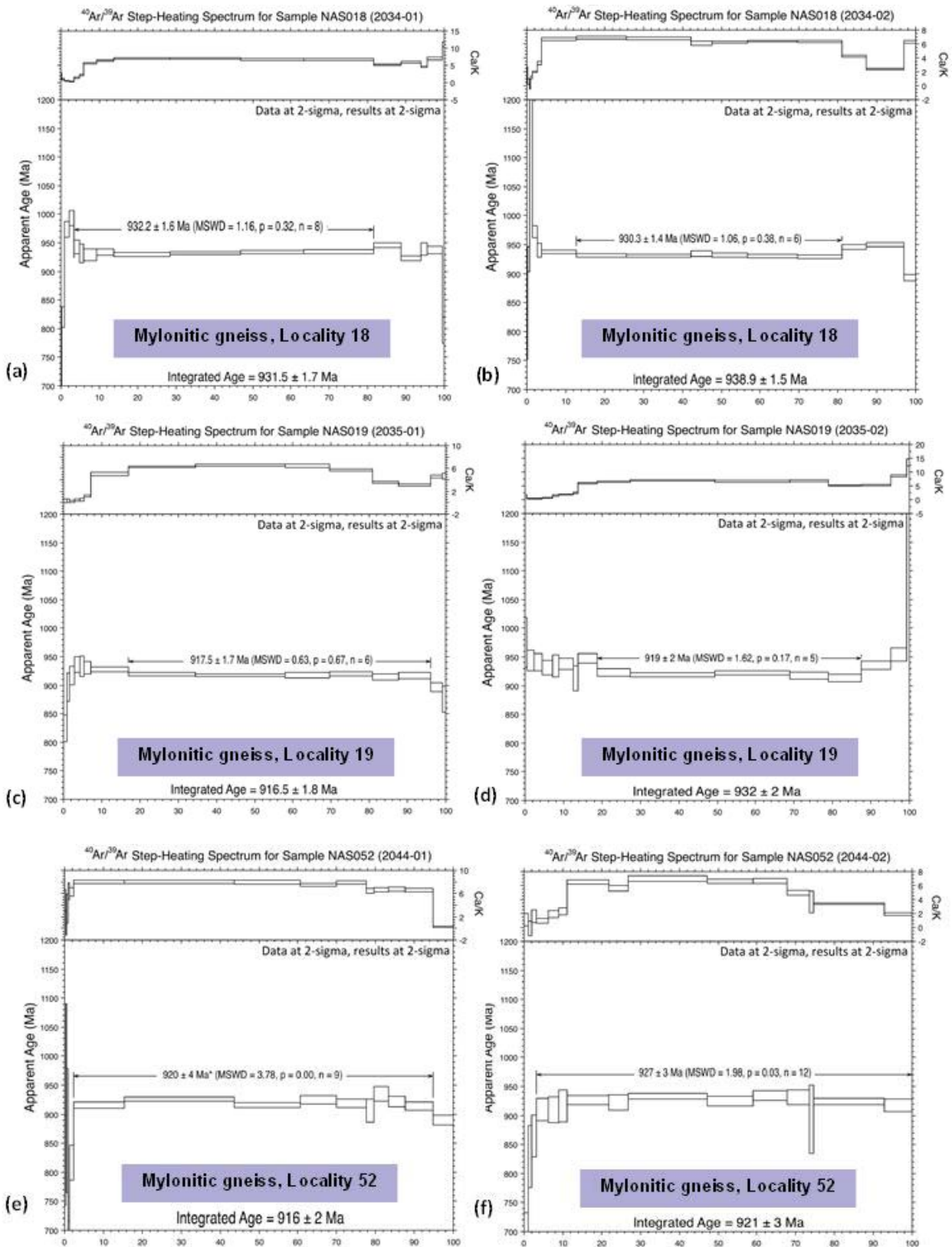
Fig. 34. ^{40}Ar/^{39}Ar release spectra of mylonitic gneiss.
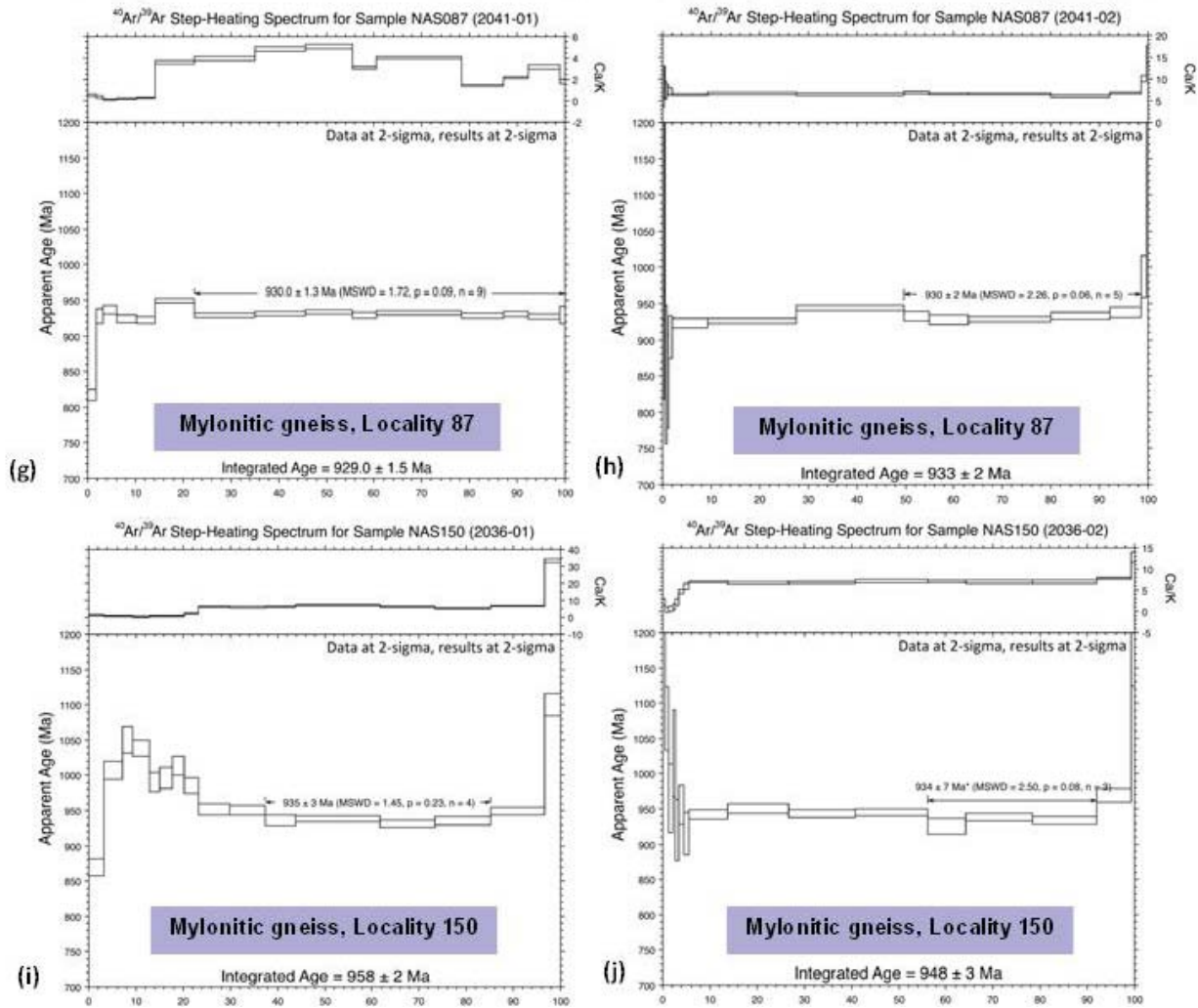
Fig. 34. $^{40}Ar/^{39}Ar$ release spectra of mylonitic gneiss (continued).

6.1.2.3 Sample NMA11052

The hornblende-bearing rock was sampled from the middle part of the mylonitic gneiss body yielded ages of 920 ± 4 Ma and 927 ± 3 Ma inferred from slightly irregular spectra diagrams showing more than 90% of released ^{39}Ar (Fig. 34e-f).

6.1.2.4 Sample NMA11087

This sample was collected from a small mylonitic gneiss body in contact with the Torpa granite at its southern end. Ages of 930 ± 1.3 Ma and 930 ± 2 Ma were achieved from the spectra plateaus (Fig. 34g-h). 50-70% of ^{39}Ar was released during the heating steps.

6.1.2.5 Sample NMA11150

The rock was sampled from the mylonitic gneiss in contact with the grey orthogneiss in the most southern part of the area. The roughly erratic spectra plateaus gave ages of 935 ± 3 Ma and 934 ± 7 Ma, corrosponding to less than 50% released ^{39}Ar (Fig. 34i-j).

6.1.3 Strongly deformed augen gneiss

6.1.3.1 Sample NMA11001

The hornblende-bearing sample corresponds to the strongly deformed augen in the margin of the Torpa granite massif. No plateau ages yielded from one of the graphs representing very erratic spectra, while the other graph gave age of 926 ± 1.6 Ma showing about 40% released gas (Fig. 35a-b).

6.1.4 Retro-eclogite

6.1.4.1 Sample NMA11029

The sample was taken from a 30 m² retroeclogite body associated with the heterogenous mylonitic gneiss. The plateau ages yielded from the $^{40}Ar/^{39}Ar$ step-heating spectrum (fractions of 0.5-1.0 mm in size) is 957.8 ± 1.3 Ma (Fig. 36b), while ages of 954.7 ± 1.6 Ma and 953.3 ± 1.5 Ma were achieved from the smaller fractions (Fig. 36c-d). 80-100% of ^{39}Ar was released during the heating steps. One of the step-heating graphs representing no plateau age was ignored (Fig. 36a).
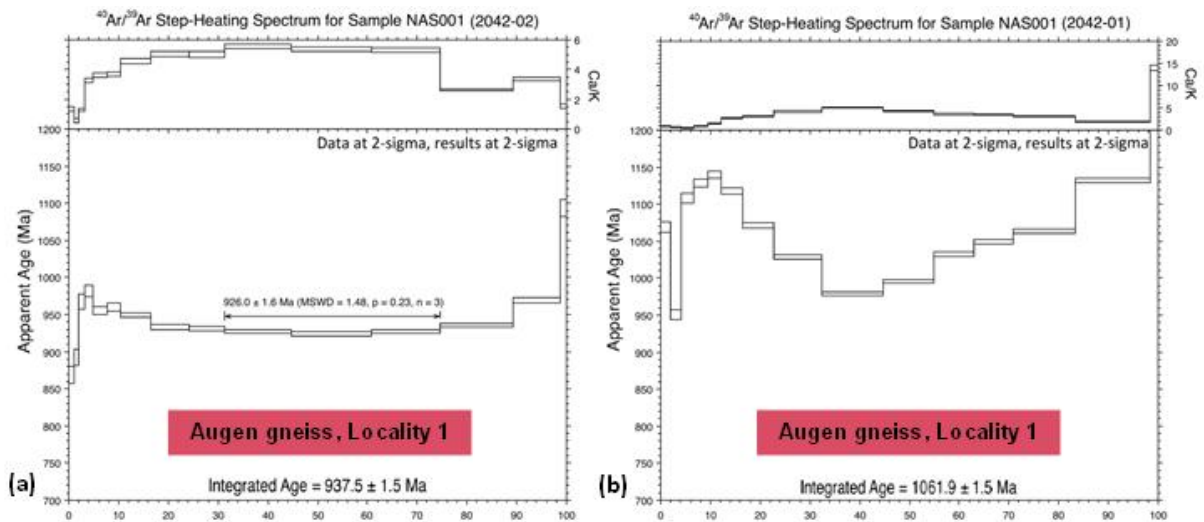
Fig. 35. ^{40}Ar/^{39}Ar release spectra of augen gneiss
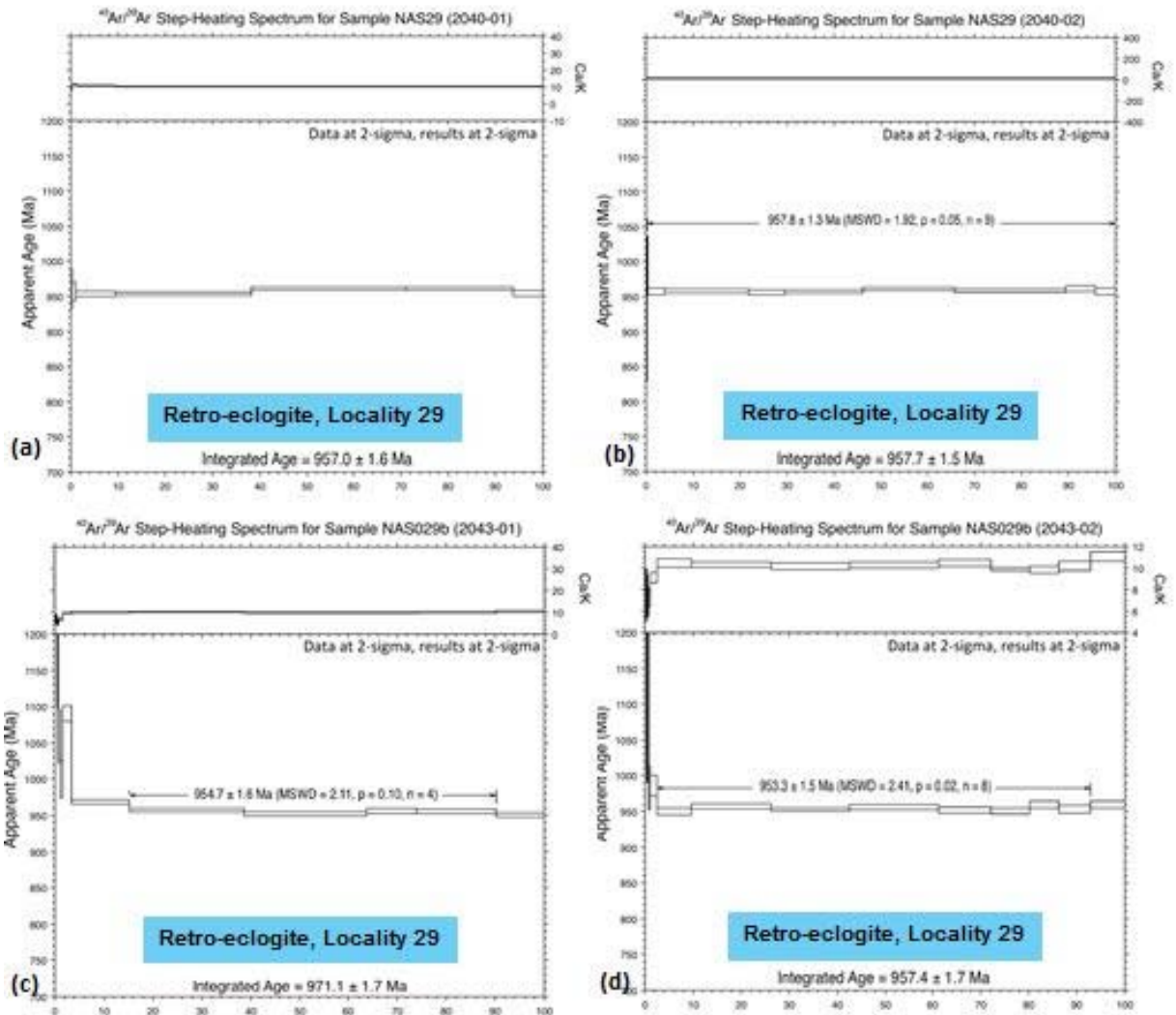
Fig. 36. ^{40}Ar/^{39}Ar release spectra of retro-eclogite.

Table. 2. Analyzed hornblende samples for $^{40}Ar/^{39}Ar$ dating. The ages were rounded for simplicity. The color background in Figs. 33-36 corresponds to that of the rock units in the map (Fig. 3).

Location Nr.	Rock type	Fraction size (mm)	Grain size of Hbl (mm)	Age ± 2σ	Released Ar %	Remark
16a	Reddish grey orthogneiss	0.25-0.5	0.1-3	920 ± 1	90.4	
				923 ± 1	83.2	
		0.5-1.0	0.1-1.5	927 ± 2	81.9	
				925 ± 2	95.3	
125	Reddish grey orthogneiss	0.25-0.5	0.1-2	928 ± 2	47.1	
				929 ± 2	51.2	
18	Mylonitic gneiss	0.25-0.5	0.01-0.3 Porphyroclast < 2.5	932 ± 2	78.2	
				930 ± 1	68.2	
19	Mylonitic gneiss	0.25-0.5	0.01-0.2 Remnant < 1.5	918 ± 2	79	Hbl-bio aggregates
				919 ± 2	68.7	
52a	Mylonitic gneiss	0.25-0.5	0.1-1	920 ± 4	92.4	
				927 ± 3	96.6	
87	Mylonitic gneiss	0.25-0.5	0.01-0.2 Porphyroclast < 2.5	930 ± 1	77.6	
				930 ± 2	49	
150	Mylonitic gneiss	0.25-0.5	0.01-0.5	935 ± 3	47.8	
				934 ± 7	35.8	
1	Augen gneiss	0.5-1.0	0.5-3	926 ± 2	43.3	Hbl-bio aggregates
29	Retroeclogite	0.5-1.0	0.5-2	958 ± 1	99.7	
		0.25-0.5		955 ± 2	74.9	
			0.5-2	953 ± 1	90.5	

7   Interpretations

7.1   Metamorphism

7.1.1   Metamorphic assemblages

The mineral assemblages and textures described in previous sections allow identification of the following metamorphic assemblages:

7.1.1.1   Eclogite facies

Presence of remnant clinopyroxene with expelled plagioclase (former omphacite; Möller 1998, 1999) and garnet reveals a previous eclogite facies assemblage in the retroeclogite. Kyanite in hand specimens and sapphirine symplectite after kyanite in the thin section also confirm the occurrence of eclogite facies. High pressures result in the breakdown of plagioclase and formation of sodic clinopyroxene. Matrix plagioclase is a secondary phase formed during decompression.

7.1.1.2   High-pressure granulite to amphibolite facies

Some samples (mylonitic gneisses and garnet-amphibolite) were recrystallized under granulite facies conditions. The mylonitic gneisses formed mineral assemblages consisting of clinopyroxene, garnet, plagioclase, biotite, hornblende, scapolite and quartz. Garnet and clinopyroxene are however generally absent in the felsic rocks. The garnet-amphibolite also has mineral assemblages composed of garnet, hornblende, plagioclase, clinopyroxene and quartz.

7.1.1.3 Amphibolite facies

The occurrence of amphibolite facies is often found with migmatization of the grey and reddish grey orthogneiss by the presence of hornblende and plagioclase with lesser amounts of quartz and biotite and also accessory chlorite and epidote in the mineral assemblage.

7.1.1.4 Greenschist facies

Greenschist facies minerals likely formed as local alteration of the higher grade mineral assemblages during later erosion at low pressures and temperatures. Saussuritization is prevalent but not pervasive, giving the plagioclase grains a dusty appearance in all the rock types. The chloritization of biotite along with epidotization is also common. The presence of allanite -epidote group- is also indicative of low-grade fluid presence.

7.1.2 Evidences of high strain in microscale

The formation of myrmekite in the grey orthogneiss is associated with migmatization under amphibolite facies conditions and recrystallization of the felsic domains. Myrmekite is a secondary texture of quartz intergrowth in plagioclase which forms under a high tectonic strain typically in granites and metamorphic gneisses with a composition similar to granite. SiO_2 releases while plagioclase replaces the K-feldspar and vermicular quartz is produced (Winter 2010). High strain has also resulted in orthoclase to microcline recrystallization in the augen gneiss, which significantly increase in the Torpa-type granitic gneiss as a cosequence of strain (cp. Fig. 8c-f with 11a-b). In addition perthite was also produced from the exsolution of plagioclase in K-feldspar in response to high strain in the augen gneiss. High strain also created strongly elongated mineral and/or mineral aggregates in particular, quartz.

7.1.3 Partial melting

The stromatic migmatitic gneiss is characterized by coarse-grained felsic leucosomes parallel to the gneissic foliation reflecting a strong deformation phase. Leucosome containing plagioclase, K-feldspar and quartz devoid of anhydrous minerals indicate the presence of water-saturated melting (Vernon and Clark 2008). The higher degree of migmatization and partial melting in the easternmost investigated area (Fig. 3), may imply the presence of more water at the time of metamorphism, than the other parts. There is also a probability that the eastern part was closer to the source of heat responsible for migmatization.

7.1.4 Exhumation and uplift

Evidences of retrograde metamorphism are reflected in amphibolitization of granulite and eclogite facies assemblages. The textural features of high-pressure assemblage like remnants of clinopyroxene and garnet are not in equilibrium with the lower-pressure assemblage of hornblende and biotite. Clinopyroxene remnants are present in retroeclogite, garnet-amphibolite and mylonitic gneiss. They are intergrown with expelled plagioclase, which reveal decompression and re-equilibration stage of metamorphism. Clinopyroxene was also partially replaced in several samples by secondary hornblende crystals. Breakdown of garnet producing fine plagioclase, hornblende and biotite and also the corona texture of plagioclase around garnet indicate that metamorphism has taken place through retrogression stage. Calcium required for plagioclase production is provided by releasing Ca^{2+} ions in the breakdown of grossular. Replacement of kyanite as a high-pressure mineral by symplectite of sapphirine also verifies metamorphism under granulite facies (Ackermand et al. 1975, Möller 1998, 1999) which later continued through upper amphibolite facies. Scapolite grains were also produced under granulite facies in high temperature conditions which are brought upwards during exhumation. Moecher and Essene (1991) assert that scapolite production takes place in the lower crust conditions where CO_2- and sulfate-rich fluids are available. Goldsmith and Newton (1977), also state the necessity of the lower crust conditions for the occurrence of scapolite and consider it as high temperature mineral.

7.2 Structure

7.2.1 Heterogenous deformation

Heterogenous deformation is characterized in the study area by several indicators which are:

- Difference in competency (e.g. competent Torpa granite versus the mylonitic gneiss)
- Wrapped porphyroclasts of garnet and feldspars in orthogneisses (e.g. Fig. 27f).
- Abundance of amphibolite lenses in the migmatitic units wrapped by orthogneiss (Fig. 31b).

7.2.2 Strain

A prominent NNW-SSE- trending foliation is evident in the area, along with a minor ESE-WNW- trending foliation. According to the map (Fig. 22), the gneissic foliations, locally, show bending structures which would imply that both trends of the foliations belong to the same generation but underwent a subsequent folding phase. A larger overview of the area in the airborne magnetic map also illustrates a bending form of similar trending foliation in a scale of tens of kilometers (Fig. 37). At least four bending sub-parallel structures are distinguishable, which get close to one another in the northwest, near the Mylonite Zone (Fig. 37). This would imply that geological structures are fractal in nature, thus, the outcrop scale structures represent the regional scale structures and what you see in

regional scale is also reflected in meso- and micro-scale. However, no systematic fold axis pattern can be deduced from foliations to verify that all foliation were generated by the same strain regime. The most out-standing curving structure is visible around the Torpa granite (Fig. 22), similar to the foliations mapped by Ekdahl (2001) in the northwest of the study area. This gneissic foliation is more due to the highly competent granite body than to a later fold phase.

Since only a couple of the kinematic indicators were observed parallel to the mineral stretching linea-tions, a certain sense of shear is not easy to determine. Top-to-the-ESE sense of shear were observed parallel to the E-plunging mineral stretching lineations similar to Ekdahl (2001) and Dyck (2011) observations in the northwest and farther southeast of the area. Relative movements of the clasts, however, reveal two opposed movement direction (Fig. 24). The possibility that the-se movements are resulted from two different strain phases is not easy to realize.

There are two possible scenarios that can explain deformational history of the area. In the first scenario, ESE-WNW foliation is older than NNW-SSE-trending foliation. Although these two foliation sets are not observed to intersect, several features manifest that the former is deflected by NNW-SSE structures. In three outcrops, late and coarse-grained granitic melts crystallized along sub-horizontal (locality 2) and gently north-dipping (locality 40b) ~

N-S shear planes (Figs. 25). An assumption is, an E-W extension component was occurred resulted in the development of upright and symmetric ESE-WNW generation of folds simultaneously with the onset of regional migmatization. The area must be later, influenced by an intense shear phase which consequently formed E-plunging intrafolial isoclinal folds and parallel mineral stretching lineation. A second NNW-SSE phase of shear displaced the ESE-WNW foliation along the sub-horizontal or moderately north-dipping shear planes (Figs. 25 & 29c).

The second scenario is that following the onset of regional migmatization, E-plunging mineral stretching lineations were formed simultaneously with ~N-S shearing, resulted in the progression of isoclinal folds. The trends of mineral stretching lineation and shear direction are assumed to be parallel in high strain shear zones (Passchier and Trouw 1996). Nevertheless, these two are not necessarily exactly parallel to one another, but lineation is associated with the finite strain and cannot be parallel to motion especially when a non-axial deformation is present (Lin et al. 2007; Ridley 1986; Burg, 1999), similar to our study area in which shear sense indicators are not parallel to the E-plunging mineral stretching lineations. In this scenario, deflection of pre-existing ESE-WNW foliation (Fig. 25, 29c) is assumed synchronized by isoclinal folds formation and the related shear phase.
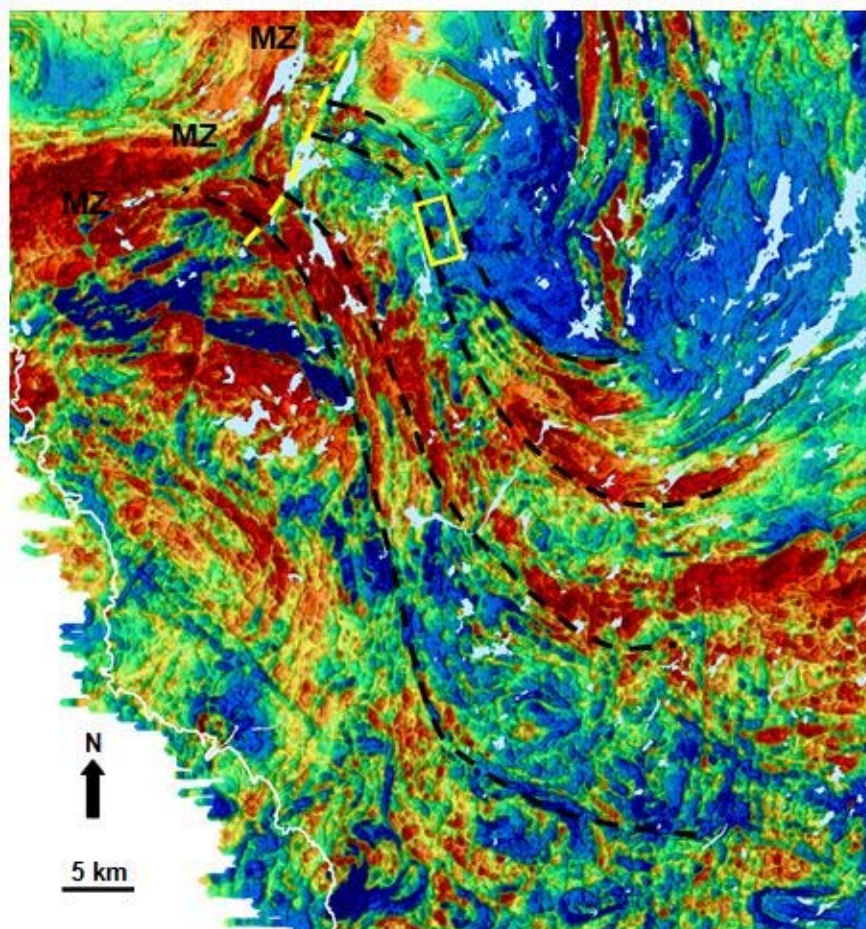
Fig. 37. Airborne magnetic map of the Varberg - Ullared area (source SGU), illustrating bending structure (denoted by dashed lines) in the regional scale. The yellow dashed line represent a major fault. The yellow rectangular shows the study area. MZ = Mylonite Zone.
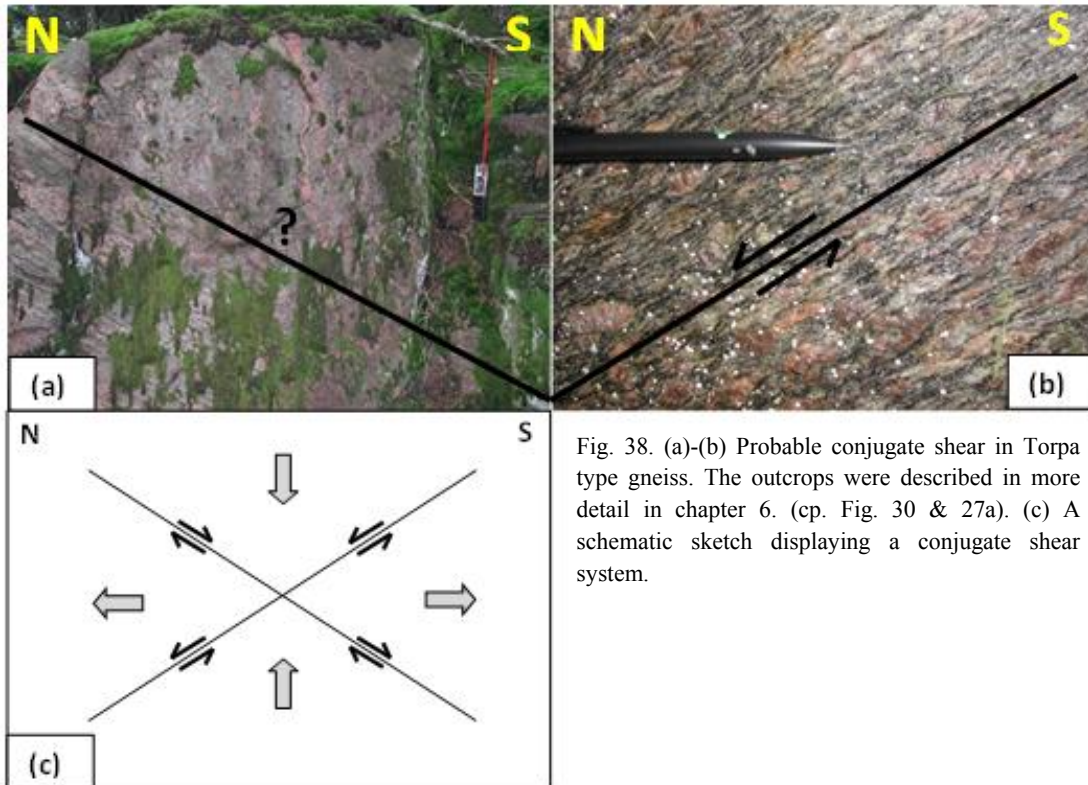
Fig. 38. (a)-(b) Probable conjugate shear in Torpa type gneiss. The outcrops were described in more detail in chapter 6. (cp. Fig. 30 & 27a). (c) A schematic sketch displaying a conjugate shear system.

Irrespective of which scenario is correct, one late phase of shear must have taken place. Open and upright NNE-SSW- trending fold in the Torpa-type gneiss (Fig. 30) which is younger than isoclinal generation of folds (Ekdahl 2001, Möller et al. 2007, Tual et al. 2012) has a sheared limb. The late shear phase is parallel to the NNW-SSE structures of the Svarten Zone. There is also a possibility that the open fold is affected by conjugate shear. In spite of the absence of an exposure displaying conjugate shear zone, two parallel outcrops in Torpa type gneiss-augen gneiss, c. 50 m apart, show shear planes dipping ~ 35° in opposite directions (Fig. 38). S-C fabric indicates a top-to-the-north sense of shear in the southern outcrop (Fig. 38b). An occurrence of a conjugate shear system, thus, would be probable providing that the northern outcrop (Fig. 38a) has a top-to-the-south sense of shear, but there is no evidence to support it. It can be a young deformation developed by ~ N-S and ~ E-W extensions and a vertical compression component (Fig. 38c).

7.3 Geochronology

7.3.1 Principles of the $^{40}Ar/^{39}Ar$ dating method

Potassium is one of the most abundant elements in the crust occurring in three isotopes. All the K-bearing minerals contain a portion of ^{40}K isotope which decays to ^{40}Ar with a half life of 1.25 Ga (McDougall and Harrison 1999). Ar atoms generated as a consequence of radiogenic decay immediately escape from the mineral structure at high temperatures. Once the tempera-ture falls below the closure temperature, the mineral begins to accumulate Ar. $^{40}Ar/^{39}Ar$ geochronology method, hence, does not yield time of a mineral pro-duction, but the time elapsed since the mineral reaches to its closure temperature (Faure 1986) and start to preserve ^{40}Ar.

7.3.2 Excess Ar

"Excess Ar" is that portion of ^{40}Ar except of atmos-pheric ^{40}Ar which incorporates into a K-bearing miner-al by any process other than in situ radioactive decay of ^{40}K (McDougall and Harrison 1999). An assump-tion in $^{40}Ar/^{39}Ar$ dating method is the absence of any non-atmospheric ^{40}Ar in a given mineral while the system is still open (Dodson 1973). A pre-existing component of ^{40}Ar will cause the obtained age to be too old. A necessity for "zero radiogenic Ar assump-tion" defined by Baxter et al. (2002) is an immediate emission of radiogenic ^{40}Ar from a given mineral and its nearby surrounding before the temperature drops to the mineral closure temperature.

Baxter (2003) presented a model to illustrate potential internal and external sinks for ^{40}Ar (Fig. 39). The product Ar may diffuse out of the K-bearing mineral (or even return back into the source mineral) and into the local intergranular transporting medium (ITM). ITM can be a wet or dry networks of grain boundaries. Matrix mineral, grain boundaries and fluid phases are essential factors in terms of providing a local sink to accumulate some portions of the ^{40}Ar which may back to the mineral composition (Fig. 39). Accordingly, any rock unit owning high volume of

local sink contains fairly little excess Ar in the mineral of interest. The efficiency of local sinks depends on their diffusive closure characterizations, Ar partition coefficients and relative modes. Quartz is an efficient sink of Ar in the K-bearing rocks due to its strong partitioning (Baxter et al. 2002; Baxter 2003). Consequently, more felsic rocks are expected to have less excess Ar in their K-bearing minerals.

Furthermore, the amounts of excess Ar will be lower when the produced Ar more quickly escape from the mineral to an external sink (e.g. Atmosphere) (Baxter 2002; Baxter et al. 2003). Fluids have an essential role in terms of acceleration of Ar diffusion. The high incompatibility behavior of Ar allows it to escape from the source mineral into grain boundary fluids in metamorphic rocks, which accordingly makes the fluids an effective reservoir for Ar (Kelley 2002).

Conversely, the transmission of Ar in a fluid-poor system is only a few centimeters over millions of years, which is not an ideal system to diffuse Ar out of the source mineral (Scaillet 1996). Baxter et al. (2002) also state that ITM cannot be efficient if it constitute a tiny fraction of the rock. According to Kelley (2002), the grain boundary fluid phase in dry systems such as eclogites and granulites may be as little as a layer of OH- molecules at the grain boundaries. Scaillet (1996) also asserts that an excess Ar component will remain in the source mineral from the initial closure temperature of the former high-pressure conditions.

7.3.3 Hornblende cooling age in Källsjö

In this study, hornblende grains were dated in order to obtain cooling age through 500°C (Dahl 1996) -550°C (Harrisson 1981) associated with the unroofing history and exhumation of eclogite-bearing section of the Ullared Deformation Zone. The obtained plateau ages range from 935 Ma to 917 Ma (Fig. 33-35) with the exception of retro-eclogite spectra giving the ages of about 953-958 Ma (Fig. 36).

Sample 16a, a **reddish grey orthogneiss**, with hornblende fractions of 0.25-0.5 mm in size, yielded plateau ages of 919.9 ± 1.4 Ma to 923.2 ± 1 Ma. The coarser fractions of hornblende resulted in, however, slightly older ages of 926.7 ± 1.7 Ma and 925 ± 1.7 Ma. This difference could reflect a difference in cooling age with the grain size. All the related diagrams represent flat spectra, corresponding to a sufficient amounts of ^{39}Ar released (82-95%). Hornblende grains were well-separated with no contamination with the other minerals. According to the above mentioned factors (Sec. 7.3.2), the obtained ages (920-927 Ma) from sample 16a would be the most convincing plateau ages, in terms of consisting high amount of quartz and also benefiting from recrystallization under fluid-rich system of amphibolite with no evidence of high-pressure metamorphism. Hornblende minerals in the sample 125, also were recrystallized in a condition similar to the sample 16a gave convincing ages of 927.6 ± 1.6 Ma and 928.4 ± 1.9 Ma, which are, however, based on about 50% released Ar.

Hornblende fractions belong to the **mylonitic gneiss** were all fine-grained (0.25-0.5 mm) and yielded plateau ages range between c. 917 Ma and 935 Ma. Sample 18 gave ages of 932.2 ± 1.6 Ma and 930.3 ± 1.4 Ma, corresponding to 68-78 % of Ar released. The slightly older ages in comparison with the most convincing ages (sample 16a), might be due to less amount of quartz to act as a local sink in the rock (Fig. 13). Sample 19 containing of hornblende occurring as aggregates with biotite, yielded ages of 917.5 ± 1.7 Ma and 919 ± 2 Ma. The presence of biotite along with separated hornblende could cause to obtain young age of 917 Ma (cp. thin sections, Fig. 14a-b) due to the difference in closure temperature of biotite (c. 300°C) (Harrison et al. 1985) compared to 500°C-550°C for hornblende. Ages of 920 ± 4 Ma and 927 ± 3 Ma were also achieved from sample 52a. Although the hornblende fractions suffered from poor separation in terms
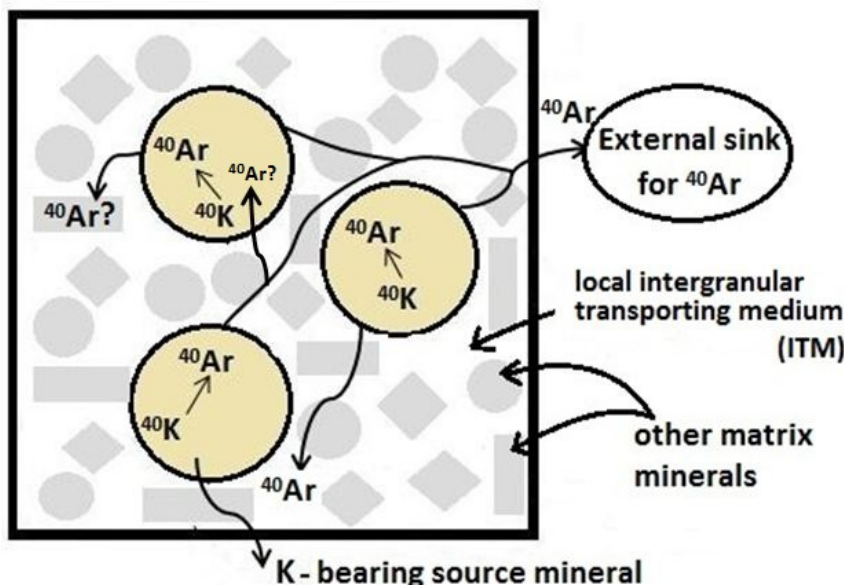
Fig. 39. Schematic model of potential sinks for ^{40}Ar. K-bearing source mineral in association with the internal (e.g. matrix minerals and intergranular transporting medium) and external sinks (modified after Baxter 2003).

of occurring with the other minerals, the ages are interpreted as convincing cooling age in order to be a felsic rock recrystallized under a fluid-rich metamorphic facies with no sign of high-pressure metamorphism. Sample 87 gave the plateau age of about 930 Ma to 932 Ma. According to the thin section (Fig. 16), evidences of the initial crystallization under poor-fluid system of granulite facies is distinguishable, which could accumulation of excess Ar in hornblende. Ages of 934-935 Ma were obtained from Sample 150, based on less than 50% of released ^{39}Ar. In addition, according to the thin section (Fig. 17), the rock has undergone crystallization under high pressure granulite facies, with restricted amounts of fluid. These older ages are interpreted as containing some excess Ar.

The **deformed augen gneiss** gave a plateau age of 926 ± 1.6 Ma similar to the mylonitic gneiss (sample 52a) and the grey orthogneiss (samples 16a & 125). But the obtained age would, nevertheless, not consider reliable, because of the inadequate amount of released gas, together with contamination of hornblende fractions with the other minerals.

Hornblende fractions of the **retroeclogite** sample (0.5-1 mm) gave plateau ages of 957.8 ± 1.3 Ma while the smaller fractions (0.25-0.5 mm) yielded ages of 954.7 ± 1.6 Ma and 953.3 ± 1.5 Ma. The relatively coarse size of the hornblende grains in comparison with the other rock types can not readily justify a difference in the age of c. 30 Ma. The rock has initially formed under fluid-poor system of eclogite facies characterized by a low ability to transmit the produced Ar out of the source mineral. These old ages are interpreted as remained excess Ar in hornblende grains from the initial closure temperature of eclogite facies. Moreover, the mafic retro-eclogite with small amounts of quartz does not contain a capable sink for excess Ar.

7.3.4   Cooling rate

The occurrence of partial melting in the migmatite gneiss (Skene, farther north), based on metamorphic zircon, has been dated at 969 ± 13 Ma (Andersson et al. 2002). Considering the convincing ages range between 920 Ma and 927 Ma for hornblende cooling age in the investigated area, together with the maximum temperature of 770°C as a peak metamorphism in the Ullared region (Johansson et al. 1991), cooling rates of 5.5-6.4 °C/m.y. were achieved for hornblende down to the 500°C, and 4.5-5.2°C/m.y. down to the 550°C which reflect cooling following peak metamorphism through the Sveconorwegian Orogen uplift.

8 Suggestions for follow-up study

- Geochronology study of the granitic melt crystallized in the shear planes to find out the relative age of N-S shear phase.
- Similar studies in the sub-parallel structures towards west.
- Focus on NNE- trending upright open folds in a more widespread area to find out its relation and relative timing in comparison with the other structural features.

9   Conclusions

Based on petrography, structures and geochronoly studies and above given results, the conclusions can be inferred:

- The sheared limb of NNE-trending young upright, open generation of folds infer that a late phase of shear has taken place probably in association with ~N-S Svarten Zone structures.
- Two retoeclogite units were found, within the mylonitic gneiss, more than 2.5 km apart.
- Hetereogenous deformation is one of the most common characteristic throughout the area.
- Mineral assemblages indicate retrogression metamorphism reflected in superimposed amphibolite mineral assemblages on eclogite and granulite facies mineral assemblages simultaneous with the uplift of the Sveconorwegian Orogen.
- ^{40}Ar/^{39}Ar dating of hornblende yielded cooling ages between 920 Ma and 927 Ma.
- The cooling rate of 5.5-6.4 °C/m.y. and 4.5-5.2 °C/m.y. were obtained from the onset of partial melting and migmatization down to the hornblende cooling age of 920 Ma to 927 Ma, respectively, upon the determined closure temperatures, associated with uplift of the Sveconorwegian Orogen and cooling following peak metamorphism.
- There are two scenarios to explain deformational history. 1) An E-W extension phase, simultaneously with the onset of migmatization, developed the old, upright symmetric generation of folds. An intense subsequent shear has formed E-plunging isoclinal folds and parallel mineral stretching lineations. A later phase of NNW-SSE shear deflected the ESE-WNW foliation. 2) An E-W extension has taken place along with NNW-SSE shear phase, which were responsible for the development of isoclinal folds, mineral stretching lineations and displacement of ESE-WNW foliations.

10 Acknowledgements

11 References

Ackermand, D., Seifert, F. & Schereyer, W., 1975: Instability of sapphirine at high pressures, contributions to Mineralogy and Petrology. 50, 79-92.

Andersson, J., Söderlund, U., Cornell, D., Johansson, L. & Möller, C., 1999: Sveconorwegian (-Grenvillian) deformation, metamorphism and leucosome formation in SW Sweden, SW Baltic Shield: constraints from a Mesoproterozoic granite intrusion. Precambrian Research 98, 151-171.

Andersson, J., Möller, C. & Johansson, L., 2002: Zircon geochronology of migmatite gneisses along the Mylonite Zone (S Sweden): a major Sveconorwegian terrane boundary in the Baltic shield. Precambrian Research 114, 121-147.

Austin Hegardt, E., Cornell, D. H., Claesson, L., Simakov, S., Stein, H. J. & Hannah, J. L., 2005: Eclogites in the central part of the Sveconorwegian Eastern Segment of the Baltic Shield: support for an extensive eclogite terrane. GFF 127, 221-232.

Baxter, E. F., DePaolo, D. J., & Renne, P. R., 2002: Spatially Correlated Anomalous $^{40}Ar/^{39}Ar$ "Age" Variations About a Lithologic Contact near Simplon Pass, Switzerland: A Mechanistic Explanation for Excess Ar. Geochimica et Cosmochimica Acta, 66, 1067-1083.

Baxter, E. F., 2003: Quantification of the factors controlling the presence of excess ^{40}Ar and 4He. Earth and Planetary Science Letters, 216, 619-634.

Bingen, B., Skår, Ø., Marker, M., Sigmond, E. M. O., Nordgulen, Ø., Ragnhildstveit, J., Mansfeld, J., Tucker, R. D. & Liégeois, J. P., 2005: Timing of continental building in the Sveconorwegian orogen, SW Scandinavia. Norwegian Journal of Geology 85, 87-116.

Bingen, B., Stein, H. J., Bogaerts, M., Bolle, O. & Mansfeld, J., 2006: Molybdenite Re-Os dating constrains gravitational collapse of the Sveconorwegian orogen, SW Scandinavia. Lithos 87, 328-346.

Bingen, B., Nordgulen, O. & Viola, G., 2008: A four phase model for the Sveconorwegian orogeny, SW Scandinavia. Norwegian Journal of Geology 88, 43-72.

Bingen, B., Viola, G., Engvik, A. K. & Yi, K., 2012: The hot long-lived Sveconorwegian Collisional Orogen: A review and new constraints from SE Norway. GAC-MAC Annual Meetings, StJohns2012, Abstracts vol. 35.

Burg J-P., 1999: Ductile structures and instabilities: their implication for Variscan tectonics in the Ardennes. Tectonophysics, vol. 309 (1-4), 1-25.

Christoffel, C. A., Connelly, J. N. & Åhäll, K.-I., 1999: Timing and characterization of recurrent pre-Sveconorwegian metamorphism and deformation in the Varberg-Halmstad region of SW Sweden. Precambrian Research, 98, 173-195.

Connelly, J. N., Berglund, J. & Larson, S. Å., 1996: Thermotectonic evolution of the Eastern Segment of southwestern Sweden: tectonic constraints from U–Pb geochronology. In T.S. Brewer, Ed. Precambrian crustal evolution in the North Atlantic Region, Geological Society, London, Special Publications. 112, 297-313.

Dahl, P. S., 1996: The effects of composition on retentivity of argon and oxygen in hornblende and related amphiboles: A field-tested empirical model. Geochimicae et Cosmochimic Acta, Vol. 60, No. 19, 3687-3700.

Dalrymple, G. B. & Lamphere, M. A., 1971: ^{40}Ar/^{39}Ar technique of K/Ar dating: a comparison with the conventional technique. Earth Planetary Science Letters, 12, 300-308.

Dodson, M. H., 1973: Closure temperature in cooling geochronological and petrological systems. Contrib. Mineral. Petrol. 40, 259–274.

Dyck, B., 2011: A key fold structure within a Sveconorwegian eclogite-bearing deformation zone in Halland, south-western Sweden: geometry and tectonic implications., M.Sc. thesis in Geology at Lund University, Nr. 279, 42 p.

Ekdahl, M., 2001: The Källsjö augen gneiss: A study of deformation pattern and kinematic indicators within the Ullared Deformation Zone. M.Sc. thesis in Geology at Lund University, Mineralogy and petrology, Nr. 132, 38 p.

Faure, G., 1986: Principles of isotope geology, 2nd edition, John Wiley & Sons, 589 p.

Goldsmith, J. R. & Newton, R. C., 1977: Scapolite-plagioclase stability relations at high pressures and temperatures in the system $NaAlSi_3O_8$-$CaAl_2Si_2O_8$-$CaCO_3$-$CaSO_4$. American Mineralogist 62, 1063-1081.

Harrison, T. M., 1981: Diffusion of ^{40}Ar in hornblende: Contributions to Mineralogy and Petrology, v. 70, 324–331.

Harrison, T. M., Duncan, I, & McDougall, I., 1985: Diffusion of 40Ar in biotite: Temperature , pressure and compositional effects. In Geochimica et Cosmochimica Acta, 49(11), 2461-2468.

Hoffman, P. F., 1991: Did the breakout of laurentia turn gondwanaland inside-out?. Science 252, 1409-1412.

Johansson, L., Lindh, A. & Möller, C., 1991: Late Sveconorwegian (Grenville) high-pressure granulite facies metamorphism in southwest Sweden. Journal of Metamorphic Geology 9, 283-292.

Johansson, L., Möller, C. & Söderlund, U., 2001: Geochronology of eclogite facies metamorphism in the Sveconorwegian Province of SW Sweden. Precambrian Research 106, 261-275.

Kelley, S., 2002: Excess argon in K-Ar and Ar-Ar geochronology. *Chemical Geology*, 188, 1-22.

Laajoki, K., Corfu, F. & Andersen, T., 2002: Lithostratigraphy and U-Pb geochronology of the Telemark supracrustals in the Bandak-Sauland area, Telemark, South Norway. Norwegian Journal of Geology 82, 119-138.

Lin, S., Jiang, D. & Williams, P. F., 2007: Importance of differentiating ductile slickenside striations from stretching lineations and variation of shear direction across a high-strain zone. Journal of Structural Geology 29, 850-862.

Lundberg, E. & Juhlin, C., 2011: High resolution reflection seismic imaging of the Ullared Deformation Zone, southern Sweden. Precambrian Research 190, 25-34.

McDougall, I. & Harrison, T.M., 1999: Geochronology and thermochronology by the ^{40}Ar/^{39}Ar method: New York, Oxford, Oxford University Press, 269 p.

Moecher, D. P. & Essene E. J., 1991: Calculation of CO_2 activities using scapolite equilibria: constraints on the presence and composition of a fluid phase. Contributions to mineralogy and petrology 108, 219-240.

Möller, C., Andersson, J., Söderlund, U. & Johanson, L., 1997: A Sveconorwegian deformation zone (system?) within the Eastern Segment, Sveconorwegian orogen of SW Sweden- a first report. GFF 119, 73–78.

Möller, C., 1998: Decompressed eclogites in the Sveconorwegian (-Grenvillian) orogen of SW Sweden: Petrology and tectonic implications. Journal of Metamorphic Geology 16, 641-656.

Möller, C., 1999: Sapphirine in SW Sweden: a record of Sveconorwegian (-Grenvillian) late-orogenic tectonic exhumation. Journal of Metamorphic Geology 17, 127–141.

Möller, C., Andersson, J., Lundqvist, I. & Hellström, F. A., 2007: Linking deformation, migmatite formation and zircon U-Pb geochronology in polymetamorphic gneisses, Sveconorwegian province, Sweden. Journal of Metamorphic Geology 25, 727-750.

Möller C., Andersson J. & Dyck, B., 2011: An eclogite-bearing fold nappe (or flow channel?) in the Sveconorwegian Province, Scandinavia. Abstract. The 9:th International Eclogite Conference, Marianske Lazne, Tzech Republic, 49-50.

Möller, C., Andersson, J. & Dyck, B., 2012: An eclogite-bearing fold structure in the Sveconorwegian Orogen, Scandinavia. Abstracts, vol. 35. GAC-MAC Conference, St John's, Canada, 94-95.

Park, R. G., Åhäll, K. I. & Boland, M. P., 1991: The Sveconorwegian shear-zone network of SW Sweden in relation to mid-Proterozoic plate movements. Precambrian Research 49, 245-260.

Passchier C. W. & Trouw R. A. J.,1996: Microtecton ics. Springer, 289 p.

Renne, P. R., Swisher, C. C., Deino, A. L., Karner, D. B., Owens, T. & DePaolo, J. D., 1998: Intercalibration of standards, absolute ages and uncertainties in $^{40}Ar/^{39}Ar$ dating. Chemical Geology, 145, 117-152.

Ridley, J., 1986: Parallel stretching lineations and fold axes oblique to a shear displacement direction-A model and observations: Journal of Structural Geology 8, 647-655.

Scaillet, S., 1996: Excess ^{40}Ar transport scale and mechanism in high-pressure phentites: a case study from an eclogitised metabasite of the Dora-Maira nappe, western Alps. Geochim. Cosmochim. Acta 60, 1075/1090.

Smalley, P. C., Field, D., Lamb, R. C. & Clough, P. W. L., 1983: Rare earth, Th, Hf, Ta, and large-ion lithophile element variations in metabasites from the Proterozoic amphibolite-granulite transition zone at Arendal, South Norway. Earth and Planetary Science Letters 63, 446-458.

Söderlund, U., Jarl, L. G., Persson, P. O., Stephens, M. B. & Wahlgren, C. H., 1999: Protolith ages and timing of deformation in the eastern, marginal part of the Sveconorwegian orogen, southwestern Sweden. Precambrian Research 94, 29-48.

Söderlund, U., Möller, C., Andersson, J., Johansson, L. & Whitehouse, M. J., 2002: Zircon geochronology in polymetamorphic gneisses in the Sveconorwgian orogen, SW Sweden: ion microprobe evidence for 1.46-1.42 Ga and 0.98-0.96 Ga reworking. Precambrian Research 113, 193-225.

Söderlund, U. & Ask, R., 2006: Mesoproterozoic bimodal magmatism along the Protogine Zone, S Sweden: three magmatic pulses at 1.56, 1.22 and 1.205 Ga, and regional implications. GFF, 128, 303-310.

Söderlund, U., Hellström, F. A. & Kamo, S. L., 2008: Geochronology of high-pressure mafic granulite dykes in SW Sweden; tracking the P-T-t path of metamorphism using Hf isotopes in zircon and baddeleyite. Journal of Metamorphic Geology 26, 539-560.

Steiger, R. H. & Jäger, E., 1977: Subcommission on geochronology: convention on the use of decay constants in geo- and cosmochronology. Earth and Planetary Science Letters, 36, 359 - 362.

Stephens, M. B., Wahlgren, C. H., Weijermars, R. & Cruden, A. R., 1996: Left lateral transpressive deformation and its tectonic implications, Sveconorwegian Orogen, Baltic Shield, Southwestern Sweden. Precambrian Research 79, 261-279.

Tual, L., Möller, C. & Pinan-Llamas, A., 2012: Structure and metamorphism of an eclogite-bearing deformation zone within the Sveconorwegian Orogen, Sweden. Abstracts, vol. 35 GAC-MAC Conference, St John's, Canada, 143 p.

Vernon, R., H. & Clarke, G. L., 2008: Principles of Metamorphic Petrology. Cambridge University Press, 460 p.

Wahlgren, C., -H., Cruden, A. R. & Stephens, M. B., 1994: Kinematics of a major fan-like structure in the eastern part of the Sveconorwegian orogen, Baltic Shield, south-central Sweden. Precambrian Research 70, 67-91.

Wang, X. D. & Lindh, A., 1996: Temperature-pressure investigation of the southern part of the Southwest Swedish Granulite Region. European Journal of Mineralogy 8, 51-67.

Winter, J. D., 2010: Principles of Igneous and Metamorphic Petrology, 2nd Edition. Prentice Hall Publications, 702 p.

Appendix I. 40Ar/39Ar heating schedules and data.

Step	Ca/K	40*Ar/39Ar	Age (Ma)	± Sigma error
Sample NAS016A (2038-01)				
2038-01A	7.00926	103.58515	553.13126	54.31482
2038-01B	4.01372	101.31523	542.66186	40.35302
2038-01C	5.32015	101.89845	545.35758	71.14786
2038-01D	4.60491	176.79612	861.8353	17.13654
2038-01E	6.31391	192.4662	921.56645	2.98077
2038-01F	6.56408	193.72717	926.28812	2.25861
¥2038-01G	6.58278	192.40124	921.32287	1.4445
¥2038-01H	6.65724	191.4032	917.57644	1.55925
¥2038-01I	6.5906	192.39313	921.29247	1.70513
¥2038-01J	6.3553	191.13664	916.57453	1.47315
¥2038-01K	6.11402	191.7451	918.86072	1.74644
¥2038-01L	6.28627	191.91422	919.49568	2.11345
¥2038-01M	6.49621	194.20686	928.08107	4.6608
¥2038-01N	6.64416	193.87043	926.82377	3.74997
¥2038-01O	6.50367	193.35987	924.91403	2.79636
¥2038-01P	6.54252	195.06223	931.27378	7.37638
Integrated Age=			920.1	1.7
(¥) Plateau Age =			919.9	1.4
Sample NAS016A (2038-02)				
2038-02A	0.21768	85.52572	468.10542	4.81516
2038-02B	0.01486	179.19885	871.12339	1.43298
2038-02C	-0.00674	192.90661	923.21696	1.20041
2038-02D	-0.00425	193.59149	925.78064	1.07947
¥2038-02E	0.00243	193.29269	924.66262	1.35506
¥2038-02F	0.03027	193.10231	923.94989	1.12874
¥2038-02G	0.2774	192.68282	922.37846	1.40966
¥2038-02H	1.41175	192.78704	922.76898	1.84593
¥2038-02I	2.27873	193.00947	923.60222	1.3987
¥2038-02J	2.82777	193.1096	923.97717	1.00765
¥2038-02K	4.3554	193.21803	924.38314	1.1151
¥2038-02L	3.33014	192.66872	922.32562	1.03999
¥2038-02M	1.28362	191.99304	919.79151	1.28853
¥2038-02N	1.27737	192.34115	921.0975	1.54897
¥2038-02O	1.53625	193.25404	924.51795	1.17841
¥2038-02P	3.84835	192.31162	920.98678	9.5619
Integrated Age=			920	1.3
(¥) Plateau Age =			923.2	1
Sample NAS016A (2038-03)				
2038-03A	10.58503	74.55249	414.41436	56.32187
2038-03B	12.07853	114.68258	603.45858	141.04567
2038-03C	5.61515	129.41289	668.16362	140.94942
2038-03D	7.55462	85.65926	468.74909	128.80652
2038-03E	3.10855	148.1729	747.34603	76.93199
2038-03F	4.79325	167.16724	824.12629	21.21608
¥2038-03G	5.58972	195.80585	934.04481	8.94134
¥2038-03H	6.31991	195.35562	932.36758	4.03579
¥2038-03I	6.48904	192.95017	923.38012	2.09599
¥2038-03J	6.48046	194.17217	927.95148	1.31633
¥2038-03K	6.49525	193.6876	926.14014	1.13691
2038-03L	6.33675	191.06375	916.30042	1.72419
2038-03M	11.35413	194.81186	930.33987	4.73991
Integrated Age=			924.2	1.8
(¥) Plateau Age =			926.7	1.7

48

Step	Ca/K	40*Ar/39Ar	Age (Ma)	± Sigma error
Sample NAS016A (2038-04)				
2038-04A	4.54523	95.23591	514.31955	26.86204
2038-04B	4.01166	255.45134	1143.49428	162.18168
2038-04C	4.935	77.86454	430.78897	81.56656
2038-04D	0.30998	139.35079	710.54206	43.39768
2038-04E	2.5945	158.64673	790.0876	30.18226
2038-04F	3.9753	205.32677	969.15251	22.14925
2038-04G	6.28375	187.19953	901.7108	7.52378
¥2038-04H	6.27915	194.3584	928.64709	2.67844
¥2038-04I	6.34413	193.8559	926.76946	1.95277
¥2038-04J	6.52269	194.05724	927.52201	2.04195
¥2038-04K	6.46617	193.32908	924.79882	1.478
¥2038-04L	6.61962	192.74007	922.59301	1.72047
¥2038-04M	6.48594	191.98305	919.75401	3.12707
¥2038-04N	7.06909	193.11087	923.98195	3.39195
2038-04O	13.48305	183.65856	888.23726	6.00888
Integrated Age=			921.4	1.9
(¥) Plateau Age =			925	1.7
Sample NAS0125 (2037-01)				
2037-01A	3.80593	118.38721	619.95144	5.48778
2037-01B	1.00566	165.38731	817.0685	1.86486
2037-01C	0.44725	194.72274	930.00731	2.69153
2037-01D	0.24865	196.82389	937.83156	2.38733
2037-01E	0.32878	198.07668	942.48059	2.38397
2037-01F	0.37433	198.31411	943.36033	2.61434
2037-01G	0.78644	199.27948	946.93288	2.38138
2037-01H	1.95888	200.62085	951.88515	3.04436
¥2037-01I	4.33994	195.09324	931.38942	1.99672
¥2037-01J	5.2634	193.38163	924.99548	1.27906
¥2037-01K	5.38172	194.25047	928.24396	1.4643
¥2037-01L	5.47982	194.23357	928.18086	1.18054
2037-01M	4.82412	192.70888	922.4761	1.43213
2037-01N	2.41314	191.88643	919.39135	1.63329
2037-01O	3.33268	197.28133	939.53046	2.70595
2037-01P	5.94118	204.92484	967.68413	2.79423
Integrated Age=			922.5	1.5
(¥) Plateau Age =			927.6	1.6
Sample NAS0125 (2037-02)				
2037-02A	17.47973	1743.14835	3520.31802	67.34689
2037-02B	39.14167	758.5773	2324.6622	44.30902
2037-02C	16.58632	266.32238	1179.18076	39.6597
2037-02D	16.04426	241.97717	1098.25972	28.33434
2037-02E	6.07236	548.87962	1921.57249	18.71659
2037-02F	6.22354	201.25958	954.23856	2.21295
2037-02G	6.48894	243.87572	1104.70246	2.4172
2037-02H	6.73432	199.05534	946.10402	1.50239
¥2037-02I	6.63571	194.01514	927.36468	1.2654
¥2037-02J	6.49852	194.85806	930.51222	1.56996
¥2037-02K	6.67552	193.93341	927.05918	2.42196
2037-02L	6.51294	187.39613	902.45594	5.33839
2037-02M	5.83486	178.24008	867.42287	9.82497
2037-02N	6.57509	183.15071	886.29658	6.42684
2037-02O	6.34881	193.04735	923.74408	2.34658
2037-02P	7.51228	207.36837	976.5926	21.69785

Step	Ca/K	40*Ar/39Ar	Age (Ma)	± Sigma error
Integrated Age=			971.7	1.8
(¥) Plateau Age =			928.4	1.9
Sample NAS018 (2034-01)				
2034-01B	1.88845	24.51986	147.06337	26.97834
2034-01C	0.94513	165.96387	819.35768	8.8394
2034-01D	0.34683	206.39056	973.03305	6.87218
2034-01E	0.2333	211.74943	992.45549	6.45451
•2034-01F	1.30085	198.06836	942.44975	6.05577
•2034-01G	2.11283	195.00579	931.0633	8.11339
•2034-01H	5.46239	194.4269	928.9029	5.09616
•2034-01I	6.24359	195.49729	932.89551	2.75254
•2034-01J	6.88673	194.45403	929.00424	1.82554
•2034-01K	6.91042	195.17675	931.70081	1.32824
•2034-01L	6.61417	195.56641	933.15304	1.56089
•2034-01M	6.60855	195.80474	934.04067	1.6756
2034-01N	5.13108	198.71963	944.86191	2.11645
2034-01O	5.84993	192.70027	922.44385	2.2975
2034-01P	4.50652	197.07505	938.76454	5.56768
2034-01Q	6.86015	196.50063	936.63	3.15594
2034-01R	11.00437	160.34803	796.93566	11.52285
Integrated Age=			931.5	1.7
(•) Plateau Age =			932	2
Sample NAS018 (2034-02)				
2034-02A	1.95953	157.62872	785.97746	17.43469
2034-02B	0.53346	193.18526	924.26047	10.83268
2034-02C	0.17734	347.96616	1426.76681	25.08776
2034-02D	1.15194	399.2522	1566.53569	10.76312
2034-02E	1.95492	206.05643	971.81507	5.24354
2034-02F	3.16997	197.43832	940.11315	6.08738
2034-02G	6.66799	196.61421	937.05227	1.44023
¥2034-02H	6.85604	194.99799	931.03422	1.38412
¥2034-02I	6.74171	194.8008	930.29858	1.1457
¥2034-02J	6.05923	195.76673	933.89916	2.39487
¥2034-02K	6.20024	195.04445	931.20749	1.60025
¥2034-02L	6.3866	194.49485	929.15663	1.53189
¥2034-02M	6.31435	194.22922	928.1646	1.55042
2034-02N	4.21563	198.82019	945.23406	1.91508
2034-02O	2.37468	199.90505	949.24414	1.61022
2034-02P	6.23157	184.71134	892.25366	2.85383
Integrated Age=			938.9	1.5
(¥) Plateau Age =			930.3	1.4
Sample NAS019 (2035-01)				
2035-01A	6.66947	105.84664	563.50175	57.00794
2035-01B	0.24802	167.11841	823.93302	11.68128
2035-01C	0.31041	185.72089	896.09676	12.31409
2035-01D	0.17458	191.18643	916.76172	8.1551
2035-01E	0.35855	196.24391	935.67521	6.80659
2035-01F	0.42502	195.41956	932.60589	9.13903
2035-01G	1.10949	194.72143	930.0024	5.46573
2035-01H	4.93007	193.83662	926.69737	2.14061
¥2035-01I	6.17503	191.59146	918.28372	1.49478
¥2035-01J	6.4931	191.22587	916.90998	1.47329

Step	Ca/K	40*Ar/39Ar	Age (Ma)	± Sigma error
¥2035-01K	6.42564	191.17986	916.73701	2.37146
¥2035-01L	5.70061	191.90531	919.46224	1.83043
¥2035-01M	3.52087	190.54747	914.35801	2.75757
¥2035-01N	3.06056	191.10105	916.44069	2.50361
2035-01O	4.58607	185.66879	895.89861	3.94856
2035-01P	4.60324	180.04439	874.3806	11.37053
Integrated Age=			916.5	1.8
(¥) Plateau Age =			917.5	1.7
Sample NAS019 (2035-02)				
2035-02A	1.1569	206.92973	974.99667	21.5383
2035-02B	0.27525	198.23838	943.07976	8.95556
2035-02C	0.25413	197.5354	940.47339	7.45592
2035-02D	0.50116	194.95595	930.87741	6.48649
2035-02E	1.31999	195.63827	933.42071	9.55147
2035-02F	1.73023	196.68376	937.31077	4.80582
2035-02G	2.38341	190.00314	912.30778	10.74875
2035-02H	5.86281	199.31334	947.05803	4.22522
¥2035-02I	6.37969	192.68294	922.37891	3.14579
¥2035-02J	6.84555	191.63126	918.43321	1.92244
¥2035-02K	6.53266	192.36749	921.19629	1.79807
¥2035-02L	6.7209	191.32602	917.28639	3.04881
¥2035-02M	4.92577	190.1762	912.95985	3.25661
2035-02N	5.07031	195.97718	934.68265	3.69151
2035-02O	8.53475	201.09883	953.64656	5.74955
2035-02P	13.38435	478.01461	1762.08907	29.98068
Integrated Age=			932	2
(¥) Plateau Age =			919	2
Sample NAS087 (2041-01)				
2041-01A	0.47799	165.23039	816.44495	3.91883
2041-01B	0.32167	193.9055	926.95488	5.09512
2041-01C	0.0848	196.49755	936.61855	2.94351
2041-01D	0.18386	193.10125	923.94593	2.60567
2041-01E	0.26377	192.60259	922.07773	2.49064
2041-01F	3.55791	199.75848	948.70288	1.49051
¥2041-01G	3.94587	194.27787	928.34634	1.28919
¥2041-01H	4.8265	194.89565	930.65245	1.41368
¥2041-01I	5.04257	195.496	932.8907	1.39459
¥2041-01J	3.06467	194.40198	928.80985	2.02563
¥2041-01K	3.99499	195.22452	931.87889	1.28024
¥2041-01L	1.40132	194.10789	927.7113	1.82605
¥2041-01M	2.12328	194.78825	930.25175	1.87366
¥2041-01N	3.10194	193.75768	926.40222	1.92713
¥2041-01O	1.78216	194.40123	928.80707	6.16955
Integrated Age=			929	1.5
(¥) Plateau Age =			930	1.3
Sample NAS087 (2041-02)				
2041-02A	4.48843	179.43774	872.04423	27.25741
2041-02B	9.72791	361.5746	1464.92175	80.51597
2041-02C	7.30213	174.07296	851.25044	47.64539
2041-02D	7.28773	171.69066	841.93931	32.14962
2041-02E	7.06506	187.58854	903.18488	14.84995
2041-02F	6.36991	192.70995	922.48014	3.13883
2041-02G	6.56271	193.47924	925.36073	1.83896
2041-02H	6.45894	198.28632	943.25737	1.80794

Step	Ca/K	40*Ar/39Ar	Age (Ma)	± Sigma error
¥2041-02I	6.72571	195.32968	932.27089	3.42261
¥2041-02J	6.50195	193.96673	927.18376	3.02783
¥2041-02K	6.46762	194.10425	927.69768	1.77159
¥2041-02L	6.03706	195.50724	932.93258	2.46828
¥2041-02M	6.62952	196.71506	937.42711	3.4224
2041-02N	9.94822	210.05852	986.34957	14.29956
2041-02O	15.58754	262.50982	1166.74546	40.53196
Integrated Age=			933	2
(¥) Plateau Age =			930	2
Sample NAS052 (2044-01)				
2044-01A	4.81052	167.01655	819.32552	38.32931
2044-01B	2.28408	197.62026	936.12598	77.1208
2044-01C	3.33656	180.38701	871.28706	53.36365
2044-01D	6.33024	127.03049	654.35001	30.56064
2044-01E	6.23897	166.178	816.01624	14.95357
¥2044-01F	8.01535	191.89663	914.84863	2.8465
¥2044-01G	7.9762	194.74123	925.45465	1.8474
¥2044-01H	7.94151	191.96506	915.1045	2.00226
¥2044-01I	7.37682	194.4645	924.4256	3.54789
¥2044-01J	7.84547	192.80483	918.24162	3.6438
¥2044-01K	6.39695	189.41079	905.52888	9.91235
¥2044-01L	6.58835	197.08287	934.13887	6.35331
¥2044-01M	6.67556	193.53627	920.9696	4.70062
¥2044-01N	6.47488	191.45117	913.18208	3.69038
2044-01O	0.24311	185.17921	889.55253	4.05808
Integrated Age=			916	2
(¥) Plateau Age =			920	4
Sample NAS052 (2044-02)				
2044-02A	1.03114	135.89804	692.25982	19.77308
2044-02B	-0.20897	169.46084	828.93723	26.74445
2044-02C	1.58426	178.53996	864.19736	17.90798
¥2044-02D	0.90594	190.53068	909.73346	9.6927
¥2044-02E	1.85041	190.28423	908.809	11.20687
¥2044-02F	2.23547	192.10574	915.63042	13.81938
¥2044-02G	6.44455	194.98285	926.35267	3.93355
¥2044-02H	5.5543	193.80445	921.96879	6.66454
¥2044-02I	6.9927	196.62831	932.45639	2.38031
¥2044-02J	6.52228	194.47208	924.4538	4.33515
¥2044-02K	6.62347	196.94512	933.62917	4.32327
¥2044-02L	4.90776	196.20493	930.88784	6.31389
¥2044-02M	3.63555	186.06091	892.89306	29.41533
¥2044-02N	3.34	194.20292	923.45238	2.84858
¥2044-02O	1.88441	192.45025	916.91768	5.40187
Integrated Age=			921	3
(¥) Plateau Age =			927	3
Sample NAS150 (2036-01)				
2036-01A	1.16092	178.50647	868.45179	5.93936
2036-01B	0.41306	215.65132	1006.4669	6.12907
2036-01C	0.45842	227.87623	1049.67411	9.0731
2036-01D	0.32797	224.59089	1038.16386	5.76626
2036-01E	0.67288	210.88335	989.33064	6.89762
2036-01F	0.7374	212.73686	996.01159	7.41186
2036-01G	0.76407	217.48735	1013.02248	6.35464

Step	Ca/K	40*Ar/39Ar	Age (Ma)	± Sigma error
2036-01H	1.9561	209.74009	985.19742	5.77612
2036-01I	5.86107	200.3374	950.83978	4.00847
2036-01J	5.76124	200.04655	949.7665	3.12519
¥2036-01K	5.7899	196.18811	935.46762	3.7921
¥2036-01L	6.86947	196.89548	938.09755	2.03359
¥2036-01M	5.88797	194.98996	931.00424	2.73721
¥2036-01N	5.13058	196.07265	935.03798	2.78247
2036-01O	6.75831	199.70479	948.50455	2.65408
2036-01P	33.22337	242.40347	1099.70837	7.99903
Integrated Age=			958	2
(¥) Plateau Age =			935	3
Sample NAS150 (2036-02)				
2036-02A	2.04434	298.66852	1281.37083	30.59065
2036-02B	0.25874	235.99266	1077.79934	22.58091
2036-02C	0.55428	204.13818	964.80682	24.25553
2036-02D	1.03022	221.83727	1028.45959	30.85006
2036-02E	2.09551	191.87994	919.36699	21.91583
2036-02F	4.69271	201.66504	955.73087	13.81279
2036-02G	5.79229	190.49217	914.14984	15.04976
2036-02H	6.93014	197.92874	941.93221	3.42072
2036-02I	6.60421	200.20101	950.33657	3.23066
2036-02J	6.86997	198.1017	942.57331	2.51232
2036-02K	7.08896	198.59529	944.40161	2.40937
¥2036-02L	7.08748	193.25993	924.53999	5.62329
¥2036-02M	6.94909	196.85229	937.93707	2.75168
¥2036-02N	6.97132	195.52405	932.99522	2.68221
2036-02O	7.69088	205.18453	968.63298	4.65855
2036-02P	12.72904	273.68444	1202.95351	39.87949
Integrated Age=			948	3
(¥) Plateau Age =			934	7
Sample NAS001 (2042-01)				
2042-01A	0.75419	233.3452	1068.67339	3.45016
2042-01B	0.62981	200.10822	949.99416	3.04538
2042-01C	0.52552	244.671	1107.39443	3.17113
2042-01D	0.77445	250.87038	1128.24229	2.60671
2042-01E	1.50879	254.0358	1138.79509	2.40802
2042-01F	2.63242	247.66685	1117.49924	2.11921
2042-01G	2.96966	233.94354	1070.73997	1.71796
2042-01H	4.12515	221.67001	1027.86845	1.40411
2042-01I	5.01857	207.85549	978.36325	1.18357
2042-01J	4.19642	212.43163	994.91307	1.38005
2042-01K	3.5119	222.73483	1031.62849	1.56205
2042-01L	3.34606	227.55191	1048.54111	1.4103
2042-01M	3.02551	231.76345	1063.19892	1.44429
2042-01N	1.92659	251.6951	1130.99769	1.47722
2042-01O	13.94712	359.30023	1458.60084	4.65847
Integrated Age=			1061.9	1.5
Sample NAS001 (2042-02)				
2042-02A	1.32636	178.45611	868.25733	5.45138
2042-02B	0.53139	184.55536	891.65913	5.287
2042-02C	1.27389	204.63415	966.62142	5.10972
2042-02D	3.22229	208.53382	980.82607	3.83143
2042-02E	3.60829	201.36685	954.63348	2.55935
2042-02F	3.66859	202.70379	959.54843	2.59423

Step	Ca/K	40*Ar/39Ar	Age (Ma)	± Sigma error
2042-02G	4.5394	199.79004	948.81943	1.40235
2042-02H	5.02971	195.41004	932.57041	1.6744
2042-02I	4.97447	194.93824	930.81132	1.57919
¥2042-02J	5.5201	193.88422	926.87531	1.1979
¥2042-02K	5.34745	193.08036	923.86768	1.42601
¥2042-02L	5.28286	193.7873	926.51297	1.15744
2042-02M	2.63055	195.93007	934.50728	1.24909
2042-02N	3.33677	205.17537	968.59952	1.65718
2042-02O	1.51339	240.36841	1092.78231	5.80248
Integrated Age=			937.5	1.5
(¥) Plateau Age =			926	1.6
Sample NAS029 (2040-01)				
2040-01A	19.83014	117.5068	616.04552	160.98212
2040-01B	16.39957	119.33432	624.14385	213.50917
2040-01C	9.44778	80.79932	445.17519	93.77657
2040-01D	5.78945	172.65322	845.70721	72.14992
2040-01E	10.1604	158.43766	789.24424	56.83353
2040-01F	3.98773	242.48387	1099.98146	43.45095
2040-01G	2.80864	292.36536	1261.90633	69.83373
2040-01H	11.85619	151.7738	762.15506	39.86624
2040-01I	7.45754	190.38195	913.73483	25.74781
2040-01J	8.5883	202.85819	960.1152	14.06207
2040-01K	11.13745	201.92196	956.67584	6.70342
2040-01L	10.69625	200.9573	953.12519	1.82545
2040-01M	9.94069	201.04102	953.43362	1.27905
2040-01N	10.30674	202.85201	960.09251	1.02786
2040-01O	10.09443	202.83552	960.03197	1.16802
2040-01P	10.06452	200.99109	953.24966	2.0539
Integrated Age=			957	1.6
Sample NAS029 (2040-02)				
2040-02A	9.52937	192.99446	923.546	91.49909
2040-02B	22.19006	688.27008	2199.2915	346.83378
2040-02C	81.82292	991.87278	2687.48679	2335.45573
2040-02D	8.41858	253.5104	1137.04781	72.41519
2040-02E	10.63956	274.34665	1205.07658	74.46157
2040-02F	7.29499	202.2442	957.86037	29.17217
2040-02G	8.30381	184.06636	889.79409	31.04541
¥2040-02H	8.63549	212.93592	996.72759	19.35965
¥2040-02I	9.50077	201.8687	956.47999	2.61638
¥2040-02J	10.01567	202.09994	957.33017	1.29056
¥2040-02K	9.62624	201.61795	955.55762	1.62094
¥2040-02L	9.99689	201.79451	956.20715	1.27976
¥2040-02M	9.50672	202.84811	960.07818	1.06347
¥2040-02N	9.38587	202.13671	957.46533	1.24871
¥2040-02O	9.60795	203.16159	961.22835	2.16675
¥2040-02P	9.82898	201.84513	956.3933	2.43913
Integrated Age=			957.7	1.5
(¥) Plateau Age =			957.8	1.3
Sample NAS029 (2043-01)				
2043-01A	7.30175	569.91929	1958.70861	46.61585
2043-01B	25.1383	5273.66228	5326.26598	381.94602
2043-01C	6.37848	1650.78141	3426.6036	68.24552
2043-01D	7.10524	439.34928	1661.80749	58.167
2043-01E	5.44519	322.03381	1345.69361	42.5801

Step	Ca/K	40*Ar/39Ar	Age (Ma)	± Sigma error
2043-01F	5.0783	258.77175	1149.04514	26.148
2043-01G	6.39126	231.81259	1058.25894	18.55936
2043-01H	6.60935	214.95929	999.09274	12.99193
2043-01I	9.40381	241.01134	1089.75234	5.33332
2043-01J	9.76176	206.35393	968.117	1.52732
¥2043-01K	10.07525	203.12758	956.36499	1.20539
¥2043-01L	9.80538	201.8021	951.51467	1.53562
¥2043-01M	9.62105	202.84971	955.34929	1.90101
¥2043-01N	9.91967	202.64539	954.60203	1.36691
2043-01O	10.28712	201.40952	950.07557	1.75876
Integrated Age=			971.1	1.7
(¥) Plateau Age =			954.7	1.6
Sample NAS029 (2043-02)				
2043-02A	7.19491	313.85292	1321.43816	32.03487
2043-02B	7.46749	420.42342	1614.41139	77.95757
2043-02C	7.82566	236.83415	1075.51916	42.70341
2043-02D	6.84853	267.78222	1178.39739	40.11872
2043-02E	7.11633	210.19782	982.01919	15.0976
2043-02F	9.06646	211.29889	985.98177	7.23524
¥2043-02G	10.42707	201.19403	949.28517	2.33736
¥2043-02H	10.29225	203.12603	956.35935	1.67648
¥2043-02I	10.1272	201.94689	952.04512	1.36303
¥2043-02J	10.24287	202.88866	955.49169	1.72242
¥2043-02K	10.45393	201.70152	951.14606	1.9363
¥2043-02L	9.86536	201.53935	950.55162	2.11028
¥2043-02M	9.79093	203.75981	958.67393	2.39754
¥2043-02N	10.16242	201.99836	952.23364	2.54573
2043-02O	11.05448	203.8882	959.14247	2.31255
Integrated Age=			957.4	1.7
(¥) Plateau Age =			953.3	1.5

**Tidigare skrifter i serien
"Examensarbeten i Geologi vid Lunds
universitet":**

281. Åkesson, Christine, 2011: Vegetations-
utvecklingen i nordvästra Europa under
Eem och Weichsel, samt en fallstudie av
en submorän, organisk avlagring i Bellinga
stenbrott, Skåne. (15 hp)

282. Silveira, Eduardo M., 2011: First precise
U-Pb ages of mafic dykes from the São
Francisco Craton. (45 hp)

283. Holm, Johanna, 2011**:** Geofysisk utvärdering
av grundvattenskydd mellan väg 11 och
Vombs vattenverk. (15 hp)

284. Löfgren, Anneli, 2011: Undersökning
av geofysiska metoders användbarhet
vid kontroll av den omättade zonen i en
infiltrationsdamm vid Vombverket. (15
hp)

285. Grenholm, Mikael, 2011: Petrology of
Birimian granitoids in southern Ghana -
petrography and petrogenesis. (15 hp)

286. Thorbergsson, Gunnlaugur, 2011: A
sedimentological study on the formation
of a hummocky moraine at Törnåkra in
Småland, southern Sweden. (45 hp)

287. Lindskog, Anders, 2011: A Russian record
of a Middle Ordovician meteorite shower:
Extraterrestrial chromite in Volkhovian-
Kundan (lower Darriwilian) strata at Lynna
River, St. Petersburg region. (45 hp)

288. Gren, Johan, 2011: Dental histology of
Cretaceous mosasaurs (Reptilia, Squamata):
incremental growth lines in dentine and
implications for tooth replacement. (45
hp)

289. Cederberg, Julia, 2011: U-Pb baddelyit
dateringar av basiska gångar längs
Romeleåsen i Skåne och deras påverkan
av plastisk deformation i Protoginzonen
(15 hp)

290. Ning, Wenxing, 2011: Testing the hypothesis
of a link between Earth's magnetic field
and climate change: a case study from
southern Sweden focusing on the 1st
millennium BC. (45 hp)

291. Holm Östergaard, Sören, 2011:
Hydrogeology and groundwater regime
of the Stanford Aquifer, South Africa.
(45 hp)

292. Tebi, Magnus Asiboh, 2011: Metamorphosed
and partially molten hydrothermal alteration
zones of the Akulleq glacier area, Paamiut
gold province, South-West Greenland. (45
hp)

293. Lewerentz, Alexander, 2011: Experimental
zircon alteration and baddeleyite formation
in silica saturated systems: implications
for dating hydrothermal events. (45 hp)

294. Flodhammar, Ingrid, 2011: Lövestads åsar:
En isälvsavlagring bildad vid inlandsisens
kant i Weichsels slutskede. (15 hp)

295. Liu, Tianzhuo, 2012: Exploring long-term
trends in hypoxia (oxygen depletion) in
Western Gotland Basin, the Baltic Sea.
(45 hp)

296. Samer, Bou Daher, 2012: Lithofacies
analysis and heterogeneity study of
the subsurface Rhaetian–Pliensbachian
sequence in SW Skåne and Denmark. (45
hp)

297. Riebe, My, 2012: Cosmic ray tracks in
chondritic material with focus on silicate
mineral inclusions in chromite. (45 hp)

298. Hjulström, Joakim, 2012: Återfyllning av
borrhål i geoenergisystem: konventioner,
metod och material. (15 hp)

299. Letellier, Mattias, 2012: A practical
assessment of frequency electromagnetic
inversion in a near surface geological
environment. (15 hp)

300. Lindenbaum, Johan, 2012: Identification
of sources of ammonium in groundwater
using stable nitrogen and boron isotopes
in Nam Du, Hanoi. (45 hp)

301. Andersson, Josefin, 2012: Karaktärisering
av arsenikförorening i matjordsprofiler
kring Klippans Läderfabrik. (45 hp)

302. Lumetzberger, Mikael, 2012:
Hydrogeologisk kartläggning av
infiltrationsvattentransport genom
resistivitetsmätningar. (15 hp)

303. Martin, Ellinor, 2012: Fossil pigments
and pigment organelles – colouration in
deep time. (15 hp)

304. Rådman, Johan, 2012: Sällsynta jordarts-
metaller i tungsand vid Haväng på Österlen.
(15 hp)

305. Karlstedt, Filippa, 2012: Jämförande
geokemisk studie med portabel XRF av
obehandlade och sågade ytor, samt pulver
av Karlshamnsdiabas. (15 hp)

306. Lundberg, Frans, 2012: Den senkambriska
alunskiffern i Västergötland – utbredning,
mäktigheter och faciestyper. (15 hp)

307. Thulin Olander, Henric, 2012:

Hydrogeologisk kartering av grund-vattenmagasinet Ekenäs-Kvarndammen, Jönköpings län. (15 hp)

308. Demirer, Kursad, 2012: U-Pb baddeleyite ages from mafic dyke swarms in Dharwar craton, India – links to an ancient supercontinent. (45 hp)

309. Leskelä, Jari, 2012: Loggning och återfyllning av borrhål – Praktiska försök och utveckling av täthetskontroll i fält. (15 hp)

310. Eriksson, Magnus, 2012: Stratigraphy, facies and depositional history of the Colonus Shale Trough, Skåne, southern Sweden. (45 hp)

311. Larsson, Amie, 2012: Kartläggning, beskrivning och analys av Kalmar läns regionalt viktiga vattenresurser. (15 hp)

312. Olsson, Håkan, 2012: Prediction of the degree of thermal breakdown of limestone: A case study of the Upper Ordovician Boda Limestone, Siljan district, central Sweden. (45 hp)

313. Kampmann, Tobias Christoph, 2012: U-Pb geochronology and paleomagnetism of the Westerberg sill, Kaapvaal Craton – support for a coherent Kaapvaal-Pilbara block (Vaalbara). (45 hp)

314. Eliasson, Isabelle Timms, 2012: Arsenik: förekomst, miljö och hälsoeffekter. (15 hp)

315. Badawy, Ahmed Salah, 2012: Sequence stratigraphy, palynology and biostratigraphy across the Ordovician-Silurian boundary in the Röstånga-1 core, southern Sweden. (45 hp)

316. Knut, Anna, 2012: Resistivitets- och IP-mätningar på Flishultsdeponin för lokalisering av grundvattenytor. (15 hp)

317. Nylén, Fredrik, 2012: Förädling av ballast-material med hydrocyklon, ett fungerande alternativ? (15 hp)

318. Younes, Hani, 2012: Carbon isotope chemostratigraphy of the Late Silurian Lau Event, Gotland, Sweden. (45 hp)

319. Weibull, David, 2012: Subsurface geological setting in the Skagerrak area – suitability for storage of carbon dioxide. (15 hp)

320. Petersson, Albin, 2012: Förutsättningar för geoenergi till idrottsanläggningar i Kallerstad, Linköpings kommun: En förstudie. (15 hp)

321. Axbom, Jonna, 2012: Klimatets och människans inverkan på tallens etablering på sydsvenska mossar under de senaste århundradena – en dendrokronologisk och torvstratigrafisk analys av tre småländska mossar. (15 hp)

322. Kumar, Pardeep, 2012: Palynological investigation of coal-bearing deposits of the Thar Coal Field Sindh, Pakistan. (45 hp)

323. Gabrielsson, Johan, 2012: Havsisen i arktiska bassängen – nutid och framtid i ett globalt uppvärmningsperspektiv. (15 hp)

324. Lundgren, Linda, 2012: Variation in rock quality between metamorphic domains in the lower levels of the Eastern Segment, Sveconorwegian Province. (45 hp)

325. Härling, Jesper, 2012: The fossil wonders of the Silurian Eramosa Lagerstätte of Canada: the jawed polychaete faunas. (15 hp)

326. Qvarnström, Martin, 2012: An interpretation of oncoid mass-occurrence during the Late Silurian Lau Event, Gotland, Sweden. (15 hp)

327. Ulmius, Jan, 2013: P-T evolution of paragneisses and amphibolites from Romeleåsen, Scania, southernmost Sweden. (45 hp)

328. Hultin Eriksson, Elin, 2013: Resistivitets-mätningar för avgränsning av lak-vattenplym från Kejsarkullens deponis infiltrationsområde. (15 hp)

329. Mozafari Amiri, Nasim, 2013: Field relations, petrography and 40Ar/39Ar cooling ages of hornblende in a part of the eclogite-bearing domain, Sveconorwegian Orogen. (45 hp)

LUNDS UNIVERSITET